UNIVERSITY OF CALIFORNIA

Santa Barbara

Development and Characterization of High-Performance Solution-Processed Bulk Heterojunction Organic Photodetectors

A dissertation submitted in partial satisfaction of the

requirements for the degree Doctor of Philosophy

in Chemistry

by

Jianfei Huang

Committee in charge:

Professor Thuc-Quyen Nguyen, Chair

Professor Yon Visell

Professor Guillermo C. Bazan

Professor Vojtech Vlcek

September 2021

The dissertation of Jianfei Huang is approved.

_____

Professor Yon Visell

_____

Professor Guillermo C. Bazan

_____

Professor Vojtech Vlcek

_____

Professor Thuc-Quyen Nguyen, Committee Chair

August 2021

Development and Characterization of High-Performance Solution-Processed Bulk Heterojunction Organic Photodetectors

by

Jianfei Huang

ACKNOWLEDGEMENTS

Yes, indeed, it is called acknowledgements, where my words of gratitude converge.

Yet, words fail to express my thankfulness to my family. First, my wife, Yuwei, who is always there for me, supporting the decision I made and accompanying me along the path. Without her, it is very likely that I would not be working on a PhD degree this afar from home. Then, it's my parents, who happen to exert a subtle balanced influence on me on the matter of pursing a PhD degree, with one always believing in me and encouraging me to go for my goal without doubts, and with the other always reminding me that there are always other routes and that while I should work hard on the current path, I need to be flexible. And lastly, the familial credits go to my little baby, Feiyu, born just a couple of months before the end of my PhD studies, who now only knows to innocently ask me for food and cuddling, gives me one more reason to work hard.

A great many thanks shall go to my PhD advisor, Professor Thuc-Quyen Nguyen, for a great many things: the research hardware – lab, instrument, materials, etc. – with which I have the basics for my research; the opportunities of joining different projects – the ratchet one under the NSF grant, the pressure sensor one under the CNSI Challenge Grant, and the photodetector one under the NRT27 – where I enjoyed the privilege of learning new things and collaborating with researchers from different backgrounds; the valuable advice on research, work and life – "think positively", "learn to multitask", "take the initiative to learn new things", etc. – which prepares me better for the real world outside school; and, above all, the continuous and unwavering supports when I need help to strive for a higher goal or to get out of a dilemma.

I also want to express my gratitude to the other thesis committee members, Professor Guillermo Bazan, Professor Yon Visell, Professor Vojtech Vlcek, and Professor Martin Moskovits, for being on board of my thesis committee, providing advice on research, collaborating on interesting projects, and potentially asking “tough” questions on my thesis defense so that I can put more thought on the things that I can improve.

As a someone who pursues PhD in Chemistry and works largely on materials science, but barely does synthesis work myself, I must thank Dr. Jaewon Lee for providing me with his wonderful materials CO1-4Cl(F) and COTIC-4F for my research and projects. With respect to materials supply, I must also thank Dr. Hidenori Nakayama, Dr. Hengbin Wang and the anonymous synthesist(s) from Mitsubishi Chemicals, who provide the materials SiOTIC-4F and COTIC-4F for the projects. Moreover, the discussion shared with Nori, Hengbin and others from the Mitsubishi team also helped greatly in setting the course for the projects.

Another “thank you” must go to Dr. Alexander Mikhailovsky for his reliable assistance in the optical setups and maintenance of the testing instruments. His patient training also got me started on understanding the characterization techniques for photodetectors.

The scanning microscopy is usually a long and tedious procedure. Thus, I owe my thanks to Dr. Akchheta Karki and Max Schrock, for their hours and hours of sitting in the Asylum room and help in the atomic force microscopy and scanning Kelvin probe microscopy.

I want to also thank the previous and current members from the CPOS and RE TOUCH Lab who are all amazing people as my colleagues/mentors in the lab, as cheerful officemates in our chit-chat chamber (i.e., the office), or as caring friends outside of the lab: Dr. Hung Phan, Dr. Viktor Brus, Dr. Akchheta Karki, Dr. Joachim Vollbrecht, Dr. Seo-Jin Ko, Dr. Lijiao Ren, Dr. Niva Ran, Dr. Hoang Luong, Dr. Tung Dang Nguyen, Dr. David Cao, Dr.

Alexander Lill, Dr. Michael Ford, Dr. Brett Yurash, Dr. Michael Hughes, Dr. Yuanyuan Hu, Dr. Shantonu Biswas, Dr. Thanh Nho Do, Dr. Ala' Eftaiha, Dr. Mike Heiber, Dr. Takashi Okubo, Dr. Zach Rengert, Dr. Samuel Collins, Dr. Álvaro Daniel Romero-Borja, Max Schrock, Katie Rosenthal, Benjamin Luginbuhl, Tyler Postle, Justin Beavers, Simon Biberger, Hao Yang, Peter Santiago, Eunjeong Jeong, Kevin Koster, William Le, Taku Ogawa, Carolina Espinoza, Mengjia Zhu, Zhifang Du, Ziyue Zhu, Alan Dixon, Hiba Wakidi, Sangcheol Yoon, Nora Schopp, Sangmin Chae, Jirat (Ik) Chatsirisupachai, Patchareepond (Tam) Panoy.

"*All work and no play makes Jack a dull boy!*" So, I am lucky to have Zhifang, Ziyue, and Dr. Lei Dou with whom I shared fun after work. This keeps me from becoming the dull Jack.

What is friendship, but a chance encounter?

This dissertation is supported by Mitsubishi Chemical Center for Advanced Materials through New Research Theme 27 (NRT-27) project, a partnership between the materials community at UC Santa Barbara and Mitsubishi Chemical Corporation. In addition, I was supported for a quarter by the CNSI Challenge Grant awarded to Professor Yon Visell and Professor Thuc-Quyen Nguyen.

Curriculum Vitae
of
Jianfei Huang

EDUCATION

2021 Doctor of Philosophy in Chemistry (Expected), University of California, Santa Barbara, California, United States

2016 Master of Engineering in Materials Science and Engineering, East China University of Science and Technology, Shanghai, China

2013 Bachelor of Engineering in Polymer Materials and Engineering, East China University of Science and Technology, Shanghai, China

PUBLICATIONS

2021 **Huang, J**, Lee J., Nakayama, H., Schrock, M., Cao, D. X., Cho, K., Bazan, G. C., Nguyen, T.-Q., Understanding and Countering Illumination-Sensitive Dark Current: Toward Organic Photodetectors with Reliable High Detectivity *ACS Nano*, **2021**, *15*, 1753.

2021 Du, Z., Mainville, M., Vollbrecht, J., Dixon, A. L., Schopp, N., Schrock, M., Peng, Z., **Huang, J.**, Chae, S., Ade, H., Leclerc, M., Manjunatha Reddy, G. N., Nguyen, T.-Q., Insights into Bulk-Heterojunction Organic Solar Cells Processed from Green Solvent, *Sol. RRL* **2021**, 2100213.

2020 **Huang, J.**, Lee, J., Vollbrecht, J., Brus, V. V., Dixon, A. L., Cao, D. X., Zhu, Z., Du, Z., Wang, H., Cho, K., Bazan, G. C., Nguyen, T.-Q., A High-Performance Solution-Processed Organic Photodetector for Near-Infrared Sensing. *Adv. Mater.* **2020**, *32*, 1906027.

2020 **Huang, J.**, Lee, J., Schrock, M., Dixon, A. L., Lill, A. T., Cho, K., Bazan, G. C., Nguyen, T.-Q., Large-Gain Low-Voltage and Wideband Organic Photodetectors via Unbalanced Charge Transport, *Materials Horizons* **2020**, *7*, 3234.

2020 Lill, A. T., Cao, D. X., Schrock, M., Vollbrecht, J., **Huang, J.**, Nguyen-Dang, T., Brus, V. V., Yurash, B., Leifert, D., Bazan, G. C., Nguyen, T.-Q., Organic Electrochemical Transistors Based on the Conjugated Polyelectrolyte PCPDTBT-SO_3K (CPE-K). *Adv. Mater.* **2020**, 1908120.

2020 Lee, J., Song, S., **Huang, J.**, Du, Z., Lee, H., Zhu, Z., Ko, S.-J., Nguyen, T.-Q., Kim, Y. J., Cho, K., Bazan, G. C, Bandgap Tailored Nonfullerene Acceptors for Low-Energy-Loss Near-Infrared Organic Photovoltaics. *ACS Materials Lett.* **2020**, *2*, 395.

2020 Lee, J., Ko, S.-J. Ko, **Huang, J.**, Seifrid, M., Wang, H., Nguyen, T.-Q., Bazan, G. C., Organic Solar Cell and Photodetector Materials and Devices, *Pending*, US16/792,000.

2020 Zhu, J., Zhu, Y., **Huang, J.**, Hou, L., Shen, J., Li, C., Synthesis of monodisperse water-stable surface Pb-rich CsPbCl 3 nanocrystals for efficient photocatalytic CO_2 reduction, *Nanoscale* **2020**, *12*, 11842.

2019 Lee, J., Ko, S.-J., Lee, H., **Huang, J.**, Zhu, Z., Seifrid, M., Vollbrecht, J., Brus, V. V., Karki, A., Wang, H., Cho, K., Nguyen, T.-Q., Bazan, G. C, Side-Chain Engineering of Nonfullerene Acceptors for Near-Infrared Organic Photodetectors and Photovoltaics. *ACS Energy Lett.* **2019**, 4, 1401.

2019 Lill, A. T., Eftaiha, A. F., **Huang, J.**, Yang, Hao., Seifrid M., Wang M., Bazan, G. C, Nguyen, T.-Q., High-k Fluoropolymer Gate Dielectric in Electrically Stable Organic Field-Effect Transistors, *ACS Appl. Mater. Interfaces* **2019**, *11*, 15821.

2019 Zhu, J., Zhu, Y., **Huang, J.**, Gong, Y., Shen, J., Li, C., Synthesis of $CsPbBr_3$ perovskite nanocrystals with the sole ligand of protonated (3-aminopropyl) triethoxysilane, *J. Mater. Chem. C*, **2019**, *7*, 7201.

2018 **Huang, J.**, Karki, A., Brus, V. V., Hu, Y., Phan, H., Lill, A. T., Wang, M., Bazan, G. C., Nguyen, T.-Q., Solution-Processed Ion-Free Organic Ratchets with Asymmetric Contacts. *Adv. Mater.* **2018**, *30*, 1804794.

2018 Cui, Q., Hu, Y., Zhou, C., Teng, F., **Huang, J.**, Zhugayevych, A., Tretiak, S., Nguyen, T.-Q., Bazan, G. C., Single Crystal Microwires of *p*-DTS$(FBTTh_2)_2$ and Their Use in the Fabrication of Field-Effect Transistors and Photodetectors. *Adv. Funct. Mater.* **2018**, *28*, 1702073.

2018 Yao, Y., Zhu, Y., **Huang, J.**, Shen, J., Li, C., Porous CoS nanosheets coated by N and S doped carbon shell on graphene foams for free-standing and flexible lithium ion battery anodes: Influence of void spaces, shell and porous nanosheet, *Electrochim. Acta*, **2018**, *271*, 242.

2018 Liu, Y., Zhu, Y., Shen, J., **Huang, J.**, Yang, X., Li, C., CoP nanoparticles anchored on N, P-dual-doped graphene-like carbon as a catalyst for water splitting in non-acidic media, *Nanoscale*, **2018**, *10*, 2603.

2017 Wang, Y., Zhu, Y., **Huang, J.**, Cai, J., Zhu, J., Yang, X., Shen, J., Li, C., Perovskite quantum dots encapsulated in electrospun fiber membranes as multifunctional supersensitive sensors for biomolecules, metal ions and pH, *Nanoscale Horizons*, **2017**, *2*, 225.

2017 Zhao, S., **Huang, J.**, Liu, Y., Shen, J., Wang, H., Yang, X., Zhu, Y., Li, C., Multimetallic Ni-Mo/Cu Nanowires as Nonprecious and Efficient Full Water Splitting Catalyst, *J. Mater. Chem. A*, **2017**, *5*, 4207.

2017 Shen, J., Zhou, Y., **Huang, J.**, Zhu, Y., Zhu, J., Yang, X., Chen, W., Yao, Y., Qian, S., Jiang, H., Li, C., In-Situ SERS Monitoring of Reaction Catalyzed by Multifunctional Fe_3O_4@TiO_2@Ag-Au Microspheres, *Appl. Catal. B*, **2017**, *205*, 11.

2017 Wang, H., Shen, J., **Huang, J.**, Xu, T., Zhu, J., Zhu, Y., Li, C., Atomically dispersed Au catalysts supported on CeO_2 foam: controllable synthesis and CO oxidation reaction mechanism, *Nanoscale*, **2017**, *9*, 16817.

2017 **Huang, J.**, Liu, Y., Chen, W., Shen, J., Zhu, Y., Li, C., Nitrogen-Doped Fe_3C@C Particles as an Efficient Heterogeneous Photo-Assisted Fenton Catalyst, X Yang, C Li, *RSC Adv.*, **2017**, *7*, 15168.

2016 Wang, Y., Zhu, Y., **Huang, J.**, Cai, J., Zhu, J., Yang, X., Shen, J., Jiang, H., Li, C., CsPbBr3 Perovskite Quantum Dots-Based Monolithic Electrospun Fiber Membrane as an Ultrastable and Ultrasensitive Fluorescent Sensor in Aqueous Medium, *J. Phys. Chem. Lett.*, **2016**, *7*, 4253.

2016 Chen, W., Yang, X., **Huang, J.**, Zhu, Y., Zhou, Y., Yao, Y., Li, C., Iron Oxide Containing Graphene/Carbon Nanotube Based Carbon Aerogel as an Efficient E-Fenton Cathode for the Degradation of Methyl Blue, *Electrochim. Acta*, **2016**, *200*, 75

2016 **Huang, J.**, Zhao, S., Chen, W., Zhou, Y., Yang, X., Zhu, Y., Li, C., Three-dimensionally Grown Thorn-like Cu Nanowire Arrays by Fully Electrochemical Nanoengineering for Highly Enhanced Hydrazine Oxidation, *Nanoscale*, **2016**, *8*, 5810.

2015 **Huang, J.**, Zhu, Y., Yang, X., Chen, W., Zhou, Y., Li, C., Flexible 3D Porous CuO Nanowire Arrays for Enzymeless Glucose Sensing: *In Situ* Engineered Versus *Ex Situ* Piled *Nanoscale*, **2015**, *7*, 559.

2015 **Huang, J.**, Li, H., Zhu, Y., Cheng, Q., Yang, X., Li, C., Sculpturing Metal Foams toward Bifunctional 3D Copper Oxide Nanowire Arrays for Pseudo-capacitance and Enzyme-free Hydrogen Peroxide Detection, *J. Mater. Chem. A*, **2015**, *3*, 8734

2015 Yang, X., Chen, W., **Huang, J.**, Zhou, Y., Zhu, Y., Li, C., Rapid Degradation of Methylene Blue in a Novel Heterogeneous Fe_3O_4@rGO@TiO_2-catalyzed Photo-Fenton System, *Sci. Rep.*, **2015**, *5*, 10632.

2015 Lv, X., Zhu, Y., Jiang, H., Yang, X., Liu, Y., Su, Y., **Huang, J.**, Yao, Y., Li, C., Hollow Mesoporous $NiCo_2O_4$ Nanocages as Efficient Electrocatalysts for Oxygen Evolution Reaction, *Dalton Trans.*, **2015**, *44*, 4148.

2015 Zhou, Y., Zhu, Y., Yang, X., **Huang, J.**, Chen, W., Lv, X., Li, C., Li, C., Au Decorated Fe_3O_4@TiO_2 Magnetic Composites with Visible Light-assisted Enhanced Catalytic Reduction of 4-Nitrophenol, *RSC Adv.*, **2015**, *5*, 50454.

2014 **Huang, J.**, Zhu, Y., Zhong, H., Yang, X., Li, C., Dispersed CuO Nanoparticles on a Silicon Nanowire for Improved Performance of Nonenzymatic H_2O_2 Detection, *ACS Appl. Mater. Interfaces*, **2014**, *6*, 7055.

2014 Yang, X., Zhong, H., Zhu, Y., Jiang, H., Shen, J., **Huang, J.**, C Li, Highly Efficient Reusable Catalyst Based on Silicon Nanowire Arrays Decorated with Copper Nanoparticles, *J. Mater. Chem. A*, **2014**, *2*, 9040.

PRESENTATIONS

2021	*"Developing Organic Photodetectors for Near Infrared Sensing"*, UCSB/Potsdam Mini-Symposium, Santa Barbara, United States and Potsdam, Germany
2020	*"Developing High-Performance Broadband Organic Photodetectors"*, Center for Polymers and Organic Solids Seminar, Santa Barbara, United States
2019	*"High-Performance Near Infrared Organic Photodetectors"*, Mitsubishi Chemical-Center for Advanced Materials Annual Review, Santa Barbara, United States
2019	*"Organic Photodetectors with NIR Response",* Center for Polymers and Organic Solids Seminar, Santa Barbara, United States
2019	*"Physics and Characterization of Organic Semiconductor Devices"*, Graduate Recruitment Poster Session, Department of Chemistry and Biochemistry, Santa Barbara, United States
2018	*"Characterizations of Organic Ratchet Based on Intrinsic Asymmetric Injecting Contacts"*, Center for Polymers and Organic Solids Seminar, Santa Barbara, United States
2017	*"Organic Electronic Ratchet Based on Pumping"*, Center for Polymers and Organic Solids Seminar, Santa Barbara, United States

AWARDS & HONORS

2017	Phi Lambda Upsilon, National Honorary Chemical Society, USA
2016	Outstanding Graduate of Shanghai, China
2015	National Scholarship for Graduate Students, China
2015	Titan Scholarship, China
2014	National Scholarship for Graduate Students, China
2014	EVONIK Scholarship, Germany & China

ABSTRACT

Development and Characterizations of High-Performance Solution-Processed Bulk Heterojunction Organic Photodetectors

by

Jianfei Huang

The motto of University of California is "*let there be light.*" But how do we know whether there is light, especially the light that we cannot see with our eyes? The answer is photodetectors. Photodetection has long play an indispensable role in modern technologies. The research endeavors on organic photodetectors (OPDs) have been continuously increasing in the recent years since they promise great potential as a platform for photosensing, imaging, and optical communication. Compared to the established crystalline inorganic counterparts, OPDs show their unique attractiveness: tunable spectral activity, low-temperature and low-cost fabrication, light weight and mechanical flexibility, large-area solution/printing processibility, and versatile integration into complicated optoelectronics. In this thesis, three studies are carried out to enhance the sensing performance, as well as to better understand the device physics of bulk heterojunction (BHJ) OPDs. Notwithstanding the exciting progress made thus far for OPDs, efficient broadband detection, especially in the near infrared (NIR) region, still needs to be improved due to the challenges in simultaneously securing high photoresponse and low dark/noise current for narrow bandgap systems. For the first part, the focus is placed on achieving high NIR sensing performance for BHJ organic photodiodes. A novel ultranarrow bandgap (~1.2 eV) small molecule is used, which present the highest responsivity of 0.45-0.52 A/W in the spectral region of 920 – 940 nm. With well suppressed charge injection under reverse bias using thick junction approach, high NIR specific

detectivity of ~10^{12} Jones can be obtained even at a large bias of 2 V. Subsequently, we touch an instability problem found for inverted structure OPDs, where a large inconsistency of dark current can be universally found between before- and after-illumination conditions, negatively impacting the crucial figures-of-merit such as specific detectivity. Systematic control tests reveal that the widely used zinc oxide electron transport layer has caused the issue, which is triggered by exposure to high energy photons. We identify an alternative electron transport layer, optimized as "multilayer" tin oxide film, which is not only immune to the illumination-induced dark current inconsistency, but also simultaneously retain well suppressed low dark/noise current, uncompromised photoresponse, and rapid response speed. With the success of regular photodiode based OPDs studied in the first two parts, the focus is then shifted to introducing photomultiplication (PM) gain to BHJ OPDs, aiming at external quantum efficiency over 100%. This goal is accompanied by the targets of simultaneously achieving broad spectral response, low operating voltage, and applicable photoresponse speed, the aspects where the current approaches of making PM OPDs show shortcomings. Introduction of electron trapping agent (tetracyanoquinodimethane, TCNQ) into the BHJ blend has resulted in PM OPDs that can deliver not only large EQE over 10^4 % at low operation voltages, but also a wide span of spectral response from ultraviolet to NIR. The origin of the observed large photocurrent gain is revealed to originate from the interfacial metal-organic interaction and the enhanced electron trapping in the bulk of the BHJ layer, both induced by the intentionally added TCNQ. These effects essentially convert the device behavior from that of a regular photodiode to a photoconductor with excessive trapping sites of electrons.

TABLE OF CONTENTS

Curriculum Vitae vii
ABSTRACT xi

Chapter 1. Introduction 1
1.1 Background and Motivation 1
1.2 Photodetectors Based on Organic Bulk Heterojunction 4
1.3 Figures-of-Merit of Photodetectors 7
1.3.1 Photoresponse 7
1.3.2 Noise/dark Current 8
1.3.3 Noise Equivalent Power and Specific Detectivity 10
1.3.4 Light Intensity Dependence of Photoresponse 12
1.3.5 Response Speed and Cutoff Frequency 14
1.4 Relevant Characterization Methods in This Work 16
1.4.1 (Photo)conductive Atomic Force Microscopy 16
1.4.2 Scanning Kelvin Probe Microscopy 18
1.4.3 Transmission Line Method 20
1.5 Synopsis of Chapters 21
1.5.1 Synopsis of Chapter 2 21
1.5.2 Synopsis of Chapter 3 22
1.5.3 Synopsis of Chapter 4 23
1.6 Permissions and Attributions 23

Chapter 2. High-Performance Near Infrared Organic Photodiode Based on Non-Fullerene Acceptor 25
2.1 Introduction 25
2.2 Materials and Thin-Film Absorption 27
2.3 Thin-Film Morphologies 28
2.3.1 Molecular Packing and Crystalline Features 28
2.3.2 Surface Morphology 30
2.4 Photoresponse 31
2.5 Dark Current and Shot Noise-Limited Specific Detectivity 32
2.6 Noise Spectrum, NEP and D* 35
2.7 Linear Dynamic Range (LDR) 37
2.8 Phototransient Behavior 38
2.8.1 Frequency-Modulated Response and Cutoff Frequency 38
2.8.2 Limiting Factors of Photoresponse Speed 40
2.9 Application for Photoplethysmography 42
2.10 Experimental 43
2.10.1 Device fabrication 43
2.10.2 Thin-Film Characterizations 44
2.10.3 Device Characterizations 45

Chapter 3. Understanding and Countering Illumination History – Sensitive Dark Current in Inverted Organic Photodetectors 47
3.1 Introduction 47
3.2 Illumination History – Sensitive Dark Current 49

3.3 External and Internal factors 52
3.4 Criteria for Alternative Electron Transport Layers 56
3.5 Tin Oxide as the Alternative 57
3.5.1 Material Characterizations 57
3.5.2 Photodetection Performance 60
3.5.3 Applicability in Other BHJ Systems 66
3.6 Difference between SnO_2 and ZnO as Electron Transport Layer 67
3.7 Other Attempts 69
3.8 Experimental 71
3.8.1 Device fabrication 71
3.8.2 Spectroscopic Analysis 72
3.8.3 Conductive atomic force microscopy 73
3.8.4 Device Characterizations 73

Chapter 4. Large-Gain Low-Voltage and Wideband Photomultiplication Organic Photodetectors via Unbalanced Charge Transport 75
4.1 Introduction 75
4.2 Photoresponse Performance 77
4.3 Origin of the PM Effect 80
4.3.1 Effect of TCNQ on the Interfacial Conditions 81
4.3.2 Effect of TCNQ on Charge Transport of the Active Layer 85
4.3.3 PM Gain Mechanism 89
4.4 Light Intensity Dependence 91
4.5 Phototransient Behavior 92
4.6 Applicability for Other Active Layer Materials 93
4.7 Experimental 96
4.7.1 Device fabrication 96
4.7.2 Spectroscopic Analysis 96
4.7.3 Thin-film Characterizations 97
4.7.4 Device Characterizations 97

Chapter 5. Conclusions and Outlooks 99
5.1 Summary of the PhD Work 99
5.2 Outlooks for Organic Photodetectors Development 101

Appendices 105
References 117

Chapter 1

Introduction

1.1 Background and Motivation

Photodetectors are an essential part of modern optoelectronic technologies. At present, the most commercialized photodetectors are based on crystalline inorganic semiconductors: silicon (Si), germanium (Ge), or III-V compound semiconductors, e.g., indium gallium arsenide (InGaAs), gallium arsenide phosphide (GaAsP), and so forth.[1] In spite of the high stability, large carrier mobility and wide spectral activity of these materials, the photodetectors based on them have drawbacks include equipment-intensive manufacturing, high-temperature fabrication processes incompatible to substrates with low thermal stability, intrinsic mechanical inflexibility, and expensive production.[2,3]

The emergence of organic semiconductor materials has provided novel pathways toward low-cost, performance-tunable, large-scale and mechanically conformable consumer optoelectronics. As a sensing platform, organic photodetectors (OPDs) utilize organic semiconductor as the photoactive layer materials. While industrial manufacturing of OPDs has not yet been established as maturely as that of the inorganic counterparts, OPDs have already been extensively investigated as an alternative or rival to the inorganic photodetectors due to their promising traits and feasibility in various applications (Figure 1.1) including healthcare, image sensors, bio-authentication security, etc.[4–6] Notably, thanks to the intrinsically mechanical flexibility of soft organic materials, OPDs can be readily integrated onto flexible substrate for the construction of conformable electronics.[7] The solution processability of organic semiconductors in common organic solvents can also be achieved

by rational molecular design, enabling facile low-temperature manufacturing methods such as dip/blade/spin/spray coating and roll-to-roll inkjet printing for low-cost and large-scale production.[8] Through synthetic engineering, the band structure and absorption characteristics of the organic semiconductor materials can also be finely tuned.[9,10] Moreover, the unique Frenkel excitation feature of organic semiconductors has been shown exploitable for constructing intrinsic narrowband sensing platform,[11] which would otherwise require employment of external optical filters for broad-absorption inorganic semiconductor photodetectors. The commercialization efforts for OPDs have also been seen, as exemplified by the start-up companies.[12,13]

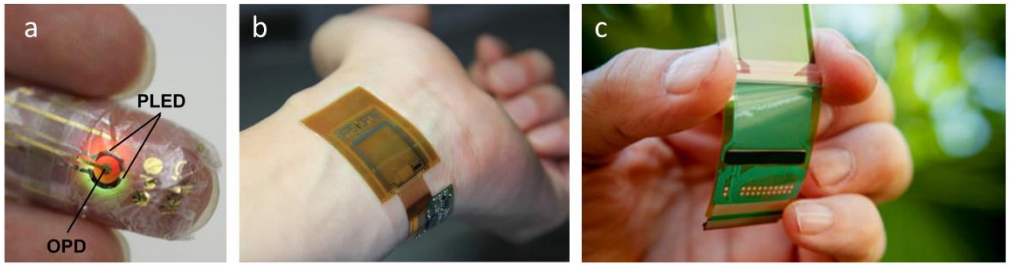

Figure 1.1. Prototypical applications of OPDs: (a) Flexible organic pulse oximeter comprising an OPD for health monitoring based on photoplethysmography.[4] Reprinted in accordance to license CC BY-NC 4.0. (b) OPD-based sensing arrays mounted on a wrist for vein pattern detection. Reprinted with permission from the Springer Nature, Copyright 2020.[5] (c) A bio-authentication module (Fingerprint Acquisition Profile 10) based on OPDs from Isorg, certified by FBI for security market.[6]

Usable as the materials for the photoactive layer in OPDs, the organic semiconductors are essentially solid-state organic small-molecule or polymeric materials, which mainly comprise carbon and hydrogen atoms, also sometimes heteroatoms (nitrogen, oxygen, and sulfur, etc.), and feature conjugated backbone with highly delocalized electrons. As an example, for conjugation system based on a carbon backbone, sp^2 hybridization was adopted by the carbon atoms along the conjugation system, with their p_z orbitals normal to the plane where the three sp^2 orbitals are situated. The sp^2 orbitals form the σ bonds that covalently linked the carbon

atoms, while the adjacent p_z orbitals and the electrons within create a "large" π bond with delocalized electron density (Figure 1.2a). Through bonding and antibonding interactions, the π and π* orbitals are formed (Figure 1.2b).[14] Consequently, among the π and π* orbitals are the highest occupied molecular orbital (HOMO) and lowest unoccupied molecular orbital (LUMO), which largely determine the electronic and optoelectronic properties of the organic semiconductors, where electron in the HOMO can be either thermally or optically excited from the LUMO.

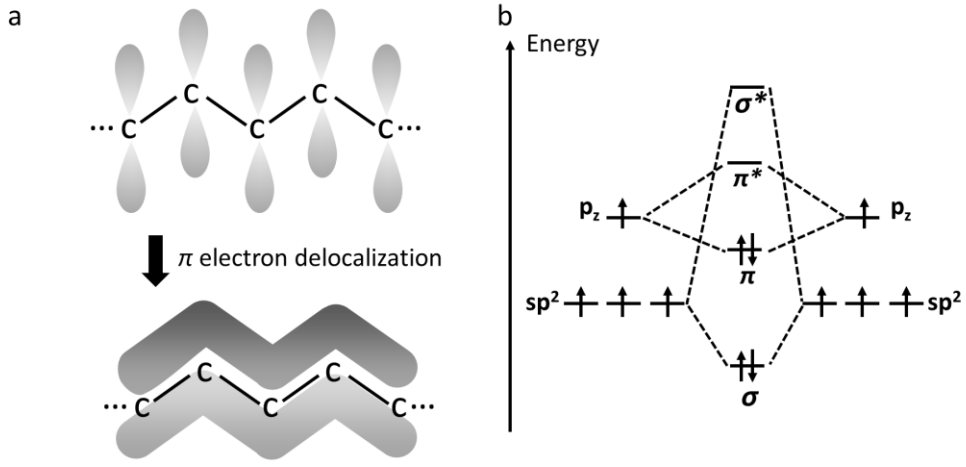

Figure 1.2. (a) Schematic of electron delocalization of the π orbitals along the carbon backbone. (b) Energy diagram of the bonding and anti-bonding of two sp^2 hybridized carbon atoms.

One unique feature of organic semiconductors in terms of optical excitation compared to the single-crystalline inorganic semiconductors is that the low relative permittivity (on the order of ~3) of organic semiconductors leads to relatively strong coulomb attraction between electron and hole. As a result, instead of free electrons and holes, optical excitation in organic semiconductors creates electrically neutral exciton, a bound electron hole pair, with a high binding energy (even up to 1 eV).[15] Such excitation is termed as Frenkel excitation, characterized by localization on a single molecular site and an electron-hole separation

distance no larger than the lattice constant.[16] Therefore, the dissociation of the exciton and photogeneration of free charge carriers are not trivial for organic semiconductors. To overcome the large binding energy for better photo-to-electric conversion, heterojunction structure incorporating organic semiconductors with different electron affinities and ionization potentials has been introduced, where the exciton goes through charge a so-called transfer (CT) state at the interface of the two materials for facilitated dissociation.[17] The detailed active layer configuration for organic photodiodes is explained in the next section.

1.2 Photodetectors Based on Organic Bulk Heterojunction

The development of organic photodiodes went through single-component (homojunction) to multicomponent (heterojunction) design.[18] A heterojunction features dissimilar semiconductor materials with different band structures and an interface between the two materials. For organic photoactive (photovoltaic and photoconductive) devices, planar heterojunction (PHJ) had been developed to replace the single-component homojunction architecture, leading to the then-record-high efficiency thanks to the improved exciton dissociation facilitated by the energy offsets between the electron donor (D) and electron acceptor (A).[19] To further improve the photocurrent generation, bulk heterojunction (BHJ) as the architecture for photoactive layer was put forward,[20,21] and now proves to be the most promising active layer configuration for achieving high-performance organic photodiodes in the solar energy conversion and photosensing applications.[18,22]

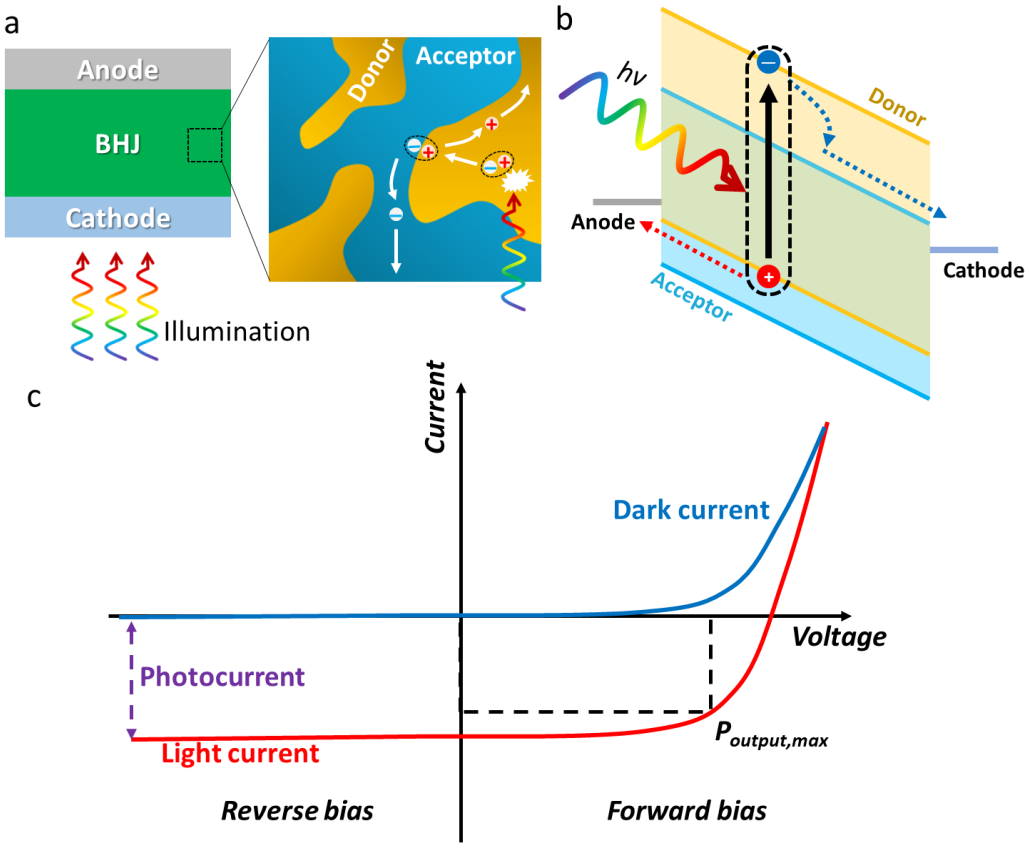

Figure 1.3. (a) Schematic of photocurrent generation for an organic photodiode containing a BHJ layer. (b) Band diagram of an organic photodiode operated under reverse bias for photocurrent generation. (c) Typical *J*-*V* characteristics of an organic photodiode.

Typically, in an organic BHJ, a blend of electron donor and electron acceptor materials form an intermixed percolating network, leading to a large interfacial area between the donor- and acceptor- rich domains throughout the bulk of the active layer (Figure 1.3a). When photons are incident on the donor-acceptor (D-A) blend, optical excitation occurs, and excitons are formed. The excitons then migrate to the D-A interface and dissociate into free holes and electrons with the assistance of the energy offsets between the donor and acceptor materials (Figure 1.3a and 1.3b). Subsequently, the free holes/electrons traverse the donor/acceptor domains to reach the anode/cathode contacts and are collected by the external circuit. Distinct from solar cells, photodetector devices are usually operated under reverse bias

instead of forward bias (Figure 1.3c). Therefore, the focus on the *J-V* characteristics of the two types of devices differs. In energy-harvesting solar cell devices, the core pursuit is a high product of the current and voltage in the fourth quadrant of the *J-V* characteristics, which basically presents the capability of the device doing work against an external bias. However, for photodetectors, maximizing the photocurrent is one of the basic goals, which is better realized under reverse bias with facilitated charge collection under assisted by the external electric field (Figure 1.3b). In addition, when the limiting factor of the device response speed is the transit time of the charge carriers, a larger electric field also contributes to faster charge collection, and therefore better a dynamic behavior of a photodetector.[23] However, a larger reverse bias generally leads to undesirably larger dark/noise current, which can originate from shunting, collection of thermally activated charges carriers, and/or charge injection from the contacts.[24,25] Particularly for BHJ based organic photodiodes, the advantage of higher photocurrent comes with the disadvantage of incurring higher dark current due to the direct physical contact of the donor material with the cathode, as well as acceptor material with the anode (Figure 1.3a and 1.3b). Such situations effectively lower the injection barriers of the charges from the contacts to the frontier orbitals of the active layer materials in the dark condition. Hence, unlike the solar cells whose operating condition is determined to maximize the output power ($P_{output,max}$) in the forward bias region, the operation condition of a photodetector emphasizes striking a fine balance between multiple figures-of-merit, such as photoresponse, dark/noise current, detector speed, response linearity, energy consumption, and more often depends on the specific applications for which the device is used. In the next section, the main figures-of-merit of OPDs and the characterization methods will be introduced.

1.3 Figures-of-Merit of Photodetectors

1.3.1 Photoresponse

As the name suggests, a photodetector detects light. Hence, its response toward incident photons is undoubtedly important. For convenience, the photoresponse is usually quoted as responsivity (R), commonly defined as the ratio of the photocurrent (I_{ph}) in amperes to the power of the incident light (P_{in}) in watts by the equation below:

$$R = \frac{I_{ph}}{P_{in}} \tag{1}$$

Although the responsivity is straightforward in definition, this parameter is relatively superficial. It is also predictable that the values of responsivity will be dependent on the wavelength due to the different energies of a single photon of different wavelength, which means the R value will be numerically different at different wavelength even if the photon-to-charge conversion efficiency is the same. Besides, the value of the parameter is not straightforward to tell whether or not certain photomultiplication gain mechanisms exist. Therefore, it is also common to quote the external quantum efficiency (EQE) for the description of the photoresponse. For photodetectors, EQE is defined as the ratio (quoted in percentage) of the number of electrons collected by the external circuit per unit time to the number of photons of a given energy that are incident on the active area of the detector per unit time. Hence, this parameter is more fundamental, and the value is not numerically affected by the energy of the photons at different wavelength in calculation. R and EQE can be mutually calculated if one of them is known according to the following equation:

$$R = \frac{EQE}{100\%} \times \frac{\lambda}{1240\ (\mathrm{nm\ W\ A^{-1}})} \tag{2}$$

1.3.2 Noise/dark Current

Although a photodetector is for light sensing, its purpose as a sensing tool subject it to other parameters which are measured not under illumination conditions. In electronic devices, various mechanisms can generate noises that are reflected as fluctuation of signals.[26] These noises, overlapped on the baseline, can cause difficulty in identifying an actual response to an incident optical signal when the magnitude of the response and that of the signal fluctuation (noise) is close (Figure 1.4). Hence, a certain signal-to-noise ratio is set for confirming the existence of a real signal with confidence. Apparently, lower the noise, weaker the interference in sensing applications. Nosie can be generated by different mechanisms. For instance, shot noise in electronics is considered to originate from the discrete nature of charges, whereas thermal noise stems from thermal agitation of the charge carriers.

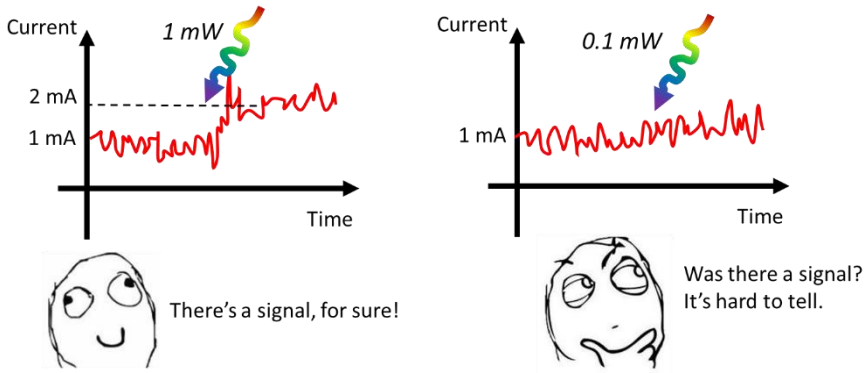

Figure 1.4. Cartoon showing difficulty of an imaginary photodetector with responsivity of 1 A/W in confirming detection of optical signal due to the existence of signal fluctuation (noise).

In this work, the experimentally measured noise of an OPD, or more accurately, the noise from the testing circuit in which the OPD is placed, is obtained by fast Fourier transform (FFT) of the dark current. The measurement is schematically shown in Figure 1.5. Of note is that the pre-amplifier that provides the DC bias also has its own noise characteristics. When using a pre-amplifier to magnify the signal to the oscilloscope and to provide reverse bias for

the OPDs, one should pay attention to two aspects of the pre-amplifier, usually provided in its specifications sheet. First, the pre-amplifier has its own frequency-dependence of noise, which may be imposed on the ultimately measured noise profile, and often are considered as part of the instrument background noise. Second, the frequency-dependent gain feature of the pre-amplifier dictates the frequency range within which the signal from the OPDs can be amplified according to the nominal amplification ratio. At higher frequencies, the amplification gain will drop and so the signals fed to the oscilloscope is attenuated, and even cut off. Thus, the pre-amplifier should be configured so that the background noise level from the pre-amplifier is minimized, while the working bandwidth of the pre-amplifier includes the frequency of interest.

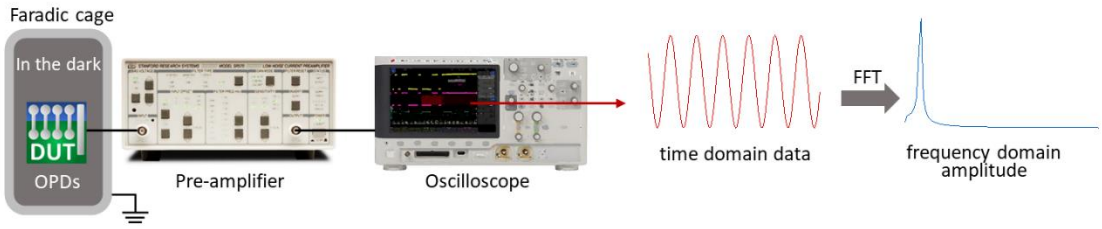

Figure 1.5. Setup and data processing for evaluating the noise of the OPDs.

Due to the complexity of noise current characteristics, its dependence on the employed circuitry, and configurations of the setups, one convenient approach to preliminarily compare the performance of OPDs from different labs/groups is to use shot noise, which is easily extractable from the dark current characteristics to replace the need for experimentally measuring the noise level. For instance, the major source of noise is commonly assumed to be from shot noise ($I_{n,\,sh}$), thermal noise ($I_{n,\,th}$), or their combination, white noise ($I_{n,\,wh}$), and therefore can be calculated by the following equations accordingly:[27]

$$I_{n,sh} = \sqrt{2qI_dB} \tag{3}$$

$$I_{n,th} = \sqrt{\frac{4kTB}{R_{sh}}} \tag{4}$$

$$I_{n,wh} = \sqrt{I_{n,sh}^2 + I_{n,th}^2} \tag{5}$$

where q is the elementary charge, I_d is the dark current, B is the bandwidth, k is the Boltzmann constant, T is the Kelvin temperature, and R_{sh} is the shunt resistance. Notably, these noise sources are considered frequency-independent within the relevant range. Despite that the assumption might not be always true and potentially induce risk of underestimating the actual noise level and ignoring the frequency-dependent component of noise (e.g., "flicker" noise), it provides a quick access to cross-lab comparison that at least gives an idea of the lowest possible noise limit of the devices prepared and tested by different labs.

1.3.3 Noise Equivalent Power and Specific Detectivity

As mentioned in the previous section, noise can obscure the presence of a targeted incoming signal when its magnitude is close to the response of the detector. More quantitatively for analysis, noise equivalent power (NEP) can be defined. For photodetectors, NEP is the signal power in a one hertz output bandwidth that gives a signal-to-noise ratio of one. It presents the signal power below which a system is no longer able to "confidently" confirm its presence out of the background noise. Apparently, this parameter is determined by both the photoresponse performance as well as the noise characteristics of the photodetector according to the following equation:

$$NEP = \frac{S_n}{R} \tag{6}$$

where S_n is the noise current spectral density, bearing the unit of $A\ Hz^{-1/2}$. The smaller the NEP, the weaker the incoming signal is identifiable by a photodetector. It should be noted that

the NEP value depends on S_n and R, both of which depend on the geometric setting, i.e., active area (A) of a photodetector. To allow direct comparison between photodetectors with different active areas, specific detectivity (D^*) has been introduced with the equation below:[28]

$$D^* = \frac{R\sqrt{A}}{S_n} \tag{7}$$

The unit of D^* is *cm* $Hz^{1/2}$ W^{-1}, or *Jones*, in honor of the American physicist *Robert C. Jones* who coined it. With this area-normalized parameter, direct comparison between photodetectors with different device geometry is made more feasible. As aforementioned, the noise current is sometimes directly calculated from the steady-state dark current characteristics of photodetectors based on the assumptions that certain noise(s) will be the dominant source. Hence, the following specific detectivity limits, respectively corresponding to the shot noise, thermal noise, and white noise, are usually defined in the literature:[27,29]

$$D^*_{sh} = \frac{R}{\sqrt{2qJ_d}} \tag{8}$$

$$D^*_{th} = \frac{R\sqrt{A}}{\sqrt{\frac{4kT}{R_{sh}}}} \tag{9}$$

$$D^*_{wh} = \frac{R\sqrt{A}}{\sqrt{2qI_d + \frac{4kT}{R_{sh}}}} \tag{10}$$

where D^*_{sh}, D^*_{th}, and D^*_{wh} are the shot noise-, thermal noise- and white noise- limited specific detectivity, respectively, and J_d is the dark current density.

1.3.4 Light Intensity Dependence of Photoresponse

EQE of photodetectors may be different under different intensities of the incident light. For example, under high light intensities, the increased photogeneration and carrier concentration can lead to more severe bimolecular recombination and less efficient extraction of the photogenerated charge carriers, giving rise to lower EQE values.[30] Non-linearity at low light intensities close to the NEP has also been documented.[31,32] Hence, the EQE as a function of light intensity is also concerned, especially for photodetectors expected to operate in a wide range of light intensity. Particularly, the span of the light intensity range within which the device output is linear to the incident light intensity is commonly used to describe the linearity of photodetectors. This feature is usually quoted as linear dynamic range (LDR), which is defined by:

$$\mathrm{LDR} = 20\log\frac{I_{upper}}{I_{lower}} = 20\log\frac{J_{upper}}{J_{lower}}\ (\mathrm{dB}) \qquad (11)$$

where I_{upper} and I_{lower} respectively stand for the maximum and minimum irradiance beyond or below which the device signal-irradiance relation deviates from linearity. J_{upper} and J_{lower} are the corresponding photocurrent measured at I_{upper} and I_{lower}, respectively. It is noteworthy that the prefactor "20" is sometimes replaced with "10" in the literatures.[33] This discrepancy stems from the choice of whether amplitude or power gain of the signal is being considered. Hence, when carrying out comparison of cross-lab results, extra attention should be paid to the definitions of this parameter.

For measuring LDR, the device output under various light intensities is measured. To adjust the light intensity in a large range spanning several orders of magnitude, tuning the power supplied to the light source and the use of neutral density optical filters can be combined, and the light intensity can be calibrated with a reference photodiode with known

responsivity/EQE. As for the measurement method, the optical signals from the light source and the device output signals can be made either as DC or AC (Figure 1.6). In the case of DC measurement, a light source is powered by a DC power source, and DC current response of the photodetector device, both in the dark and under different illumination of different light intensities, are measured. In principle, to measure the current response, either bias sweep or fixed bias steady-state measurement can be an option. However, the result of the dynamic bias sweep measurement may be affected by testing parameters (e.g., scan rate) and/or undesirable device characteristics (e.g., hysteresis). Therefore, steady-state current measurement under a fixed bias as a function of time is more recommended, in which way both the dark current and the current under illumination are measured in a single test. While the DC method is straightforward, it has some shortcomings. In the steady-state DC tests, signal drift may be present and may interfere the reading of the current. When detecting very weak light, the large-magnitude low-frequency noise signal may also overshadow the photoresponse in the current – time profile. These situations may be worse when the OPD devices present a certain degree of bias aging and show changing dark current under constant bias during the measurement. The alternative is the AC method, where AC optical signals at a certain frequency are used, and the detector response can be recorded with a lock-in amplifier referencing the frequency of the optical signals. To obtain the AC illumination condition, one can either use a function generator-powered light source, or use an optical chopper wheel placed between the DC light source and the detector. In the operation of a lock-in amplifier, the noise signals with frequencies other than the lock-in frequency are attenuated. This enables extraction of the signal of a targeted frequency with minimized interferences from both the noise of other frequencies and signal drifting under constant bias.

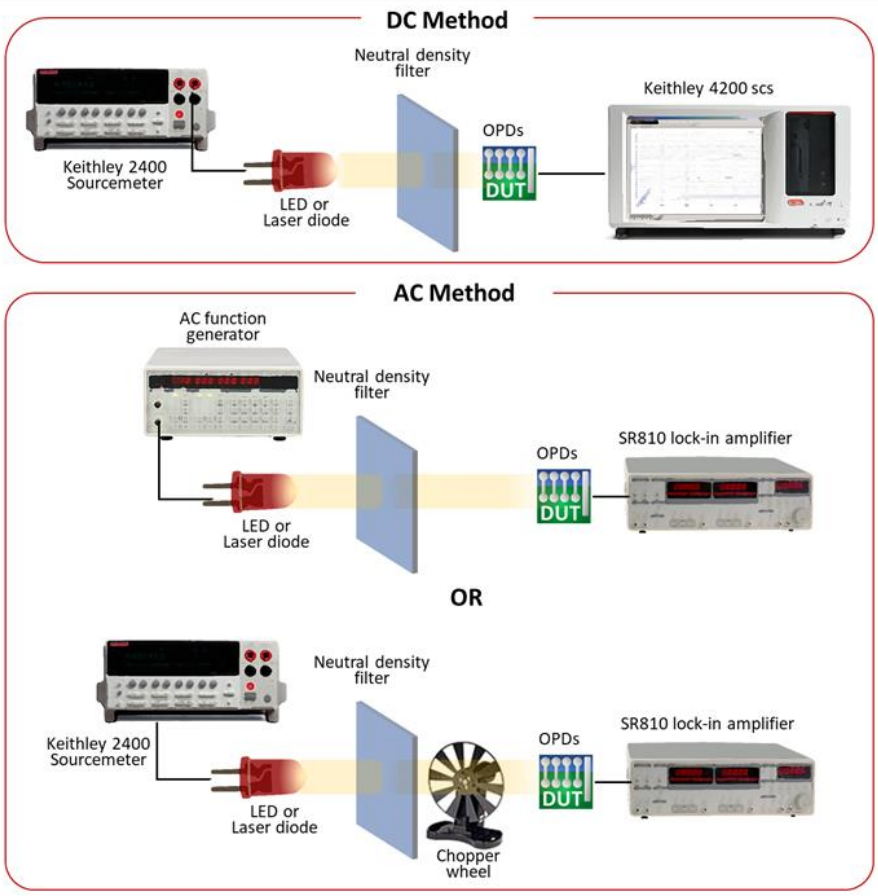

Figure 1.6. Measurement setups for the photoresponse of OPDs under different light intensities.

1.3.5 Response Speed and Cutoff Frequency

Depending on specific applications, the response speed of photodetectors toward optical signals may also be a figure-of-merit of vital importance. Take the example of image sensors where a matrix of photodetectors are operated: the signals from each sensing pixel is given limited time in order to achieve a decent frame rate for real-time imaging. This demand on fast response is even more critical for high-resolution imagers, where a larger number of pixels are on the panel and even less time for individual pixel/array.[5] When the photoresponse of an individual photodetector is too slow, the electric signal from the device cannot follow up the change of the optical signals within a given time to fully reach the expected steady-state

photoresponse value corresponding to the low-frequency condition, leading to attenuated output signals (Figure 1.7).

For evaluation of the response speed, typical parameters include rise time (t_r), fall time (t_f), and -3dB cutoff frequency (f_{-3dB}). The rise time and fall time denote the time required for the signal to go between 10% and 90% of the total change in the case of photocurrent increase and decay, respectively. It should be noted that t_r and t_f are not always equal, and their evaluation may also be made difficult with overshooting signals or electrical ringing in the circuit. The cutoff frequency, sometimes also referred to as the working bandwidth, represents the frequency at which the output signal of the photodetector is reduced to -3 dB (~70.8 %) of the nominal output.

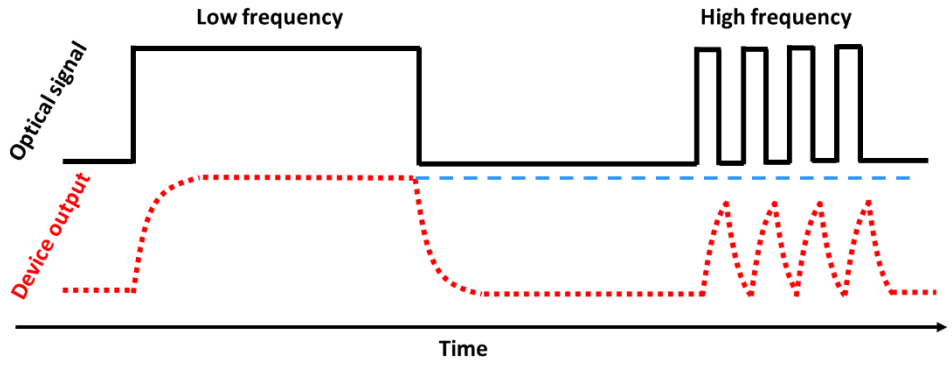

Figure 1.7. Typical photodetector dynamic response to optical signals at low and high frequencies.

To measure the transient response, the overall instrument setup is shown in Figure 1.8. A function generator is employed to power the light source, which can be either a laser diode or light-emitting diode, as long as its response speed (measurable or provided in the product specifications) is much faster than the device under test, namely the OPDs. The light source, powered by an AC voltage from the function generator with designated wave form, amplitude and frequency provides an on-off optical signal incident on the OPD device. To know how

well the OPD output signal follow the on-off optical signal, it is connected to a pre-amplifier, converting the current signal to voltage signal, which is then fed to an oscilloscope. It is recommended that the load resistance of the oscilloscope to be set as the commonly used small value, 50 Ω, to have a smaller RC time constant and less impact on the speed from the RC time constant of the testing circuit. Normally, OPDs are operated under short-circuit condition or reverse bias, which can be realized with the bias setting of the pre-amplifier. To obtain the cutoff frequency, the OPD output signal under various frequencies of the optical signal will be recorded, to find out at which frequency the OPD output signal is attenuated to -3 dB (~70%) of its steady-state value under sufficiently low frequencies.

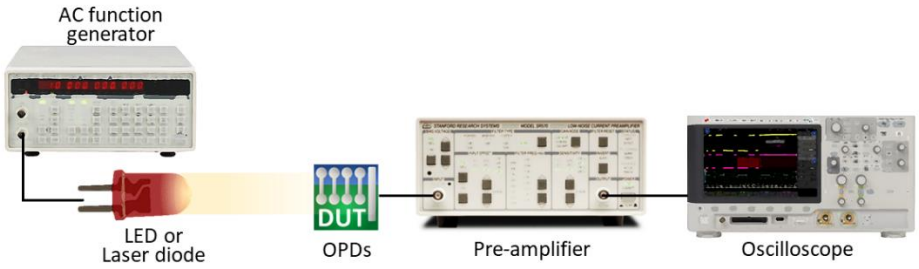

Figure 1.8. Measurement setups for phototransient behavior of the OPDs.

1.4 Relevant Characterization Methods in This Work

1.4.1 (Photo)conductive Atomic Force Microscopy

(Photo)conductive atomic force microscopy has been used in Chapter 3 to investigate the effect of illumination on the electron transport layer (ETL) in the OPDs. They are based on contact mode atomic force microscopy (AFM) with additional function of nanoscale current measurement (under illumination). As in contact mode AFM operation, a tip, which is fixed on a cantilever, is brought in contact with the sample surface (Figure 1.9). Due to the interaction force between the tip and the sample, the cantilever will show displacement,

measurable with a laser diode and a photodetector. The displacement is adjusted to a desired degree by a feedback system which controls the piezo scanner, on which the sample is placed, to raise or lower relative to the cantilever and the tip.

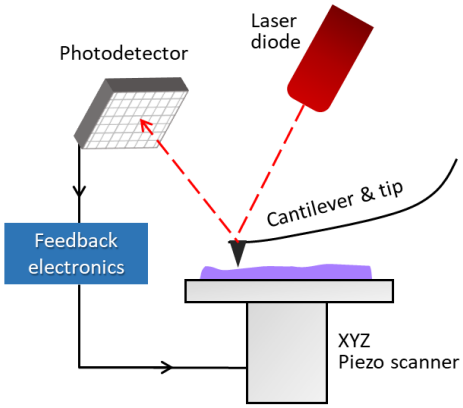

Figure 1.9. Basic setup of atomic force microscopy.

In the conductive atomic force microscopy (c-AFM), the contact mode scanning further features a voltage applied between a conductive tip and the sample, which enables simultaneous mapping of the nanoscale surface morphology and the local current running through the tip and the sample. For photoconductive atomic force microscopy (pc-AFM), a light source is employed to provide illumination on the sample while the similar c-AFM measurements are being carried out. The lamp is placed on the side away from the cantilever and tip to prevent them from blocking the illumination. The sample should also be prepared on a (semi)transparent substrate to allow sufficient light transmittance. As shown in Figure 1.10, by controlling the on-off status of the lamp, we can measure and compare the dark current change before and after illumination, providing clues on the effect of illumination on the electronic properties of the metal oxide sample films prepared on an ITO/glass substrate.

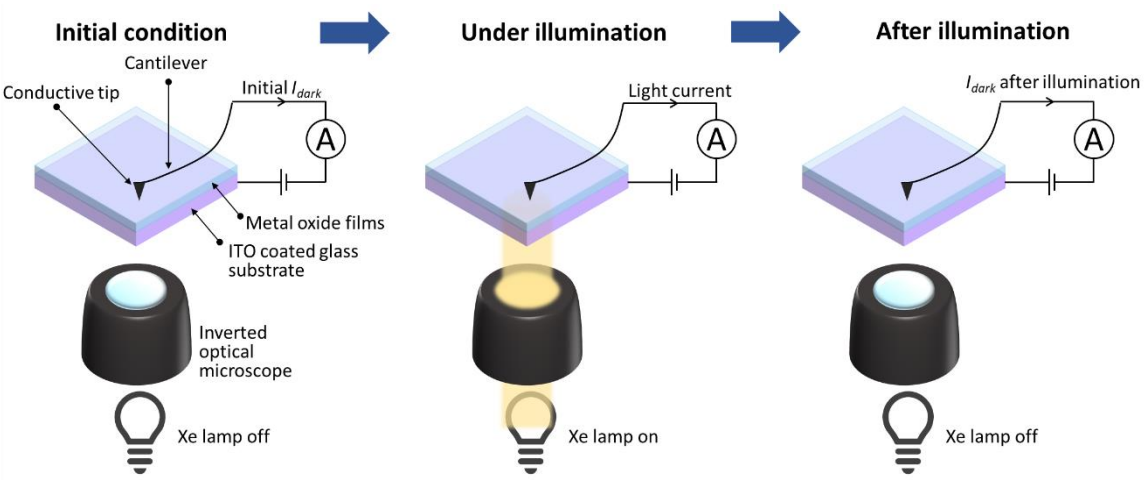

Figure 1.10. Schematic showing (photo)conductive AFM studying the effect of illumination on the electronic properties of metal oxide films used as ETL.

1.4.2 Scanning Kelvin Probe Microscopy

Scanning Kelvin Probe Microscopy (SKPM) is a type of non-contact AFM technique combined with a Kelvin probe function. In this thesis, SKPM is used to evaluate the work function change due to the influence of a deep-LUMO organic material, tetracyanoquinodimethane (TCNQ), on the aluminum metal electrode (Chapter 4). The potential offset between a conductive probe tip and a sample surface can be determined with the same principle as a common Kelvin probe. Due to the difference of work function between the tip material and the sample, a potential difference will exist, which is called contact potential difference (CPD), defined in the equation below:[34]

$$CPD = \frac{(\phi_{tip} - \phi_{sample})}{q} \tag{12}$$

where Φ_{tip} and Φ_{sample} are the work function of the tip and the sample, respectively, and q is the elementary charge. In order to measure the CPD, the tip is brough close to the surface of the sample. At the beginning, the tip and the sample are not electrically connected, and therefore their Fermi levels are not aligned (Figure 1.11a). Upon electrical connection, a

transient current flow between the two and renders their Fermi levels to align, and an equilibrium state is reached with the tip and the sample charged (Figure 1.11b). Subsequently, the system applies a DC voltage, denoted as V_{DC}, which has the identical magnitude as that of the CPD but with an opposite direction, to completely nullify the charging (Figure 1.11c). Therefore, the CPD can be known from the V_{DC} value, allowing one to calculated work function of the sample if the work function of the tip is known.

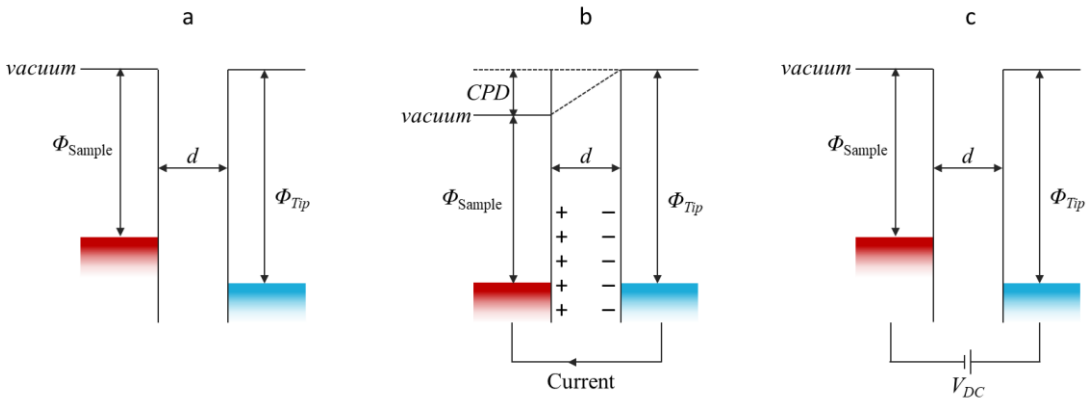

Figure 1.11. Energy diagram of SKPM operation for determination of the workfunction of the sample: (a) no contact between the sample and the tip, (b) the tip and sample are electrically connected, (c) an external bias V_{DC} is applied to nullify the charging caused by the CPD.

In the case of SKPM, the Kelvin probe tip is a microscopic AFM tip, which allows mapping out of local distribution of the CPD for the sample. During the scan, an AC voltage with the frequency of ω is also applied to the tip in addition the V_{DC}. This leads to a partial component of the electrostatic force (F_ω) between the sample and the tip with the frequency of ω according the following equation:[35]

$$F_\omega = \frac{dC}{dz}[V_{DC} - CPD]V_{AC}\sin(\omega t) \qquad (13)$$

where C is the capacitance, z is the separation and $V_{AC}\,sin(\omega t)$ is the AC voltage applied to the tip. To measure the CPD, a lock-in amplifier is employed to detect the cantilever oscillation

at frequency ω, and to find the V_{DC} value at which the F_ω becomes zero, signaling that the magnitude of the applied V_{DC} is equal to the CPD.

1.4.3 Transmission Line Method

In Chapter 4 of this thesis, transmission line method (TLM) is used to extract the contact resistance (R_{ct}) between the electrode and the organic BHJ layer in order to understand the effect of TCNQ on the electronic property of the metal/organic interface. In general, TLM measures the resistance between two electrodes, which have a conduction channel between them. By varying the distance between the two electrodes, the total resistance (R_{total}) as function of the length of the conduction channel can be obtained, which bears the following relation:

$$R_{total} = R_{ch} + 2R_{ct} = \rho\frac{L}{A} + 2R_{ct} \tag{14}$$

where R_{ch} is the resistance of the conductive channel between the two electrodes, ρ is the resistivity of the channel material, A is the cross-section area normal to the conduction direction, and L is channel length. By extrapolating to $L = 0$, one can extract the nominal value of $2 \times R_{ct}$ (Figure 1.12a). It should be noted that in a BHJ system with a narrow effective bandgap (~1 eV, defined as the difference between the LUMO of the acceptor and the HOMO of the donor), it is difficult to designate the measured current exclusively to the transport of holes or electrons due to the intrinsically ambipolar nature of most organic semiconductors. Hence, a field-effect transistor (FET) architecture is employed for the TLM test in this thesis. Since the organic FET is operated under accumulation mode, by negatively charging the gate, the device will be forced to show p-type transport, and therefore the charge injection at the

organic/metal interface will be relevant to hole carriers (Figure 1.12b). In this way, the R_{ct} extracted will be relevant to hole transport at the interfaces.

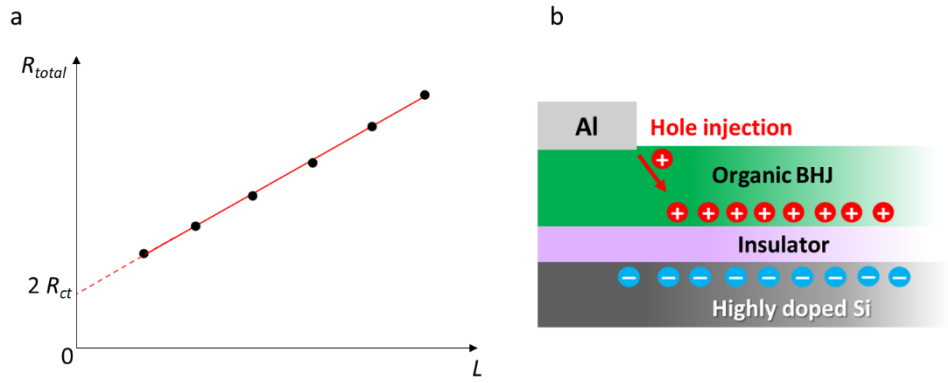

Figure 1.12. (a) Extraction of R_{ct} by TLM. (b) Field effect controlled TLM for extracting R_{ct} relevant to the carrier of holes.

1.5 Synopsis of Chapters

In this thesis, the design, fabrication, characterization and analysis of non-fullerene acceptor based BHJ OPDs with broadband sensitivity are presented. The work includes both OPDs based on regular rectifying junction diode structure, as well as photomultiplication (PM) type OPDs that exhibit external quantum efficiency larger than 100%. The concerned aspects incorporate achieving excellent photosensing performance, understanding the working principles, as well as tackling particular instability issue associated with OPDs. Below lists the summaries for the chapters from Chapter 2 to Chapter 4, where each chapter is designed to revolve around one specific topic, and comprises an independent, systematic and standalone set of experimental results and the corresponding analyses.

1.5.1 Synopsis of Chapter 2

The development of high-performance OPDs for near infrared (NIR) sensing still lags behind due to the early spectral cutoff, low photoresponse, and large dark/noise current, which

altogether leads to low a NIR specific detectivity. A novel non-fullerene small molecule named CO1-4Cl with a narrow bandgap (~1.2 eV) is used to couple with a conjugated polymer for constructing highly sensitive BHJ OPDs for NIR sensing. The optimized devices demonstrate a remarkable responsivity over 500 mA W^{-1} in the NIR spectral region (920 – 960 nm), which is the highest amongst organic photodiodes in the corresponding spectral region. By effectively delaying the onset of the injection current and suppressing the shunt leakage current using a simple thick junction, the optimized devices show a large specific detectivity around 10^{12} *Jones* for NIR spectral region up to 1010 nm. The phototransient behavior of the OPDs is also investigated, which reveals the limiting factor of the detector speed to be the transit time of carriers. The presented OPDs can also be integrated in photoplethysmography for real-time heart rate monitoring, suggesting its potential for practical applications.

1.5.2 Synopsis of Chapter 3

The OPDs based on inverted structure in Chapter 2 have demonstrated outstanding performance, yet not without a problem. One concern is the dark current instability issue, which is not alone found in one BHJ system. Herein, we pay attention to this universal phenomenon of undesirable sensitivity of dark current to illumination history in high-performance inverted OPDs. The phenomenon, unfavorable to attainments of high sensitivity and consistent figures-of-merit, is shown *via* systematic studies to arise from the exposure of the commonly used electron transport layer in the devices to UV light and its consequent loss of charge selectivity. A solution to this problem is proposed, which uses multilayer layer tin oxide as an alternative electron transport layer. This not only eliminates the inconsistency

between the initial and after-illumination dark current characteristics, but also preserves the low magnitude of dark current, good external quantum efficiency and rapid transient response.

1.5.3 Synopsis of Chapter 4

While the achievements in Chapter 2 and Chapter 3 endow the OPDs with excellent and reliable broadband photosensing performance, they are based on rectifying diode whose EQE cannot exceed 100%. Photomultiplication (PM) can introduce a certain gain mechanism into photodetectors, rendering them to show external quantum efficiency over 100%. Current PM-type OPDs hardly demonstrates spectral response beyond 900 nm and have relatively large operating voltage for achieving a favorable gain. Here, we present solution-processed all-rounder gain OPDs simultaneously featuring high EQE over 10^4%, broadband activity (300-1200 nm), low-voltage operation ($\leq$ 1.5 V), and a fast response speed applicable in real-time PPG applications. A systematic study shows that the gain mechanism comes from the presence of a small quantity of tetracyanoquinodimethane (TCNQ), which modifies the electronic properties both at the contact and in the bulk of the active layer. This leads to photoconduction gain with unbalanced charge transport between holes and electrons. The strategy is also applicable to other organic bulk heterojunction systems, indicating its promising versatility for further exploration.

1.6 Permissions and Attributions

Chapter 2 to Chapter 4 are adapted reproduction of the works written by the author.

1) Chapter 2 is adapted with permission from Huang *et al*, A High‐Performance Solution‐Processed Organic Photodetector for Near‐Infrared Sensing, *Adv. Mater.*, 2020, 32, 1906027. Copyright 2019, Wiley-VCH.

2) Chapter 3 is adapted with permission from Huang *et al*, Understanding and Countering Illumination-Sensitive Dark Current: Toward Organic Photodetectors with Reliable High Detectivity, *ACS Nano*, 2021, 15, 1, 1753. Copyright 2021, American Chemical Society.
3) Chapter 4 is adapted from Huang *et al*, Large-gain low-voltage and wideband organic photodetectors via unbalanced charge transport, *Mater. Horiz.*, 2020, 7, 3234 with permission from the Royal Society of Chemistry.

Chapter 2

High-Performance Near Infrared Organic Photodiode Based on Non-Fullerene Acceptor

2.1 Introduction

Near-infrared (NIR) light usually corresponds to the region of electromagnetic radiation with wavelength spanning from about 750 nm to 1400 nm. Although NIR light is invisible to human visual perception, NIR sensing finds applications in a variety of technologies, including medical monitoring,[36] quality inspection,[37] machine vision,[38] and bio-imaging.[39] NIR sensing has been conventionally realized with detectors based on single-crystal inorganic semiconductor materials (e.g. Si, Ge, GaInAs), which typically have drawbacks including costly processing, mechanical inflexibility, and sensitivity to temperature.[2,40] Photodetectors based on organic semiconductors have witnessed increasing research endeavor, especially for extending their response from visible (Vis) spectrum into the NIR spectrum, leading to novel organic photodetectors (OPDs) with improved NIR sensitivity and broadband activity. A basic precondition for fabricating OPDs with spectral response that extends into the NIR region is to incorporate a component with a sufficiently narrow optical bandgap (E_g^{opt} < 1.55 eV), allowing exciton generation by the low-energy photons. Materials including narrow bandgap conjugated polymers,[29,40,41] organic salts,[42] organic dyes,[43] and metallo-organics,[44] have been explored for this purpose and found some success in achieving spectral response tailing off beyond 1000 nm. Nonetheless, the photodetection performance is still limited by the low external quantum efficiency (EQE) due to the poor carrier generation and extraction, and large

dark/noise current related to the poorly suppressed charge transport in the dark under reverse bias.

In the pursuit of photon utilization in the NIR region, narrow bandgap non-fullerene acceptors (NFAs) have recently achieved substantial success in organic bulk-heterojunction (BHJ) systems. While the application of the BHJ concept has greatly boosted exciton dissociation and overall quantum efficiency of organic photodiodes, the drawback brought by this approach is one of the most challenging to tackle in photodetection. In BHJ OPDs, both the donor and acceptor materials may have direct contact with the anode and cathode. Even with application of charge selective layers, this scenario raises the possibility of injection of holes from the cathode to the highest occupied molecular orbital (HOMO) of the donor, and electrons from the anode to the lowest unoccupied molecular orbital (LUMO) of the acceptor under reverse bias, leading to a large undesirable dark/noise current depending on different noise mechanisms.[45,46] This can be more severe with narrow bandgap systems due to smaller injection barriers. Therefore, simultaneously achieving high NIR photoresponse and low dark/noise current with narrow bandgap materials is fundamentally challenging.

In this chapter, solution-processed BHJ OPDs with outstanding Visible-to-NIR sensing capability based on a novel NFA is demonstrated. By including the NFA with a narrow optical bandgap of ~1.19 eV, large photoresponse can be extended up to 1100 nm. To tackle the large dark/noise current commonly associated with BHJ OPDs, we have adopted a so-called “thick junction” strategy to suppress the shunt leakage and postpone the onset of charge injection current.[47] Benefiting from a well-balanced performance under illumination and dark conditions, the presented OPDs give a low dark current density on the order of nanoamperes per centimeter square even at the moderate reverse bias of -2 V, leading to a

peak shot noise-limited detectivity over 10^{13} *Jones*. With a more careful evaluation of the noise current, a high detectivity over 10^{12} *Jones* can be confirmed from 580 nm (visible) to 1010 nm (NIR), rendering these devices amongst the best high-performance broadband OPDs for Vis-to-NIR photodetection.

2.2 Materials and Thin-Film Absorption

The active layer of our OPDs contains a BHJ system that comprises a polymer donor (PTB7-Th), and a novel NFA, abbreviated as CO1-4Cl (Figure 2.1a). The general design of CO1-4Cl can be summarized by an A−D'−D−D''−A asymmetrical configuration that is based on cyclopentadithiophene (CPDT) as the central donor (D) unit flanked with two different thienyl units as the sub-donor (D' and D'') fragments, and is terminated by acceptor (A) units consisting of 2-(5,6-dichloro-3-oxo-2,3-dihydro-1H-inden-1-ylidene)malononitrile. The HOMO level of CO1-4Cl is found to be -5.36 eV vs vaccuum according to the cyclic voltammetry (Figure A2.1). The energy levels of the materials in the case of an inverted organic photodiode with ITO/ZnO as the cathode and MoO_x/Ag as the anode is depicted in Figure 2.1b. In a BHJ blend, the donor and acceptor materials have a Type II heterojunction with a staggered band alignment to create energetic offsets of HOMO and LUMO levels between the two materials, which will facilitate separation of the photogenerated charges. Strong NIR absorption can be observed from the absorption spectrum of the PTB7-Th:CO1-4Cl blend, peaking around 920 nm, which originates from the ultranarrow bandgap acceptor material, CO1-4Cl (Figure 2.1c). The E_g^{opt} of CO1-4Cl is ~1.19 eV according to the Tauc plot (Figure A2.2) derived from the absorption data. The peak in the range of 700 – 800 nm corresponds to the absorption of PTB7-Th. Together, the donor and acceptor materials potentially offer a broad spectral activity for the OPD device.

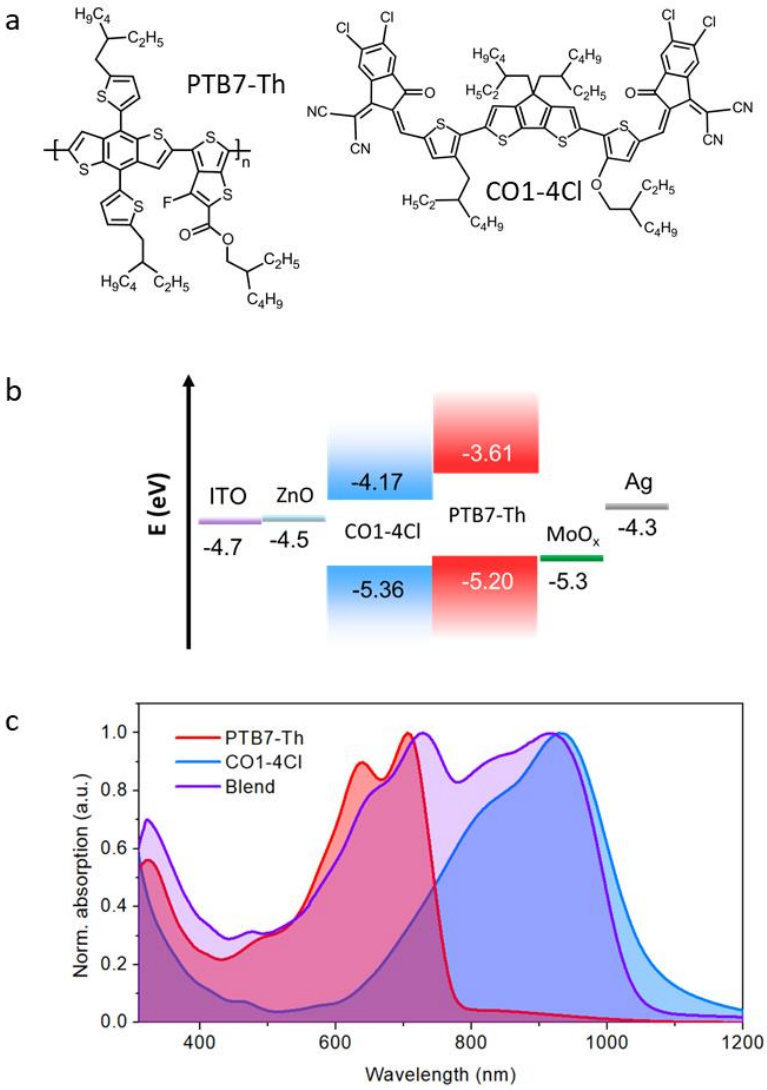

Figure 2.1. (a) Chemical structures of the donor PTB7-Th and the acceptor CO1-4Cl. (b) Energy diagram of the NIR OPD. (c) Normalized thin film absorption of the PTB7-Th (red), CO1-4Cl (blue) and their BHJ blend (purple).

2.3 Thin-Film Morphologies

2.3.1 Molecular Packing and Crystalline Features

Grazing-incidence wide-angle X-ray scattering (GIWAXS) was applied to study the molecular packing and crystalline feature of the neat films of the donor, acceptor and their

blend. The 2D GIWAXS patterns and the line-cut profiles for out-of-plane and in-plane features are shown in Figure 2.2. In Table A2.1, the detailed peak positions, stacking distance (d) and coherence lengths (L_c) are listed. The presence of intense scattering at a large q_z and small q_{xy} in both neat films (Figure 2.2a and 2.2b) indicates that both the donor and acceptor adopt face-on orientation in their neat films. The π-π stacking distance is 0.39 nm (1.63 q_z) and 0.34 nm (1.85 q_z) for PTB7-Th and CO1-4Cl, respectively. The peak for CO1-4Cl is found narrower than that of the PTB7-Th (Figure 2.2d and 2.2e), suggesting greater crystallinity. Not surprisingly, the small molecule CO1-4Cl also shows better long-range order, as reflected by larger L_c values (Table A2.1).

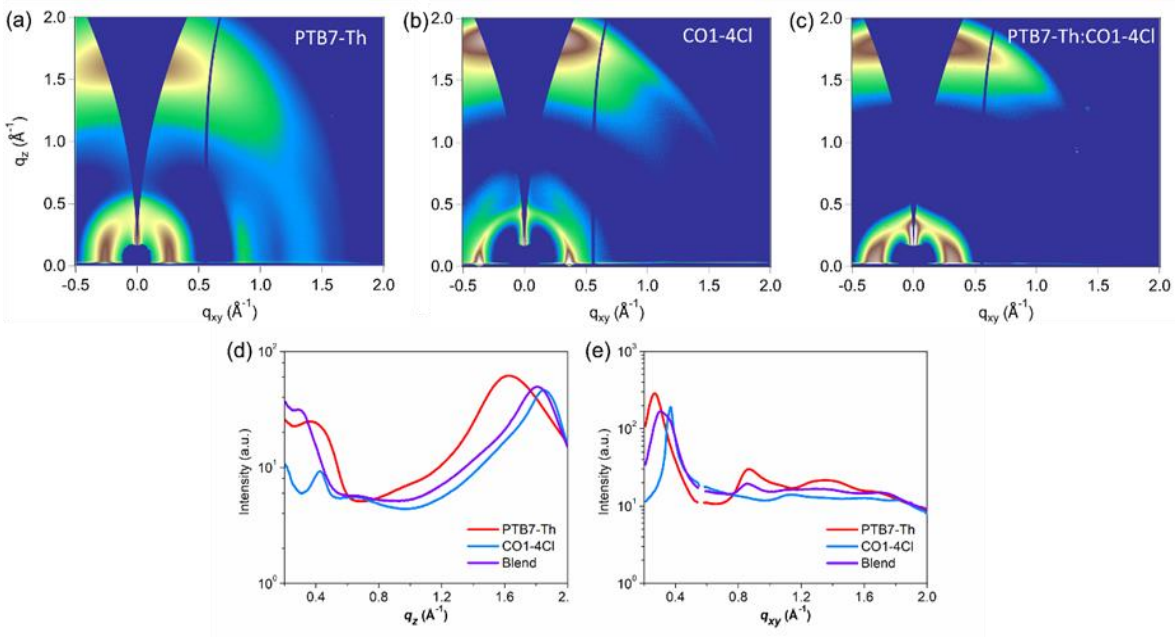

Figure 2.2. 2D GIWAXS images of the films of (a) PTB7-Th, (b) CO1-4Cl and (c) the blend. (d) Out-of-plane and (e) in-plane line-cut profiles for the neat and blend films.

For the BHJ blend, the π-π stacking of CO1-4Cl near 1.85 q_z is retained while the longer distance π-π stacking of PTB7-Th near 1.63 q_z is not present. Interestingly, the feature at 1.85 q_z has shown increased L_c value in the blend, suggesting improved long-range ordering for CO1-4Cl in the BHJ. The combination of the donor and acceptor materials in BHJ blend leads

to preferential face-on orientation and smaller π-π stacking distances, which are favorable for efficient charge transport in vertical photodetectors where photogenerated carriers are extracted in the direction normal to the substrate.[9]

2.3.2 Surface Morphology

Atomic force microscopy (AFM) is used to probe the surface morphology of the BHJ layer. For the purpose of device optimization, the active layer has been made with two thickness (~87 nm and ~300 nm). The height profiles for both films are shown in Figure 2.3. The thick and thin BHJ active layers exhibit similar surface morphologies. No clear contrast can be found to designate donor and acceptor domains as in most polymer:NFA BHJ systems, implying a well-mixed blend for PTB7-Th and CO1-4Cl. The root-mean-square (rms) roughness is slightly larger for the thick film (4.475 nm) than the thin film (3.327 nm). However, both rms thickness values are small relative to the total thickness of the active layer, being 1.49% and 3.82% of the total thickness for the thick and thin devices, respectively. This is beneficial for reducing shunt leakage related to local non-uniformity of interfaces.

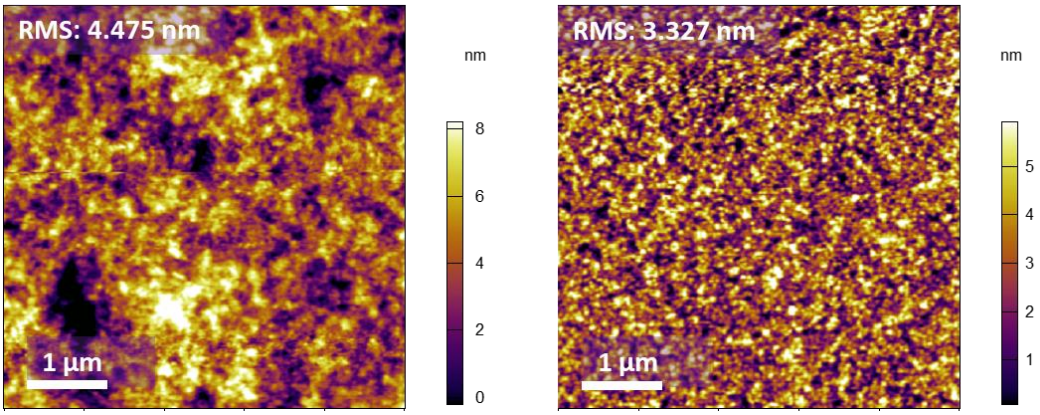

Figure 2.3. AFM images of the active layer of (left) thick and (right) thin devices.

2.4 Photoresponse

To evaluate the photoresponse performance, the EQE and responsivity (*R*) spectral response of the OPDs with both the thin and thick active layers mentioned in the previous section are presented in Figure 2.4a. As is shown, the OPDs show promising EQE values under a small reverse bias of -0.1 V, which vary from 60% – 68% in the NIR wavelength from 750 nm to 940 nm, with the thin device moderately higher than the thick device. The spectral profile of responsivity peaks around 920 nm and 940 nm, reaching 0.50 and 0.45 A W^{-1} for the thin and thick devices, respectively.

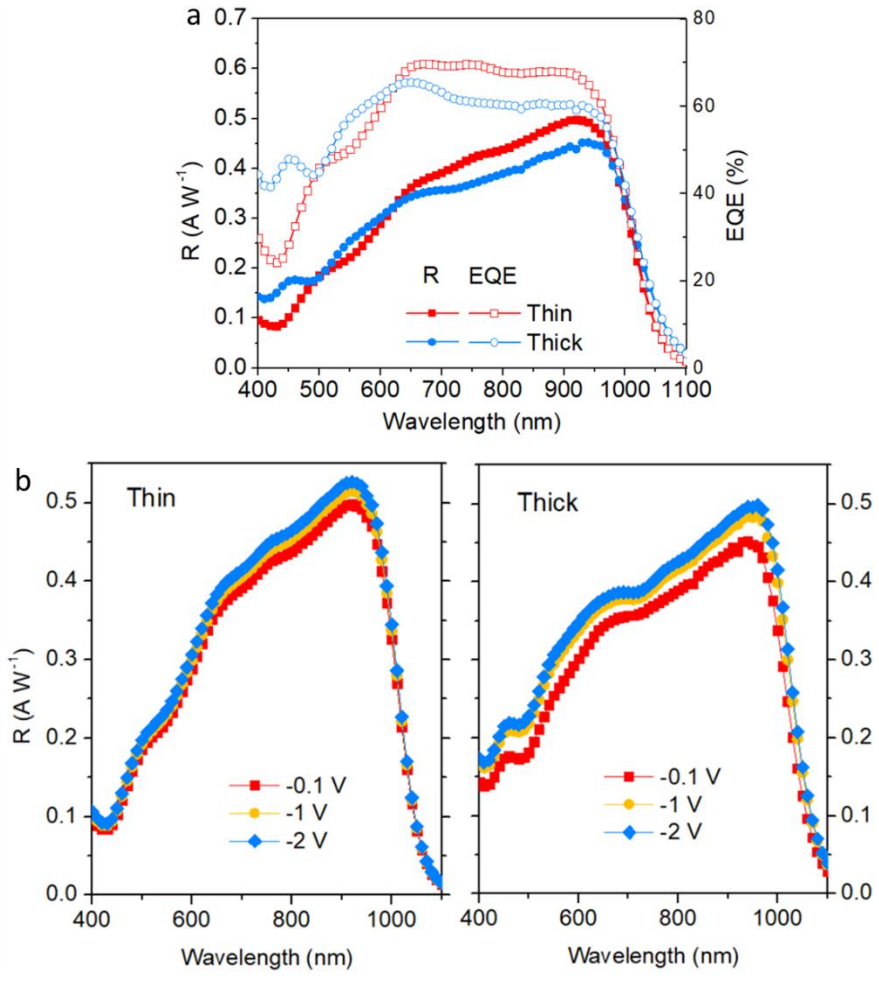

Figure 2.4. (a) EQE and responsivity profiles of the OPDs at -0.1 V. (b) responsivity profiles of the OPDs under various voltages.

With increased reverse bias, the responsivity of the photodetectors is slightly enhanced (Figure 2.4b), with the highest responsivity reached under -2 V as 0.53 A W^{-1} at 920 nm for the thin device, and 0.50 A W^{-1} at 960 nm for the thick device. The relatively small increase of photoresponse under increased reverse bias, on one hand, indicates the charge collection efficiency is already quite high even with a small external electric field, a sign of good photon-to-electron conversion for this blend system even with a large thickness. On the other hand, it suggests limited improvement of photoresponse by promoting charge collection with further increased reverse bias.

2.5 Dark Current and Shot Noise-Limited Specific Detectivity

The semi-log plot of *J-V* characteristics in the dark of the thick and thin OPD devices are shown in Figure 2.5a. Both devices show clear rectification behavior expected for p-i-n junction diodes. For photodetectors based on rectifying junction diodes, the working region is under reverse bias. Low dark current is desirable for a low noise limit and high sensitivity. The thin device shows a dark current density of 200 nA cm^{-2} at -2 V. The dark current is more effectively suppressed for the thick device, being as low as 7 nA cm^{-2} at -2 V. Figure 2.4b shows the shot noise-limited specific detectivity of both devices. Contrary to the trend in the photoresponse (Figure 2.4a), the thick device shows a larger D^*_{sh} compared to the thin device due to a smaller dark current. The D^*_{sh} spectral profiles under different biases are also shown in Figure 2.6. Despite having higher photoresponse (Figure 2.4b) under reverse bias for the thin device, the D^*_{sh} values under various reverse biases are still higher for the thick device as a result of a lower dark current.

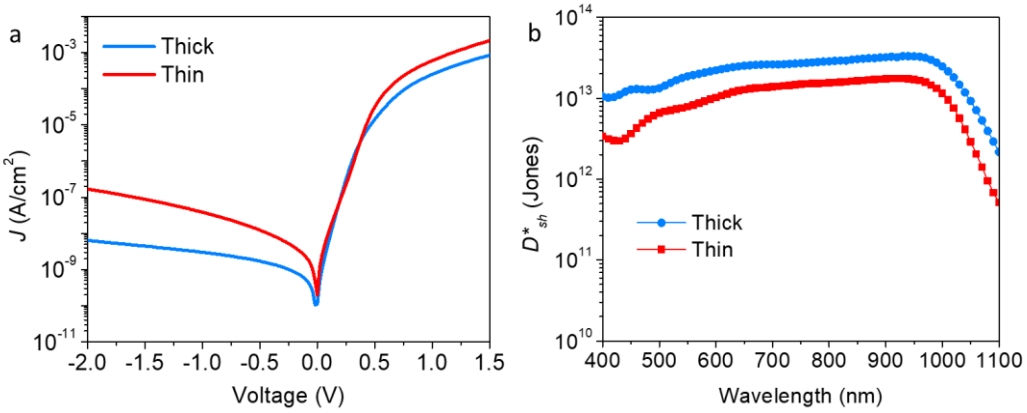

Figure 2.5. (a) Dark *J-V* characteristics and (b) shot noise-limited specific detectivity at -0.1 V of the thick and thin devices.

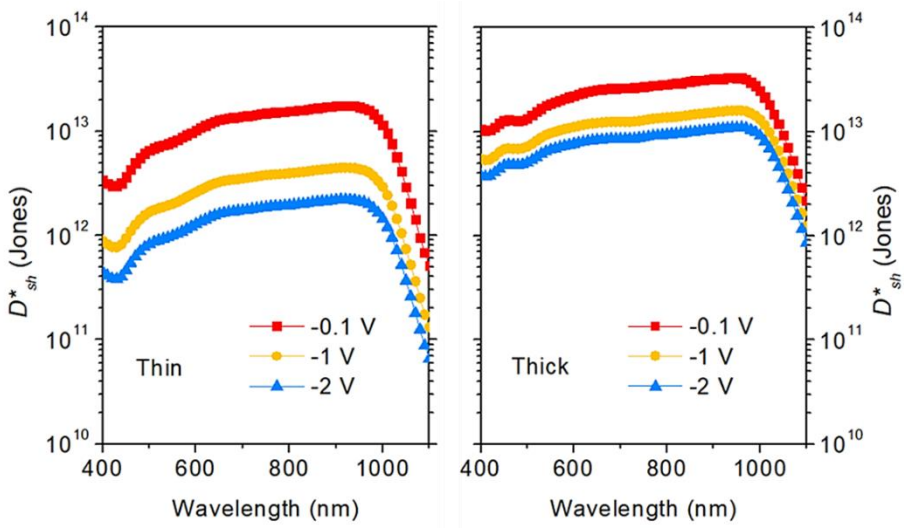

Figure 2.6. Spectral profiles of shot noise-limited specific detectivity of the thin (left) and thick (right) devices under bias of -0.1 V, -1V and -2 V.

It is easily noted that D^*_{sh} monotonically decreases as the reverse bias increases for both devices. This implies that the current characteristics in the dark, rather than the photoresponse performance, places the limit for the sensitivity. To further analyze the dark current difference between the thin and thick devices, the corrected current density-voltage (J_{corr}-V_{rev}) characteristics (Figure 2.7) are presented, with the J_{corr} calculated by:

$$J_{corr} = J - \frac{V_{rev} - JR_s}{R_{sh}} \tag{15}$$

where J is the absolute value of the apparent current density, V_{rev} is the absolute value of the applied reverse bias, R_s and R_{sh} are the area-normalized series resistance and shunt resistance, respectively.[48]

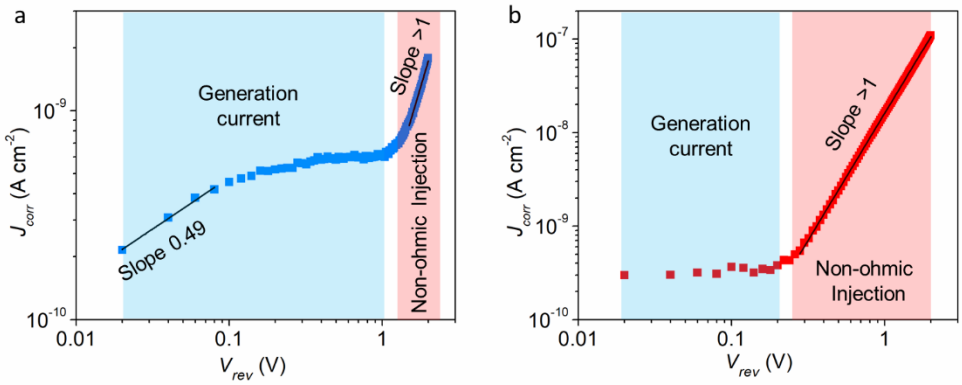

Figure 2.7. Corrected current density-voltage characteristics of the (a) thick device and (b) thin device under reverse bias.

For the thick device, the region (<0.1 V) where J_{corr} is proportional to the square root of V_{rev} corresponds to the charge transport mechanism of generation current.[49,50] With increased reverse bias, J_{corr}-V_{rev} becomes relatively flat due to the saturated generation current at the fully depleted active layer. Upon further increasing the reverse bias to larger than 1 V, the slope of the logarithmic J_{corr}-V_{rev} curves becomes larger than 1, which indicates non-ohmic injection that deviates linear dependence of current on voltage. For the thin device, the active layer is already fully depleted even at very small reverse bias, as can be seen from the flat J_{corr}-V_{rev} curve under the reverse bias less than 0.2 V. The onset voltage for the non-ohmic injection region is about 0.23 V, much smaller than that of the thick device. Although the thick device has a larger generation current due to its larger thickness of the active layer, the suppressed super-linear voltage-dependent injection makes the total dark current in the thick device much smaller and more favorable for high detectivity applications.

*2.6 Noise Spectrum, NEP and D**

While the shot noise estimated from the dark current is convenient, its use only provides the theoretical high limit of D^* and therefore comes with the risk of performance overestimation.[30,51] We therefore further probed the noise spectral density (S_n) of our OPDs (Figure 2.8) with fast Fourier transform of the dark current at -0.1 V and -2 V, respectively.

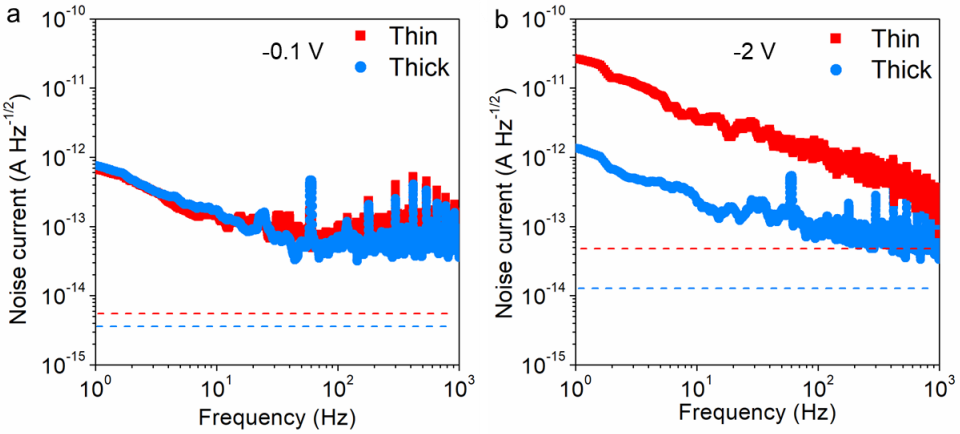

Figure 2.8. Noise spectra of the OPDs at reverse bias of (a) -0.1 V and (b) -2 V, the dashed lines are the shot noise limit for the thin device (red) and the thick device (blue).

When the bias is relatively small (Figure 2.8a), the noise level is similar for both the thin and thick devices, which show a decreasing trend with frequency up to ~70 Hz. In the frequency independent region, the thin device has a slightly higher noise, around 8.5×10^{-14} A Hz$^{-1/2}$ at 100 Hz, while it is around 5.9×10^{-14} A Hz$^{-1/2}$ for the thick device. Under a higher bias of -2 V, S_n slightly increases for the thick device, giving 1.0×10^{-13} A Hz$^{-1/2}$ at 100 Hz. However, a significant increase of S_n for the thin device is seen over the frequency range, with the frequency-dependent region widened up to 1 kHz. As a result, the S_n at 100 Hz goes up to 1.23×10^{-12} A Hz$^{-1/2}$, corresponding to an increase by over two orders of magnitude. Therefore, at the frequency of 100 Hz, the thick device has an NEP of 1.2×10^{-13} W Hz$^{-1/2}$ at -0.1 V, and still holds as low as 2.0×10^{-13} W Hz$^{-1/2}$ at -2 V. It is noticeable that at low bias (-0.1 V) in the

low-frequency region (<100 Hz), the large noise may not be necessarily related to the properties of the OPDs, but rather reflects the large background noise of the whole circuitry that awaits optimization (Figure A2.3).

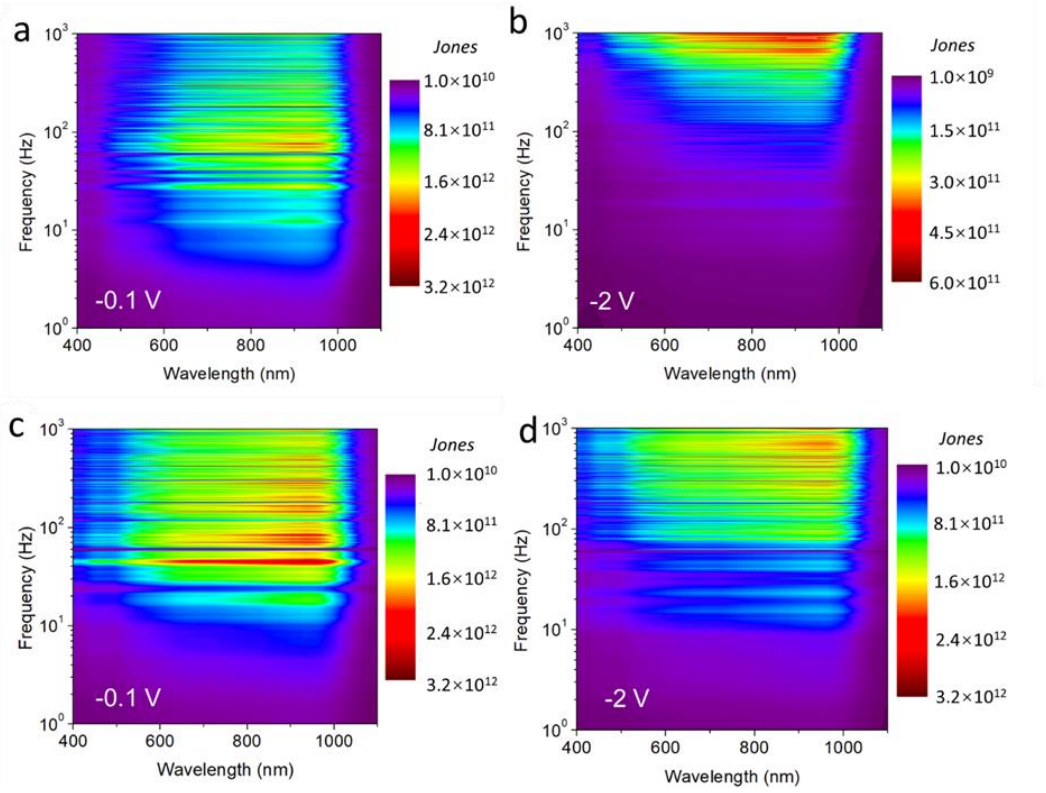

Figure 2.9. Specific detectivity (*D**) as a function of frequency and incident light wavelength for the thin device at (a) -0.1 V and (b) -2 V, and for the thick device at (c) -0.1 V and (d) -2 V.

With the measured noise spectra, the contour plot of specific detectivity (*D**) as a function of both frequency and wavelength can be derived (Figure 2.9). At a small bias of -0.1 V, even at a low frequency where flicker noise is significant (10^{-13}-10^{-12} A $Hz^{-1/2}$, Figure 2.8a), the values for *D** in the whole wavelength range (400 to 1100 nm) are over 10^{10} *Jones* for both devices (Figure 2.9a and 2.9c). In the frequency-independent region, an overall *D** higher than 10^{12} *Jones* in the NIR range from 750 nm to 980 nm is achieved for both devices due to their high responsivity and relatively low noise (<10^{-13} A $Hz^{-1/2}$). At a larger bias of -2 V, the

overall enlarged noise level results in a decrease of D^* to below 10^{12} *Jones* for the thin device. The maximum D^* is around 5×10^{11} *Jones*, achieved at the highest tested frequency around 1 kHz (Figure 2.9b) as a result of the widening of the frequency-dependent region of the noise spectrum (Figure 2.8b). This widening presents more dominant flicker noise, which is usually believed to originate from trapping and detrapping of carriers.[26] The result aligns well with the dramatically increased dark current under large bias, where the trapping and detrapping events become more apparent with large number of carriers being transported through the device. Differently, thick device is still able to uphold D^* over 10^{12} *Jones* in the original wavelength range with suppressed noise current (Figure 2.9d).

2.7 Linear Dynamic Range (LDR)

The photocurrent as function of the incident light intensity is shown in Figure 2.10 for the thick and thin devices, which give LDR of 126 dB and 148 dB, respectively. For both devices, a saturation region of photocurrent at the higher end of light intensity is found. Such sub-linearity between photoresponse and incident light intensity is usually associated with the effect of enhanced charge recombination higher photogeneration rate and larger concentration of photogenerated carriers.[30,52]

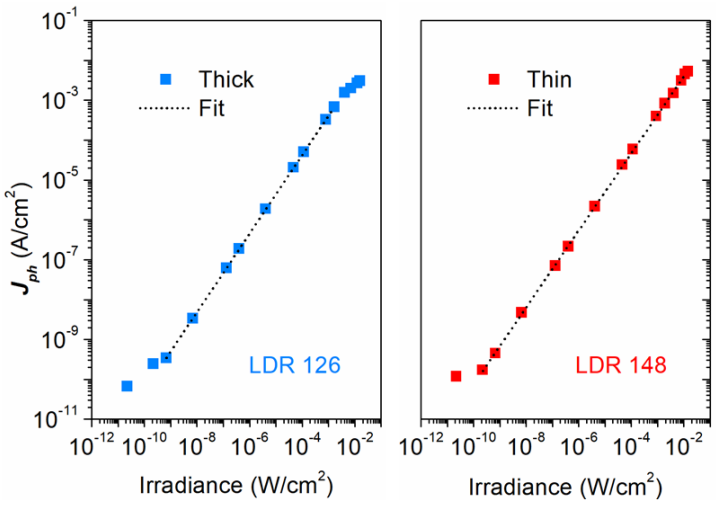

Figure 2.10. Photocurrent density vs irradiance of incident light for the OPDs at -0.1 V illuminated under of 940 nm monochromatic light.

In this regard, the thin device shows better linearity, which has upper limit of linearity of ~11 mW/cm^2, much larger than 1.67 mW/cm^2 of the thick device. It can be understood that the holes and electrons in the thick device need to traverse a larger distance to be collected at anode and cathode, respectively. In the competition between charge extraction and charge combination, the larger transit distance favors the latter. Therefore, more photogenerated carriers are lost in the thicker film and a lower photocurrent is resulted.

2.8 Phototransient Behavior

2.8.1 Frequency-Modulated Response and Cutoff Frequency

To evaluate the response speed of the OPDs, the phototransient behavior of the devices was studied. For enhanced charge extraction and faster operation, photodetectors are usually reversely biased at a relatively large bias. Therefore, the thick device operating under a reverse bias of -2 V is concerned here for its better balance between the photoresponse and noise characteristics, and the consequent superior *D**. In Figure 2.11a, the current density as a

function of time for the thick device under 940 nm infrared light modulated at 20 kHz (upper) and 200 kHz (lower) is shown, respectively. In the former case, the output of the photodetector can follow the on-off switching of the optical signal and reach the steady-state photocurrent and dark current. When illumination modulation is at 200 kHz, the photodetector is not able to fully reach the original photocurrent or decay to the dark current due to the limited response speed. An important parameter to evaluate the applicable bandwidth of a photodetector is the cutoff frequency (f_{3dB}), commonly defined as the frequency at which the output of a detector is attenuated to -3 dB, corresponding to 70.8% of the original amplitude. The temporal photoresponse at various light modulation frequencies is shown in Figure 2.11b. The f_{3dB} is found to be around 240 kHz.

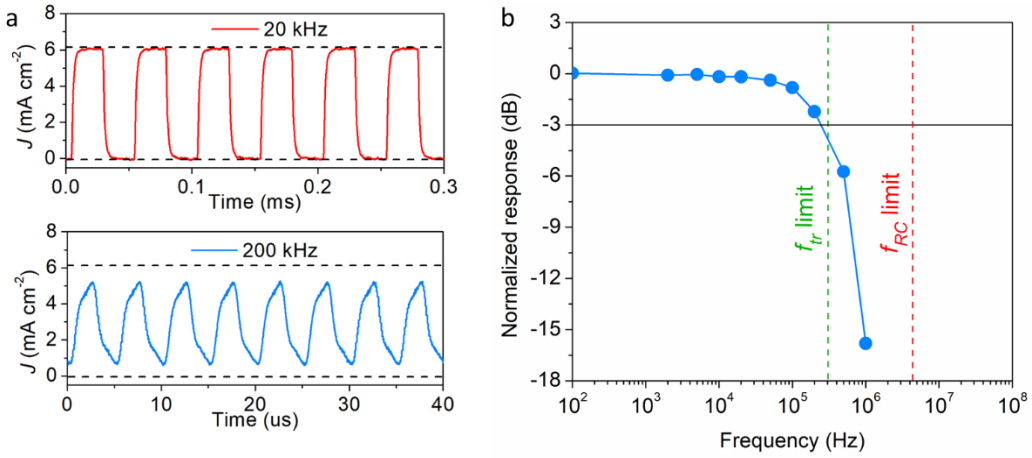

Figure 2.11. (a) Phototransient response of the thick device under light modulation frequency of 20 kHz (upper) and 200 kHz (lower) at -2 V. The black dashed lines indicate the steady-state current levels under illumination and in the dark. (b) Normalized response as a function of frequency. The dashed lines indicate the theoretical cutoff frequency limited by transit time (green) and RC time constant (red).

2.8.2 Limiting Factors of Photoresponse Speed

In order to understand the limiting factors of the photoresponse speed, two main limiting mechanisms are examined. First is the RC time constant of the system. The RC time constant-limited cutoff frequency (f_{RC}) can be calculated by:[53]

$$f_{RC} = \frac{1}{2\pi R_{sum} C} \tag{16}$$

where the R_{sum} is the sum of the series resistance (R_{series}) of the device (measured to be ~62 Ω), and the load resistance of the oscilloscope (50 Ω), and C is the junction capacitance of the device, estimated to be ~0.34 nF from the high-frequency capacitance under -2 V (Figure 2.12). Hence, the corresponding f_{RC} is calculated to be 4.18 MHz (red dashed line in Figure 2.11b), which is much larger than the experimentally measured ~240 kHz. This indicates the limiting factor of the response speed is not the RC time constant.

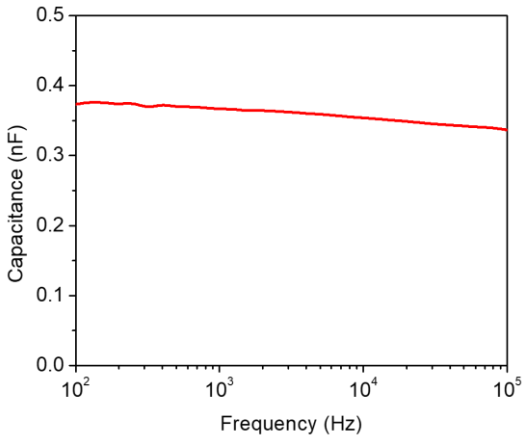

Figure 2.12. Capacitance vs frequency of the thick device under -2 V.

The other possible limiting factor is due to the time required for the photogenerated charges to transit the thickness of the active layer. The transit time-limited cutoff frequency (f_{tr}) is estimated by:[53]

$$f_{tr} = \frac{3.5}{2\pi\tau_{tr}} = \frac{3.5\mu_{eff}(V + V_{bi})}{2\pi L^2} \tag{17}$$

where τ_{tr} is the transit time of the charge carriers, μ_{eff} is the effective carrier mobility, V is the applied bias, V_{bi} is the built-in voltage, and L is the thickness of the active layer. To obtain the mobility, the hole and electron mobilities are first extracted from the $J^{1/2}$-V characteristics (**Figure 2.13**) of the hole-only and electron-holy single-carrier diodes, respectively. The hole and electron mobilities are extracted according to the Mott-Gurney law:[54]

$$J = \frac{9\varepsilon_r\varepsilon_0\mu(V - V_{bi})^2}{8L^3} \tag{18}$$

where J is the current density of the single-carrier diode, ε_r is the dielectric constant of the active layer, ε_0 is the vacuum permittivity, μ is the carrier mobility, V is the applied voltage, V_{bi} is the built-in potential, and L is the thickness of the active layer.

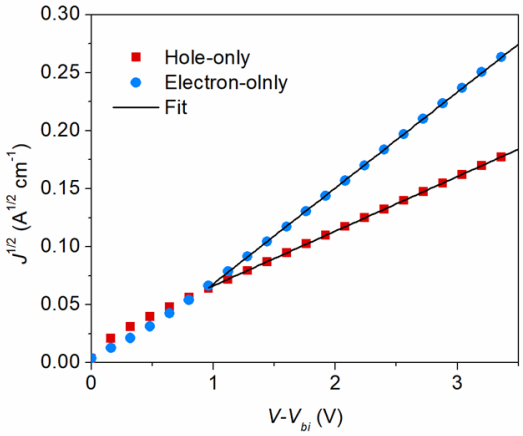

Figure 2.13. $J^{1/2} - V$ characteristics of the single carrier diodes with PTB7-Th:CO1-4Cl as the active layer.

The hole mobility (μ_h) and electron mobility (μ_e) are found to be 1.19 × 10^{-4} cm^2 V^{-1} s^{-1} and 3.26 × 10^{-4} cm^2 V^{-1} s^{-1}, respectively. The effective mobility (μ_{eff}) is defined according to the work by *Neher et al*:[55]

$$\mu_{eff} = \frac{2\mu_n\mu_h}{\mu_n + \mu_h} \tag{19}$$

The μ_{eff} is calculated to be 1.74 × 10^{-4} cm^2 V^{-1} s^{-1}, which corresponds to a τ_{tr} of 1.82 μs and a calculated f_{tr} value of 306 kHz (indicated by the dashed green line in Figure 2.11b). This

value is fairly close to the experimentally determined value of ~240 kHz. These results suggest that the limiting factor for the photoresponse speed of the present OPDs is the carrier transit time.

2.9 Application for Photoplethysmography

A simple photoplethysmography (PPG) measurement is conducted to showcase the application of the NIR OPDs in real-time healthcare monitoring. For a typical PPG test, a photodetector device collects the light signal that has been reflected/scattered by the human body part (Figure 2.14a). Due to the volume change of the blood vessels and the density fluctuation of the light-absorbing blood hemoglobin during cardiac cycles, the intensity of the light that a nearby photodetector receives is modulated by the contraction and expansion of the vessels, which can lead to a small 'AC' signal.[56] One of the functions of this non-invasive optical method is monitoring the pulse and determining the heart rate (HR). The PPG signal from a volunteer was measured at his resting and after-exercise conditions, respectively (Figure 2.14b). In both cases, the typical systolic and diastolic peaks in a PPG profile can be identified. By dividing 60 s by the averaged inter-beat interval (IBI) in each case, the HR was determined to be 67 and 106 beats per minute for the volunteer at resting and after-exercise conditions, respectively.

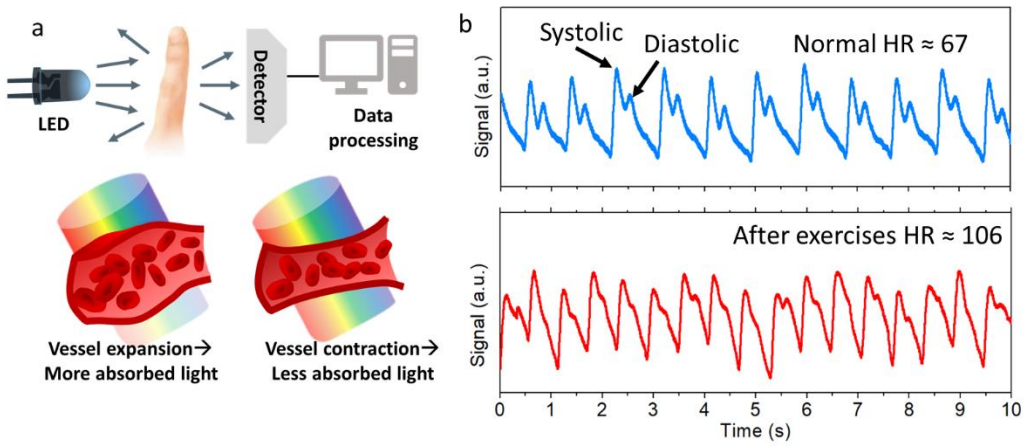

Figure 2.14. (a) Test setups and working principles of PPG. (b) Pulse signal measured from the OPD at normal (upper) and after-exercise (lower) conditions.

2.10 Experimental

2.10.1 Device fabrication

For inverted structure devices, glass substrates with pre-patterned indium tin oxide (ITO) were ultrasonicated in deionized water, acetone and 2-propanol for 10 min, respectively. The zinc oxide layer was prepared from a diethyl zinc and tetrahydrofuran solution (1:2, v/v) spun onto the cleaned ITO substrates at 4000 rpm for 15 s and annealed at 110 ℃ for 15 min. This ZnO deposition process was done twice. Subsequently, the blend solution of PTB7-Th:CO1-4Cl (1:1.5 weight ratio) in chlorobenzene:1-chloronaphthalene (98:2, v/v) with different concentrations of 15 g L^{-1} and 35 g L^{-1} was deposited by spin-coating at 1000 rpm, followed by vacuum deposition (< 10^{-6} torr) of 15 nm MoO_x and 100 nm Ag to form the hole transport layer and the anode electrode. The devices prepared from the active layer solution of the two different concentrations (15 g L^{-1} and 35 g L^{-1}) are referred to as thin and thick devices, respectively. To make the hole-only diodes, the blend solution was spun on the ITO substrates covered with poly(3,4-ethylenedioxythiophene)polystyrene sulfonate (PEDOT:PSS) and the

top electrode was 7 nm MoO_x and 100 nm Ag thermally evaporated onto the active layer. For the electron-only diodes, the deposition of ZnO layer and BHJ layer on the ITO substrates were prepared in the same way as in the photodetector devices. To make the top electrode, aluminum-doped ZnO nanoparticle ink in 2-propanol (Sigma-Aldrich) was spun onto the active layer at 4000 rpm for 15 s, followed by thermal evaporation of 100 nm Al.

2.10.2 Thin-Film Characterizations

Cyclic Voltammetry (CV) experiment was conducted on a CHI-730B electrochemistry workstation with the three-electrodes system consisting of glassy carbon disk, Pt wire, and Ag wire electrode which serve as the working electrode, counter electrode, and pseudo reference electrode, respectively. The measurement was performed in 0.1 M tetrabutylammonium hexafluorophosphate (*n*-Bu_4NPF_6)-anhydrous acetonitrile solution at a potential scan rate of 100 mV s^{-1}. Thin film of the sample was deposited onto the glassy carbon working electrode from its 5 mg mL^{-1} chloroform solution. The electrochemical onset was determined at the position where the current starts to differ from the baseline. The potential of Ag pseudo reference electrode was internally calibrated relative to Fc/Fc+ couple (−4.88 eV vs. vacuum).

The thin-film absorption spectra of the PTB7-Th, CO1-4Cl and the BHJ blend were taken from on a LAMBDA 750 UV/Vis/NIR spectrophotometer (Perkin Elmer). The films were spun from chlorobenzene solution onto UV ozone-treated quartz substrates.

The AFM topographic surface morphology measurements were obtained from an Asylum MFP-3D operating in closed loop mode mounted atop an Olympus inverted optical microscope under an inert atmosphere, using the as-prepared OPD devices as the samples to probe the morphology of the BHJ layer. Pt/Cr coated silicon AFM tips with a resonant frequency of ~13 kHz and a force constant of ~0.2 N m^{-1} were used (Budget Sensors). First-

order image flattening and subsequent image analysis were performed on the morphology images on Asylum Research AFM software version 14, programmed using IGOR Pro.

The GIWAXS measurement was conducted at the Advanced Light Source at Lawrence Berkeley National Lab on the 7.3.3 beamline. The sample was scanned with an incidence angle of 0.12° and a photon energy of 10 keV (λ = 1.24 Å), while under a helium environment to minimize beam damage and reduce air scattering. The width of the incident X-ray beam is about 1 mm, and silver behenate was used to calibrate the lengths in the reciprocal space. A 2D detector (PILATUS 2 M from Dectris) with a sample-to-detector distance of 276.9 mm was used to collect the images. The Nika software package for Igor (by Wavemetrics) and the Igor script WAXStools were used to process the image.

2.10.3 Device Characterizations

The *I-V* characteristics were obtained with a Keithley 4200 semiconductor characterization system. The EQE measurements were performed with a setup of 75-watt Xeon light source coupled with a monochromator and an optical chopper, calibrated with a reference photodiode (NIST-calibrated Newport 818-UV Si photodiode). The photocurrent was recorded with an SR810 DSP lock-in amplifier (Stanford Research System) at 155 Hz. The noise measurements of the devices were done in the dark employing a battery-powered pre-amplifier (SRS 570) coupled with an oscilloscope (Keysight DSOX3022T) operated with an internal fast Fourier transform function. For linear dynamic range measurement, a set of 940 nm LEDs were used as the light source and a series of calibrated filters were used to modulate the incident light intensity together with the adjustment of the current run through the LEDs. The transient photoresponse measurements were conducted with a 940 nm LED as

the light source and a function generator as source of pulse signals. The output of the OPDs were amplified with a pre-amplifier and recorded with an oscilloscope.

Chapter 3

Understanding and Countering Illumination History – Sensitive Dark Current in Inverted Organic Photodetectors

3.1 Introduction

In the pursuit of high-performance photosensing toolbox and optical communications based on organic photodetectors (OPDs), two core figures-of-merit of photodetectors have received extensive research attention. The first is the response of the device to light, usually presented with the value of external quantum efficiency (EQE). The second, and not any less important than the first one, is the dark current under the operation condition, which is usually reverse bias for rectifying junction-based photodiodes. The EQE marks how efficient the light-to-current conversion is, and therefore directly determines the magnitude of the obtainable electric signal under a given intensity of the incident light. The dark current sets a theoretical minimal level for the noise limit of the detectors. As discussed in the previous chapters, they altogether determine the specific detectivity. In general, large EQE and low dark current are pursued. For optimized systems, the EQE values are usually in the range of several tens of percent in their respective spectral active regions for the OPDs without special photomultiplication gain. In contrast, the dark current can vary in a large range spanning several orders of magnitude, often making it the determining factor of the specific detectivity and limit of detection. Therefore, the successful suppression of the dark current, especially under that under larger bias for the sake of faster operating speed, holds the key to enabling low noise level and high sensitivity of organic photodetectors. Encouragingly, low dark current as low as several nanoamperes per square within a reverse bias of 2 V has been

documented for even for OPDs involving materials of very narrow bandgap (~1 eV).[57–59] The robust performance upgrade have prompted commercialization of organic photodetectors from initial lab-scale exploration to serious industrial efforts.[12,60]

Contrast to the success in lowering the dark current of organic photodetectors, studies for understanding and improving the stability and reliability of organic photodetectors are concerningly scarce, although stability of the device performance is critical for commercialization of organic photodetectors. Different from organic photovoltaics in function, organic photodetectors require not only stability of performance parameters under the illumination condition like photovoltaic devices, but also emphasize the figures-of-merit under the dark condition, particularly the dark current. To establish reliable detection figures-of-merit, it is necessary that the dark current characteristic of the photodetectors should have consistent magnitude regardless of the illumination history of the device, namely, similar level before and after illumination. Interestingly, heed and inspection to this aspect of dark current, despite being essential for reliable device operation, have been rather rare in the literatures.[61,62]

In this chapter, the focus will be placed on the impact of illumination history on the stability of the figures-of-merit of high-performance organic photodetectors. More specifically, we will investigate and address the phenomenon where the dark current of the organic photodetectors is found to significantly increase after the devices are subject to illumination. The factors that contribute to this undesirable phenomenon are identified through a series of systematic control experiments, and a remedy using an alternative electron transport layer material, tin oxide, has been provided accordingly. With the sensitivity of dark current to the illumination history largely eliminated, the low magnitude of the dark current well preserved, and the originally

excellent photoresponse uncompromised, the organic photodetectors can feature both large and reliable specific detectivity.

3.2 Illumination History – Sensitive Dark Current

The main focus is placed on a BHJ system with broadband absorption (Figure 3.1a), which contains a polymer donor (poly[4,8-bis(5-(2-ethylhexyl)thiophen-2-yl)benzo[1,2-b;4,5-b']dithiophene-2,6-diyl-alt-(4-(2-ethylhexyl)-3-fluorothieno[3,4-b]thiophene-)-2-carboxylate-2-6-diyl)], PBT7-Th) and a non-fullerene small-molecule acceptor, named as CO1-4Cl.[58] This D-A blend has also been studied in Chapter 1. A typical inverted structure is adopted for the organic photodiode device (Figure 3.1b). The reverse bias *J-V* curves in the dark before and after illumination are shown in Figure 3.2. Prior to exposure to the illumination the device shows very low initial dark current of less than 10 nA/cm^2 up to -1.2 V. However, after the device is subject to a 60-second illumination process from a Xeon lamp (~1$\times$ 10^{-1} W/cm^2, the default setting for the "illumination" process mentioned in Chapter 3 unless otherwise noted), the dark current shows a dramatic increase, by more than 2 orders of magnitude at -1 V. Such a change is unfavorable to the photodetection performance. Assuming the shot noise as the dominant source of noise, the shot noise-limited specific detectivity (D^*_{sh}) can be estimated according to the following equation:

$$D^*_{sh} = \frac{EQE \cdot q\lambda}{hc\sqrt{2qJ_d}} \tag{20}$$

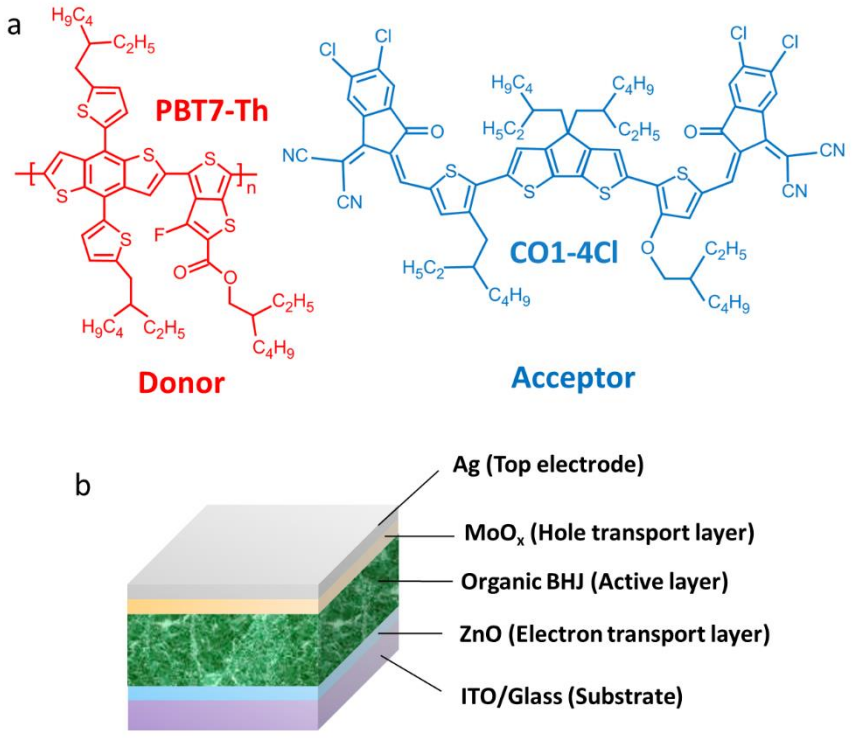

Figure 3.1. (a) Chemical structures of the active layer materials PBT7-Th and CO1-4Cl. (b) (b) Device structure of the OPDs.

where J_d is the current density in the dark. The increase of J_d will result in a drop of D^*_{sh} by more than one order of magnitude under -1 V. It is worth mentioning that this estimation only considers the shot noise alone, meaning this is the minimum loss for actual D^*. A larger dark current may also negatively impact other noise components, such as flicker noise, which is ascribed to trapping and de-trapping of the charge carriers traversing the device, and in turn further undermining the detector sensitivity.

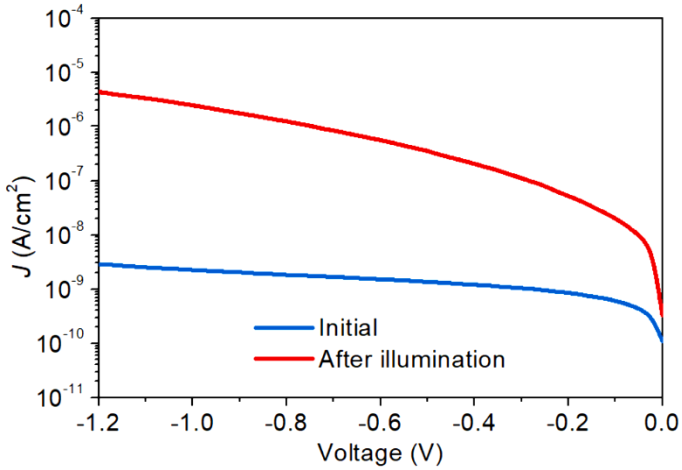

Figure 3.2. Initial and after-illumination dark *J-V* curves.

After observing the increase of the dark current caused by illumination, a question naturally comes as whether such a change is permanent or not. If the answer is positive, then stabilized figures-of-merit may still be established when such changes are permanently finished, although with the sacrifice of detector performance.

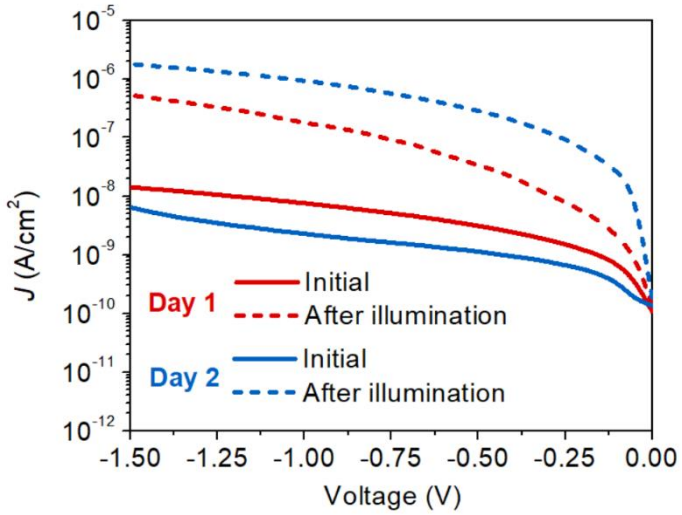

Figure 3.3. Dark *J-V* characteristics before and after illumination, measured on the day of device fabrication (Day 1, red) and the next day (Day 2, blue), respectively. Day 1 is the day when the device was prepared and Day 2 is the next day.

Unfortunately, it has been found that the large dark current induced by illumination history will disappear after leaving the device alone for a while, and can show up again if another

illumination process is introduced, indicating that the behavior is repeatable and stable sensing figures-of-merit cannot be established by a one-time pre-treatment (Figure 3.3). Therefore, the illumination-induced inconsistency issue cannot be simply circumvented by accepting a worse dark current after illumination.

3.3 External and Internal factors

To solve the problem, we first sought to understand the problem. We noticed similar behaviors have been observed in previous reports on devices containing ZnO.[63–65] Although the scopes of these works differ from ours, their results point to the exposure of ZnO components to high energy (i.e., UV) photons as the cause behind the observed behavior. To confirm that, two sets of control experiments were conducted.

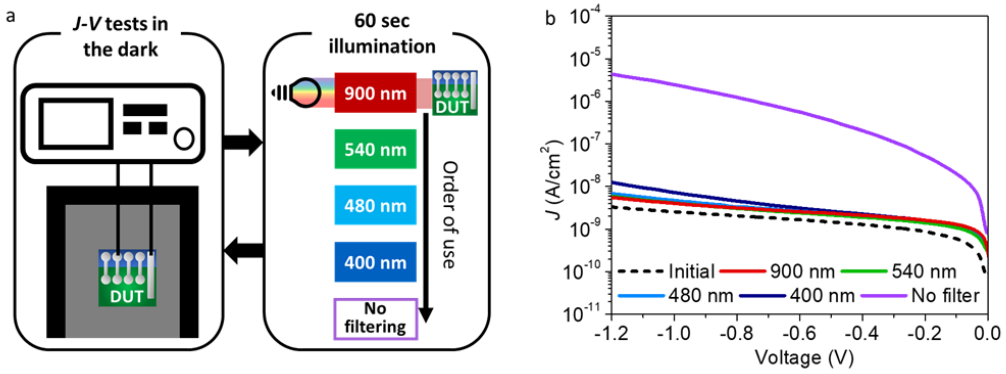

Figure 3.4. (a) Procedure for the control experiment on a freshly made device: *J-V* curve measurements and illumination processes with different long-pass filtering were repeatedly carried out. (b) Corresponding dark *J-V* curves after each illumination process. The dashed line indicates the initial dark current before any illumination processes.

The first part examines the effect of the components of light, where a freshly made OPD device was subject to illumination with long-pass filtering of different wavelength cutoffs, beginning from longer wavelength to shorter wavelength. The photons whose wavelength is below the cutoff thresholds were blocked. After each 60-second illumination process, the dark *J-V* characteristics were immediately collected before the next illumination process (Figure

3.4a). The processes were repeated until the last no-filtering run was done. The corresponding dark *J-V* characteristics are summarized in Figure 3.4b. As clearly seen, only very small change is observed after illumination with wavelength over 400 nm, while the dark current increases greatly after illumination without filtering. To ensure the observed change is not resulted from the bias aging during the repeated bias sweeping in the *J-V* measurements, the steady-state current at -1 V was also measured before, during and after roughly 30-sec illumination processes with different long-pass filtering (Figure A3.1a). Again, only when UV light was involved in the last run did the dark current exhibit dramatic increase compared to the initial level, agreeing well with the *J-V* characteristics in Figure 3.4b. A similar process using 365 nm UV light for illumination has also yielded similar result (Figure A3.1b). The results here suggest that the UV (possibly with some deep violet) part of the illumination triggers the striking change of the dark current.

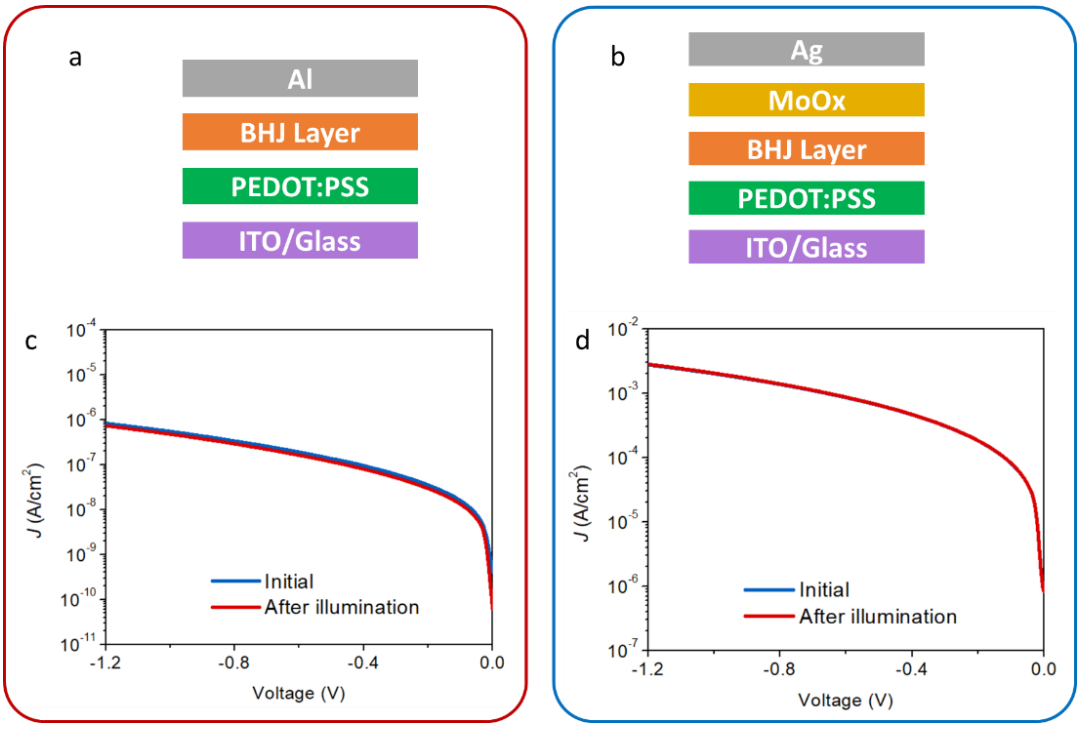

Figure 3.5. (a-b) Device structures and (c-d) dark *J-V* curves of the control group devices.

After confirming the involvement of UV in the observed behavior, control tests were carried out to find the ZnO interlayer responsible. OPDs with conventional device configuration (ITO/PEDOT:PSS/Active Layer/Al) were prepared (Figure 3.5a). The dark current characteristics before and after illumination show negligible difference (Figure 3.5c). This suggests that the issue is not from the BHJ active layer, which is the identical part in the inverted and conventional configurations. Subsequently, devices with the configuration of ITO/PEDOT:PSS/Active Layer/MoO_3/Ag were also made (Figure 3.5b). Again, the dark current shows negligible change in dark current before and after the illumination (Figure 3.5d), exempting the molybdenum oxide from the suspicion. These results of the control groups altogether point to the use of ZnO interlayer and its exposure to UV illumination as the cause of the observed phenomenon. It is noted that the devices with ZnO interlayers prepared by other approaches show a similar behavior (Figure 3.6).

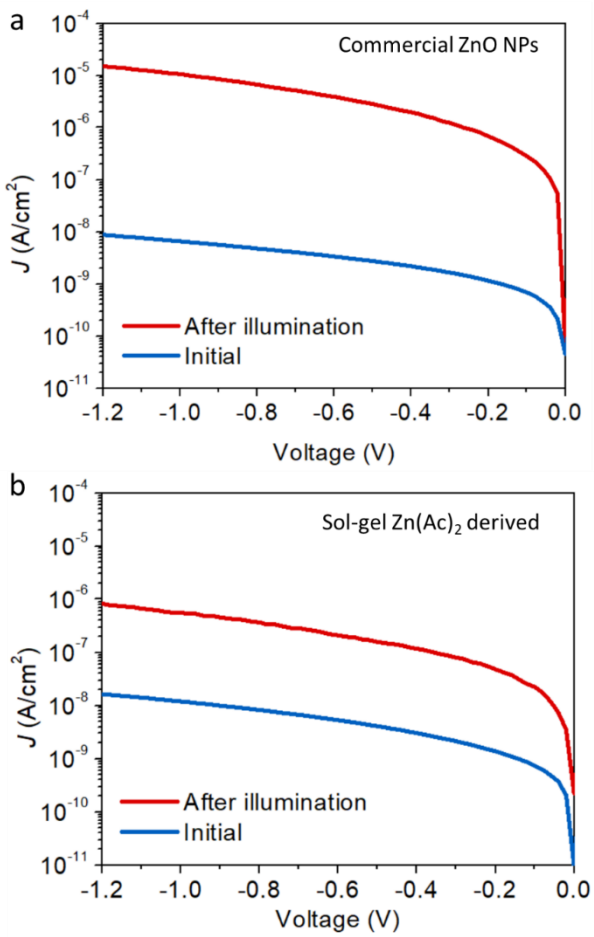

Figure 3.6. Dark *J-V* characteristics of the inverted OPDs with ZnO interlayer prepared by different methods: (a) commercial ZnO nanoparticles (NPs) suspension and (b) zinc acetate-based sol-gel method.

Other works on organic solar cells,[65] organic-inorganic hybrid diodes,[66] and photomultiplication sensors[63] have likewise shown the increased dark current associated with the effect of UV on the ZnO component in their devices, further implying universality of the phenomenon.

3.4 Criteria for Alternative Electron Transport Layers

Following the identification of the origin of inconsistency in the dark current, a counterstrategy should be considered. Arguably, the issue can be simply tackled by implementing a UV filter. However, this not only increases the cost and weight of the devices, but also deprives OPDs of UV sensing ability in the first place. Another "cheesy" approach would be using the conventional structure. This brings us back to the motivation of invention of the inverted structure organic photodiode and its advantages over conventional structure devices in the aspects of stability, performance and manufacturing, for which we would direct readers to earlier works.[67,68] In addition, under the same processing condition for the organic active layer, the dark current of the conventional structure device (Figure 3.5c and Figure A3.2) was found to be much higher compared to that of ZnO-based inverted devices before UV illumination, as was also observed in the reports.[58,69] Consequently, a proactive solution is needed to enable reliable high-detectivity photosenisng by inverted OPDs. In search of an alternative to replace ZnO (or other UV-sensitive materials, e.g. TiO_2[70]), four major criteria must be met. Foremost on this particular issue, it must make the detector to exhibit minimal sensitivity of dark current toward prior (UV) illumination. Secondly, the after-illumination dark current must be kept well suppressed, being not significantly larger than what is achievable in ZnO interlayer-based devices without UV illumination. Thirdly, the alternative should not significantly undermine the photoresponse, that is, similar EQE should be obtained. Last but not least, the alternative that can lead to major decrease of response speed should be avoided.[71]

3.5 Tin Oxide as the Alternative

Through extensive screening of commonly used materials for electron transport layer (ETL) in organic optoelectronics, we determined that the solution-processed tin oxide (SnO_2) is a promising candidate.

3.5.1 Material Characterizations

The detailed preparation procedure for the tin oxide layer can be found in the experimental section. To evaluate the chemical states of the tin oxide films, X-ray photoelectron spectroscopy (XPS) is employed. Figure 3.7a shows a Sn 3d spectrum with the characteristic peaks of element Sn at 487.37 eV (Sn $3d_{5/2}$) and 495.85 eV (Sn $3d_{3/2}$), respectively, agreeing well with the previous reports.[72–74] A spin-orbit coupling of 8.48 eV is found, implying the existence of Sn (IV).[75] The O 1s spectrum (Figure 3.7b) can be deconvoluted into two signals at 531.10 eV and 532.34 eV, which may be ascribed to the O^{2-} species in SnO_2, and chemisorbed oxygen or hydroxyl species, respectively.[73,74]

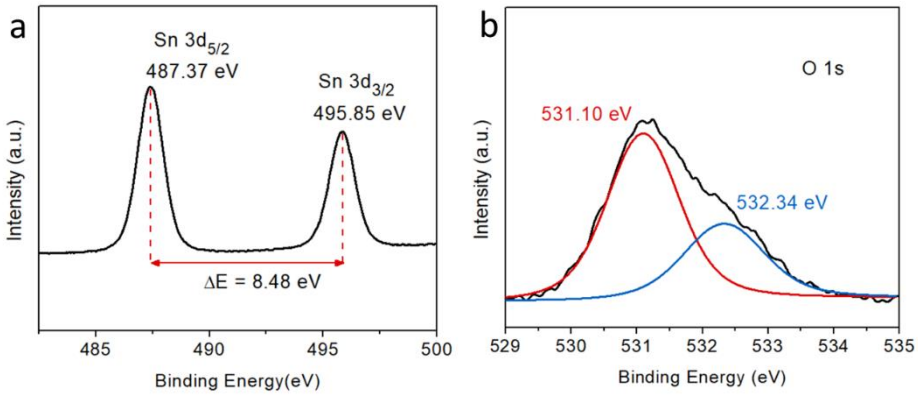

Figure 3.7. XPS profiles of (a) Sn 3d and (b) 1 Os spectra.

The thin-film absorption data was collected and an optical bandgap (E_g^{opt}) of 4.35 eV is estimated from the Tauc plot (Figure 3.8), falling in the reported range from 3.4 to 4.6 eV.[76]

Such a large bandgap and good transmittance to visible and infrared light are promising for low loss of a wide spectrum of incident light through the interlayer.

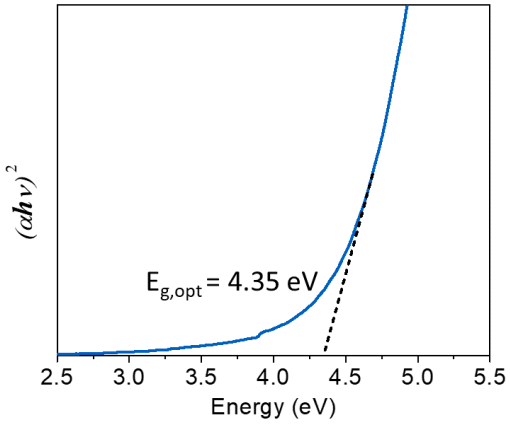

Figure 3.8. Tauc plot derived from the thin-film absorption of tin oxide layer.

Ultraviolet photoelectron spectroscopy (UPS) of the tin oxide film shows a valence region onset at ~3.70 eV (Figure 3.9a), while the secondary electron cutoff is around 16.15 eV (Figure 3.9b). The valence band maximum (VBM) is calculated according to the following equation:

$$VBM = E_{cutoff} - h\nu - E_{onset} \quad (21)$$

where $h\nu$ is the energy of the incident photon from the He (I) source (21.22 eV), E_{cutoff} is secondary electron cutoff edge, and E_{onset} is the valence region onset. The VBM is found to be -8.77 eV *versus* vacuum. Combining the E_g^{opt} of 4.35 eV, the conduction band minimum (CBM) is estimated to be -4.42 eV. Notably, the CBM of SnO_2 has been quoted in a wide range from around -4.0 eV to near -5.0 eV.[77–80] A CBM value of the ETL deeper than the lowest unoccupied molecular orbital (LUMO) level of the active layer is considered energetically beneficial for extraction of photogenerated electrons.[79,81]

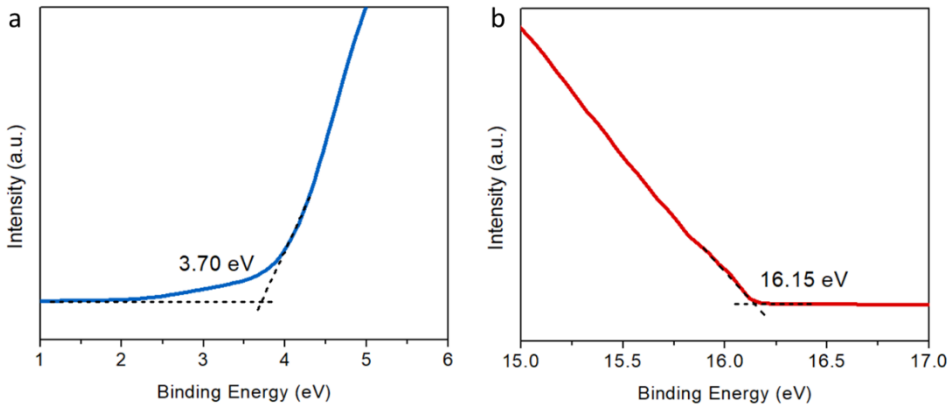

Figure 3.9. UPS profiles of (a) valance region and (a) secondary electron cutoff region of the tin oxide film.

For optimization purpose, tin oxide layer was made as “single”-, “double”- and “triple”-layered films. For the “single” layer one, a one-time spin-coating process was done for the tin oxide layer. Likewise, “double” layer and “triple” layer stand for since a second or a third layer was processed onto the pre-deposited SnO_2 layer in order to obtain a thicker layer. The height profiles of these films by atomic force microscopy (AFM) are shown in Figure 3.10. All of them show surface topology with particulate feature. Their thickness and roughness related statistics are summarized in Table 3.1. While the surface morphology and root-mean-square (rms) of the height profiles are similar for the three, the process of making multilayer tin oxide layer significantly influence the device performance, as will be detailed in the next section.

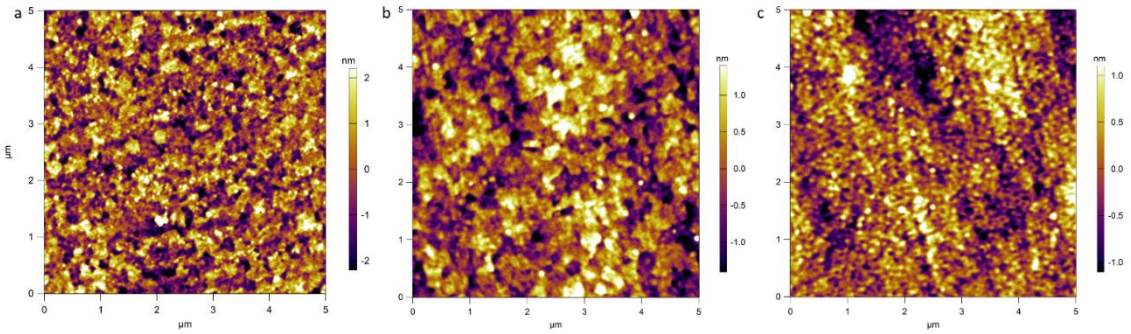

Figure 3.10. AFM images of (a) single, (b) double and (c) triple layer SnO_2 films.

Table 3.1. Thickness and AFM statistics of the SnO_2 films

Sample	Thickness (nm)	Height range (nm)	Height RMS (nm)
Single layer	15	4.40	1.091
Double layer	24	2.80	0.699
Triple layer	34	2.20	0.546

3.5.2 Photodetection Performance

Before discussing the device data, we note that tin oxide has been employed successfully in tackling the illumination-related behaviors in organic solar cells.[82] However, this by no means forecasts readily obtainable success for OPDs, especially considering the four requirements discussed in section 3.4. In the previous works, the target is to prevent the parasitic effects of ZnO from undermining photovoltaic parameters, such as fill factor and PCE. Distinctively here for photodetection applications, the second and fourth aforementioned requirements, respectively revolving around low dark current and fast transient response, highlight the distinct challenge in the present work on OPDs.

The representative *J-V* curves of the OPDs with tin oxide layer as ETL are presented in Figure 3.11a. All three types show very small change between the dark current before and after illumination. While the sought-after illumination-insensitive dark current is obtained, it is noticeable that a large current density was observed for the “single” layer SnO_2-based

device. The device based on “double” and “triple” layer SnO_2 show much smaller dark current density, comparable to the ZnO ETL-based devices before illumination (Figure 3.2) or after UV-filtered illumination (Figure 3.4b). It is also found that the devices with “double” and “triple” layer SnO_2 also feature a smaller variation of the dark current, generally of several nanoamperes per centimeter square, while that of the “single” layer counterparts show a wide range of dark current about 1-4 orders magnitude higher (Figure 3.11b and Figure A3.3).

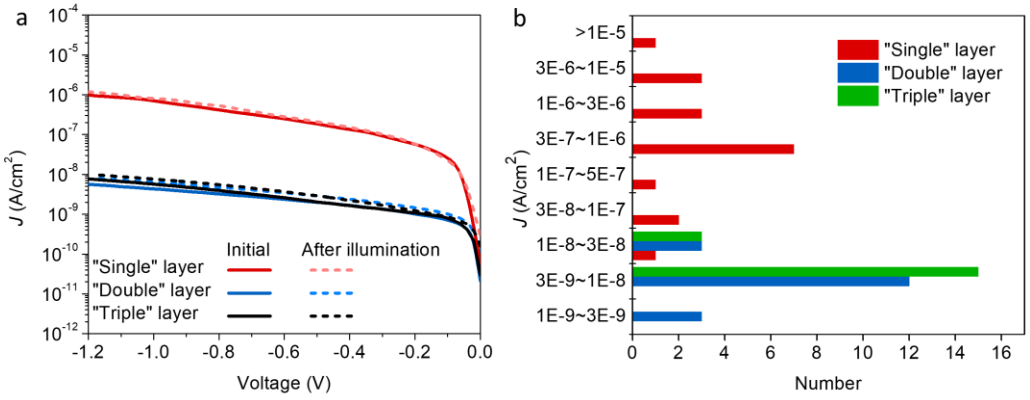

Figure 3.11. (a) Dark *J-V* curves of SnO_2 ETL-based OPDs. (b) Distribution of dark current of SnO_2 ETL-based devices at -1 V.

The better performance of “multilayer” SnO_2 ETL based devices may be a result of lower ratio of surface variation to total film thickness (Figure 3.12 and Table 3.1). As shown by the schematic in Figure 3.12, the ratio of surface height range (SHR) to the film thickness (FT) for the single layer is as large as 0.29, which is much higher than the 0.12 and 0.065 of the other two “multilayer” cases. Having a lower SHR/FT value essentially means a less “sharp” feature at the interfaces between the layers, which prevented the dissolved organic active layer materials from infiltrating into the depth of the ETL during solution processing. In addition, the SHR of the ITO substrate is found to be ~9.9 nm, about 66% of the thickness of the “single” layer SnO_2 film, while being 41% and 29% of the “double” and “triple” layer SnO_2 films, respectively. This also highlights a higher chance of “weak points”, where the active

layer and the highly conductive ITO film can meet or be in close proximity, in the "single" layer case. Notably, the benefit of "multilayer" strategy is more apparent when the configuration goes from "single" to "double", which is reasonable in that the charge selective layer with a small thickness is more susceptible to film defects (e.g., pinholes) and therefore has more chance of hosting shunting pathways considering the non-dense and porous nature of the film according to the AFM profiles.

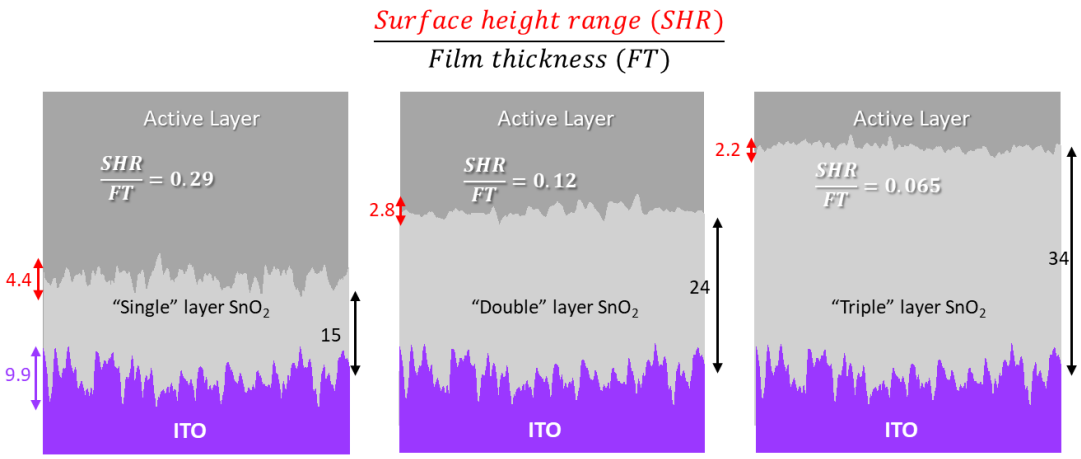

Figure 3.12. Schematic of the beneficial effect of reducing shunting and device-to-device variance by deploying extra layers, leading to a lower SHR/FT value.

Due to the excellent suppression, smaller device-to-device variation of dark current, and balanced production time, the following comparison studies will be mainly referring to the "double" layer one unless otherwise noted. To prevent potential artefacts in the dynamic *J-V* measurements, the steady-state dark current after illumination was also measured under a constant bias of -1 V for about 5 min (Figure 3.13a). A stable and low dark current close to the original level has been found for the SnO_2-based device, in stark contrast to the ZnO counterpart. The reliability of SnO_2-based device is further confirmed by the current response (Figure 3.13b) in additional five consecutive dark-illumination cycles following the 5-min test in Figure 3.13a.

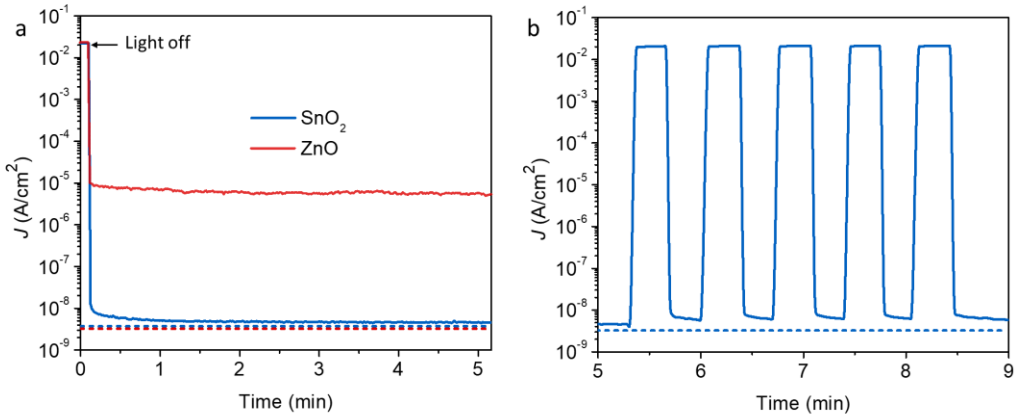

Figure 3.13. (a) Current densities *versus* time for the devices based on ZnO (red) and SnO_2 (blue) ETLs biased at -1 V upon removal of prior 60 sec illumination. Dashed lines indicate the dark current before illumination. (b) Current response of five consecutive dark-illumination cycles following the 5-min test in (a). The dashed line indicates the initial dark current prior to any illumination.

As mentioned in section 3.4, the criteria for the ETL alternative to ZnO not only concern the dark current behavior, but also the photoresponse. Now that the first two requirements, illumination history-insensitivity and low magnitude of the dark current, have been met, we move on to examine the photoresponse of the SnO_2 ETL-based OPDs (Figure 3.14a). For comparison, EQE profiles of the OPDs based on the conventional structure and inverted structure with ZnO ETL are also plotted. The devices based on SnO_2 ETL show EQE spectral shape and values similar to the other two counterparts, with slightly higher EQE values from 550 to 900 nm. The current response to different light intensities (E) of 940 nm light was also recorded for the ZnO or SnO_2 ETL-based devices (Figure A3.4). The photocurrent density (J_{ph}), defined as $J_{ph} = J_L - J_d$, where J_L is the current density under light, is plotted against the light intensity in Figure 3.14b. The photocurrent can usually be considered to bear the following relation with light intensity:

$$J_{ph} \propto E^{\alpha} \tag{22}$$

where α is a fitting parameter. The closer α is to unity, the better the linearity of $J_{ph} - E$ relation and lower the recombination loss. Accordingly, it can be inferred that the SnO_2-based device (α = 0.9996) demonstrates a slightly better linear response than the ZnO-based counterpart (α = 0.9841).

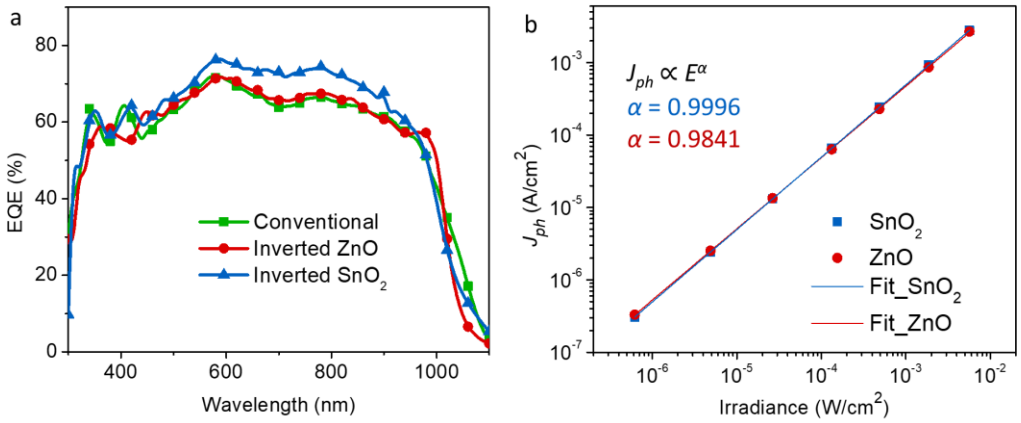

Figure 3.14. (a) EQE profiles and (b) light intensity-dependence of photocurrent density at -1 V.

To evaluate the D^* more accurately, the noise level was also determined from the fast Fourier transform (FFT) of the dark current measured at -1 V (Figure 3.15a). For the "single" layer SnO_2-based device, the noise current spectral density is around 1.48×10^{-13} A $Hz^{-1/2}$, while it is 1.89×10^{-14} A $Hz^{-1/2}$ for the "double" layer SnO_2-based device. For reference, the ZnO-based device was also tested before and after illumination, which delivered noise levels of 1.65×10^{-14} A $Hz^{-1/2}$ and 5.52×10^{-11} A $Hz^{-1/2}$, respectively. The corresponding D^* profiles are derived in Figure 3.15b. As expected, a higher D^* by roughly one order of magnitude is presented for the "double" layer SnO_2-based device compared to the "single" layer counterpart due to the lower dark/noise current. "Double" layer SnO_2-based device, even after illumination, demonstrates similar D^* to that of the ZnO-based counterpart prior to illumination. The peak D^* of 5.82×10^{12} cm·$Hz^{1/2}$·W^{-1} at 900 nm is also among the best of non-photomultiplication OPDs.[27,83,84]

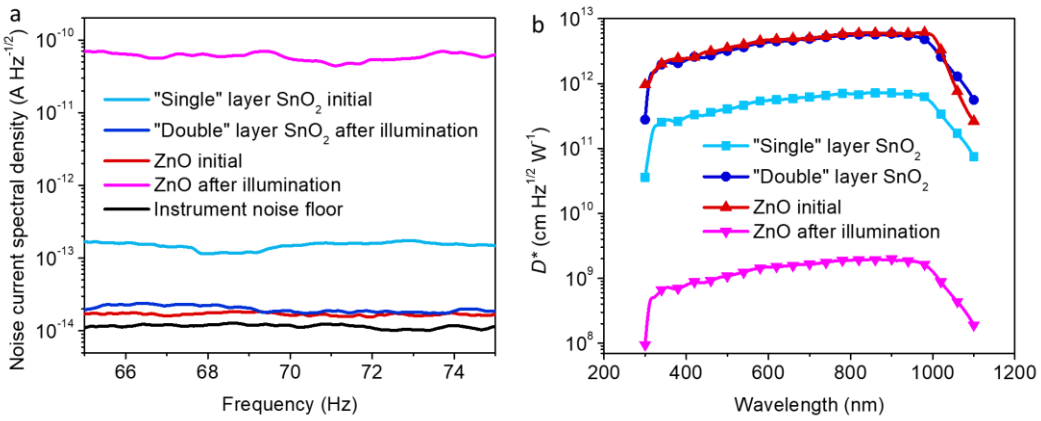

Figure 3.15. (a) Noise current spectral density. (b) *D** profiles at 70 Hz at -1 V.

In addition to the photosensitivity, the transient response was also tested to ensure that the SnO_2 alternative brings no major drawback in detector response speed. The transient response to 940 nm light was recorded for both SnO_2- and ZnO-based devices. In Figure 3.16a, the rise time (t_r), defined as the time which the detector signal takes to go from 10% to 90% of the steady-state photocurrent, was found to be 5.03 μs and 5.77 μs for the ZnO- and SnO_2-based devices, respectively. The 3dB bandwidth (f_{-3dB}), defined as the modulating frequency at which the detector response drops to -3dB (~70%) of the low frequency steady-state level, was estimated from the frequency-dependent photoresponse (Figure 3.16b). It has been found that f_{-3dB} is as close as 95.0 kHz and 108.7 kHz for the two ETLs. These results indicate only a marginally slower response from the SnO_2-based device, which is acceptable considering the overall improvement in figures-of-merit reliability.

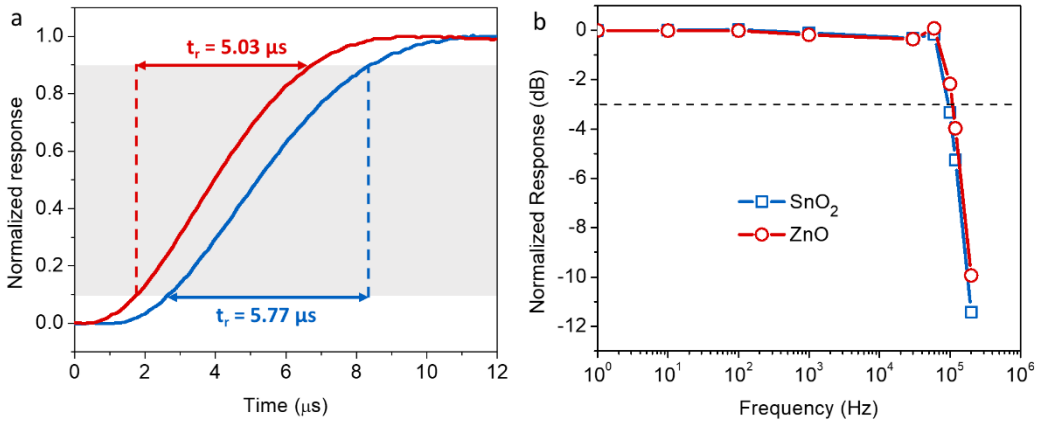

Figure 3.16. (a) Phototransient response and (b) normalized photoresponse as a function of frequency at -1 V.

3.5.3 Applicability in Other BHJ Systems

Preliminary evaluation of its applicability for other BHJ systems was also conducted. Two additional BHJ systems were concerned here. One includes PTB7-Th as the donor and a widely used fullerene acceptor, [6,6]-Phenyl-C71-butyric acid methyl ester ($PC_{70}BM$), as the acceptor. The other BHJ system employs a polymer donor, poly[[4,8-bis[5-(2-ethylhexyl)-4-fluoro-2-thienyl]benzo[1,2-b:4,5-b']dithiophene-2,6-diyl]-2,5-thiophenediyl[5,7-bis(2-ethylhexyl)-4,8-dioxo-4H,8H-benzo[1,2-c:4,5-c']dithiophene-1,3-diyl]-2,5-thiophenediyl] (PM6), and a small-molecule NFA, 2,2'-((2Z,2'Z)-((12,13-bis(2-ethylhexyl)-3,9-diundecyl-12,13-dihydro-[1,2,5]thiadiazolo[3,4-e]thieno[2",3'':4',5']thieno[2',3':4,5]pyrrolo[3,2-g]thieno[2',3':4,5]thieno[3,2-b]indole-2,10-diyl)bis(methanylylidene))bis(5,6-difluoro-3-oxo-2,3-dihydro-1H-indene-2,1-diylidene))dimalononitrile (Y6).[85] The data for the dark current and EQE characteristics of these two BHJ systems are shown in Figure A3.5 and Figure A3.6, respectively. Similar illumination history-sensitive dark current in the ZnO-based devices for both BHJ systems of PTB7-Th:$PC_{70}BM$ (Figure A3.5b) and PM6:Y6 (Figure A3.6b) have been noticed, which is in clear contrast with the small changes shown by

the SnO_2 ETL-based devices (Figure A3.5c and Figure A3.6c). In addition, the SnO_2 ETL-based devices also demonstrate similar (Figure A3.5d) or better (Figure A3.6d) photoresponse compared to the ZnO ETL-based devices. The preliminary results feature a promising sign that the proposed alternative may be applicable in other material systems.

3.6 Difference between SnO_2 and ZnO as Electron Transport Layer

To understand why the SnO_2 -based and ZnO -based devices show such contrast to the UV illumination history, some additional investigations are done. It has been reported that ZnO can exhibit higher conductivity than its initial state on a timescale up to hours after UV exposure, which was termed as "persistent photoconductivity".[86] To find out whether this so-called "persistent photoconductivity" is the direct cause of the increased dark current in the OPDs, vertical diode devices with the configuration of ITO/ETL/Ag were made (Figure 3.17a), and their *J-V* characteristics before and after illumination were collected (Figure 3.18b).

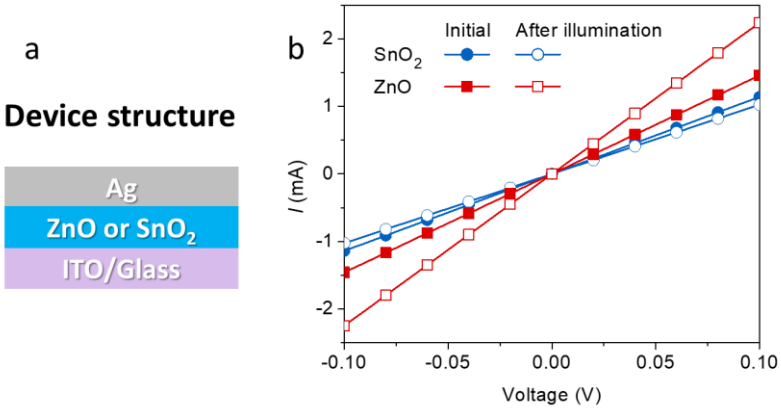

Figure 3.17. (a) Device structure and (b) dark *J-V* characteristics before and after illumination of ITO/ETL/Ag devices.

Both types of devices show symmetric linear *J-V* behavior, evidencing good ohmic contacts between the electrodes and the ETL films. Correcting the resistance (17.9 Ω) from the ITO

and Ag electrodes, the initial resistance of ZnO and SnO_2 films is 50.6 Ω and 69.8 Ω, respectively, which changes to 26.6 Ω and 79.6 Ω after illumination, respectively. While the resistance for both metal oxide films changes to a degree, such small values contribute very little to the total resistance of the full stack of layers in the OPDs, where the differential resistance lies in the range of 10^6-10^{10} Ω (Figure A3.7) even after illumination. Thus, the different behaviors of dark current to illumination history may not be directly linked to the variance in bulk conductivity of the ETLs or the ETL/ITO interfaces. This conclusion is further evidenced with nanoscale characterization by conductive-atomic force microscopy (c-AFM) in Figure A3.8. The relatively small difference (<100%) between the nanoscale dark current before and after illumination for the ZnO film does not agree with the large change by several orders of magnitude shown in the full ZnO-based OPDs.

To further pinpoint the origin of the different behaviors for the OPDs based on the two ETLs, devices with only PTB7-Th polymer in the active layer were made. Due to lack of the acceptor CO1-4Cl, a large mismatch exists between the LUMO level (-3.61 eV) of active layer and the large work function of (~6.9 eV) of MoO_3.[87] Therefore, negligible electron injection from the Ag/MoO_3 electrode to the organic layer is expected when the ITO side is positively biased. As a result, the measured dark current can be mainly ascribed to the hole transport from the ITO/ZnO electrode, through the organic active layer, to the top MoO_x/Ag electrode (inset of Figure 3.18). The dark *J-V* characteristics in Figure 3.18 have the voltage on the ITO side being referred to. For the fresh devices based on both ETLs, the dark current density is very similar, being slightly lower than 1 nA/cm^2 at 1 V. After illumination, the *J-V* curve of the SnO_2-based one does not show significant change, with only 32.6% increase at 1 V. On

the contrary, the dark current for ZnO-based counterpart shows considerable increase (~139000% at 1 V) similar to what was found in the full OPD devices (Figure 3.2).

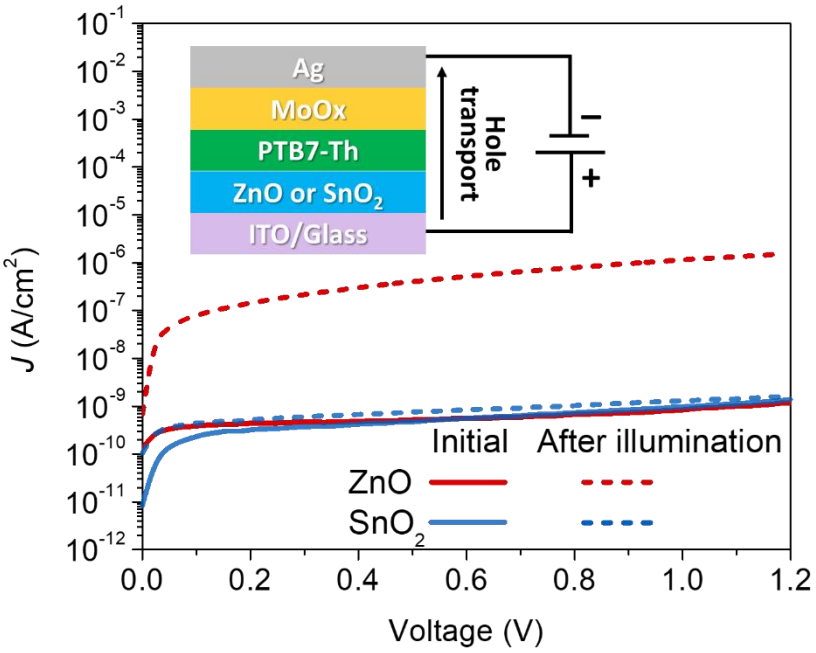

Figure 3.18. Dark *J-V* characteristics before and after illumination of the donor-only devices containing only PTB7-Th as the active layer. The inset shows the structure and operation of the devices.

From these comparisons, we can narrow down the cause behind the observed increase of dark current in the OPDs to be the greatly enhanced the hole transport. ZnO ETLs have been shown to undergo characteristic photo-induced shunting as a result of desorption of surface oxygen under UV light, which weakens its charge transport selectivity and hole blocking function.[72,88,89] In certain extreme cases, the ZnO/organic junction can even become quasi-ohmic, leading to unimpeded hole transport and symmetric dark *J-V* characteristics.[63]

3.7 Other Attempts

Prior to the success of the use of tin oxide layer as the alternative ETL, we have screened some materials including some organic ETLs commonly used in the literature for organic

photodiodes, as well as modification of ZnO with some organic ETLs. For example, a small molecule of perylene diimide functionalized with amino N-oxide (PDINO) and a polymer of polyethylenimine ethoxylated (PEIE) (Figure 3.19a) were tested. The dark *J-V* curves of the devices based on these alternative ETLs show minimal sensitivity to illumination for the dark current (Figure 3.19b). However, the magnitude of the dark current (around 10^{-7} A/cm^2 at -1 V) is about one order of magnitude higher than the before-illumination ZnO counterpart. Hence, they were not further considered in the scope of this work per the second requirement discussed in the section 3.4.

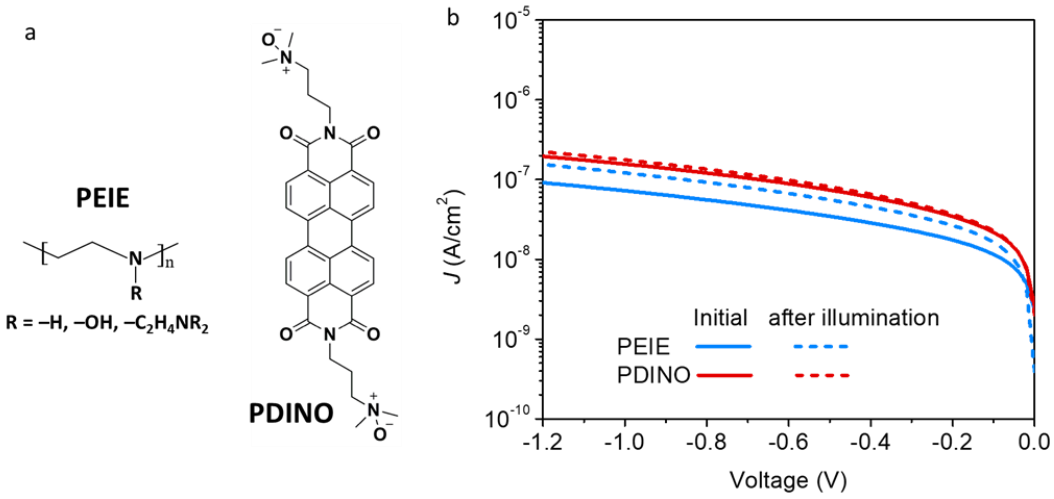

Figure 3.19. (a) Chemical structures of PEIE and PDINO. (b) Dark *J-V* characteristics of the inverted OPD devices based on "double" layer PEIE (blue) and PDINO (red) ETLs.

In terms of the route of modifying the ZnO, bathocuproine (BCP), poly [(9,9-bis(3'-(N,N-dimethylamino)propyl)-2,7-fluorene)-alt-2,7-(9,9–dioctylfluorene)] (PFN), Poly(9,9-bis(3'-(N,N-dimethyl)-N-ethylammoinium-propyl-2,7-fluorene)-alt-2,7-(9,9-dioctylfluorene))dibromide (PFN-Br), and PDINO were used (Figure 3.20a), which were all deposited on the ZnO layer before the coating of the active layer. In Figure 3.20b, it is shown that, when using these organic ETLs to modify the surface ZnO layer, while the initial dark current was found to be acceptably low compared to that of the pristine ZnO, the problem of

after-illumination increase in dark current persists to different degrees. Hence, this route is also proved not effective per the first requirement mentioned in the section 3.4.

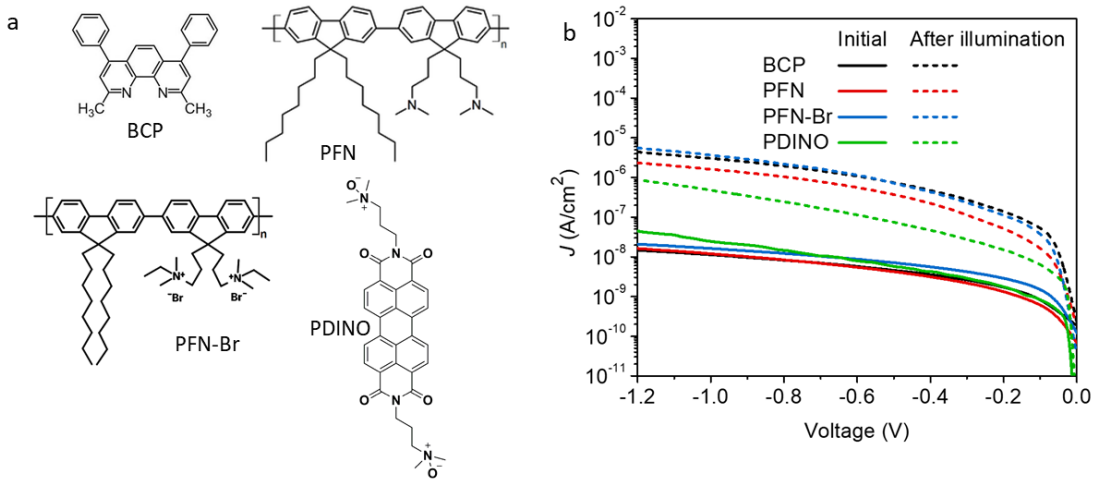

Figure 3.20. Chemical structures of PEIE and PDINO. (b) Initial and after-illumination dark *J-V* characteristics of the inverted devices with different interlayers between the ZnO ETL and active layer.

3.8 Experimental

3.8.1 Device fabrication

The default precursor solution of ZnO through this Chapter, unless otherwise noted, was prepared by mixing diethylzinc solution and tetrahydrofuran (THF) with a volume ratio of 1:2. Precursor solution for ZnO prepared via the zinc acetate-based sol-gel approach was prepared by mixing 100 mg zinc acetate dihydrate and 28 mg ethanolamine in 1 mL 2-methoxyethanol. The precursor solution of SnO_2 was prepared by dissolving $SnCl_2 \cdot 2H_2O$ in absolute ethanol to give a clear solution with concentration of 0.1 M, which was left to age overnight before use. Cleaned indium-doped tin oxide (ITO) substrates were subject to UV-ozone treatment for 15 min before solution processing. For the ZnO-based inverted devices, the precursor solution of ZnO was spun at 4000 rpm onto the ITO substrates and annealed at

110 °C for 15 min. Zinc acetate sol-gel solution was spun at 4000 rpm, followed by annealing at 200 °C for one hour. The commercial ZnO NPs suspension was spun at 3000 rpm and annealed at 110 °C for 15 min. For the "single" layer SnO_2 -based inverted devices, the precursor solution was spun at 2500 rpm and annealed at 180 °C for 30 min. For the "double" layer SnO_2-based devices, the second layer was spin-coated after the first layer had been annealed and cooled down, where a spin speed of 3500 rpm was used for the two coating processes. For deposition of the different BHJ active layers, the substrates with the ETLs were transferred to a N_2-filled glovebox. PBT7-Th:CO1-4Cl (1:1.5 weight ratio, 35 mg/mL) chlorobenzene solution (with 2 v% 1-chloronaphthalene) was spun at 1000 rpm. PM6:Y6 (1:1.2 weight ratio, 16 mg/mL) chloroform solution was spun at 2000 rpm. PTB7-Th:$PC_{70}BM$ (1:1 weight ratio, 35 mg/mL) chlorobenzene solution (with 3 v% 1,8-diiodooctane) was spun at 2000 rpm, followed by a brief methanol rinse. The procedures for depositing the active layers were the same for the conventional structure devices. Prior to active layer deposition, PEDOT:PSS solution was spun onto the ITO substrates at 2500 rpm and annealed at 125 °C for 30 min. After deposition of the active layer, Al cathode (100 nm) or MoO_3 (6 nm)/Ag (100 nm) anode was evaporated under vacuum (~10^{-7} torr) on the active layer for the conventional or inverted devices, respectively.

3.8.2 Spectroscopic Analysis

X-ray photoelectron spectroscopy. Data were obtained using a ThermoFischer EscaLab Xi+ system emitting X-rays from a monochromated Al source. A pass energy of 20 eV was used for all high-resolution element sweeps. Measurements were taken at a base analytical chamber pressure of 10^{-9} Torr. Peak fitting was performed using CasaXPS, and atomic sensitivity factors were taken into account during peak integrations.

Ultraviolet photoelectron spectroscopy. Data were obtained using a ThermoFischer EscaLab Xi+ system with the ultraviolet emission set to the He 1α line (21.22 eV). Measurements were taken at a base analytical chamber pressure of 10^{-8} Torr.

UV-Vis spectroscopy. The thin film absorption of the SnO_2 film was taken from on a LAMBDA 750 UV/Vis/NIR spectrophotometer (Perkin Elmer). The films were prepared similarly as in OPD preparation except that UV ozone-treated quartz substrate was used.

3.8.3 Conductive atomic force microscopy

The measurements were obtained from an Asylum MFP-3D atomic force microscope atop an inverted optical microscope (Olympus, IX71), under an inert atmosphere. Electrically conductive Pt/Cr-coated silicon probes with a resonant frequency of ~13 kHz and a spring constant of ~0.2 N m^{-1} (Budget Sensors) were used. A 160 μm diameter white light spot, with a power of 30 W cm^{-2}, was provided with an arc lamp (Newport, Model 67005) and focused on the sample through the inverted optical microscope (Olympus). The conductive tip was positioned at the center of the light spot, and an internal preamplifier (Asylum Research ORCA head model) was used to record the photocurrent. The morphology images were processed using first-order image flattening and all images were analyzed on Asylum Research AFM software version 14, programmed using IGOR Pro.

3.8.4 Device Characterizations

The *J-V* and current-time characteristics were measured with a Keithley 4200 semiconductor characterization system. The EQE was measured with a 75-Watt monochromatic light source and a chopper modulating the optical frequency at 70 Hz. The signal was amplified with an SRS 570 pre-amplifier and recorded with an SR810 DSP lock-

in amplifier. A silicon photodiode (Newport 818-UV) was used for as a reference for calibration. For both phototransient response measurements and noise signal measurement, the devices under test were connected to an SRS 570 pre-amplifier in low noise mode, which also applied the DC bias on the devices. The signal was then fed to a Keysight 200 MHz oscilloscope (Model DSOX3022T) configured under high resolution acquisition mode. In phototransient test, the light source was a set of 940 nm LEDs powered by square-wave voltage from an AC function generator (SRS DS345) and providing light intensity about 1.96 mW/cm^2. The noise measurement was conducted in the dark with the oscilloscope operating with a built-in FFT analysis program.

Chapter 4

Large-Gain Low-Voltage and Wideband Photomultiplication Organic Photodetectors via Unbalanced Charge Transport

4.1 Introduction

High-sensitivity photodetectors are widely relevant in optoelectronics, leading to considerable efforts in both fundamental study and applied research.[29,90] Thanks to the progress in materials design, device engineering and understanding of photophysics, photodetectors based on organic semiconductors are emerging as a promising candidate with favorable cost-effectiveness, large-scale processability, mechanical conformability and flexible tunability.[56,91,92] Widely applied in organic photovoltaics, the rectifying diode architecture is also heavily employed for constructing organic photodetectors (OPDs). However, the theoretical external quantum efficiency (EQE) of these non-photomultiplication (PM) OPDs cannot exceed 100%, leading to small outputs when detecting weak signals. This places high demands on external amplification circuitries for practical applications.[93] Alternatively, certain gain mechanisms can be introduced to construct PM OPDs. Due to the large exciton dissociation energies of disordered organic semiconductors, the established gain mechanisms for inorganic photodetectors, such as ionization impact where one photogenerated charge carrier can induce multiple free charge carriers under large electric field, cannot be readily applied.[94] Instead, other strategies have been explored. For example, by co-depositing inorganic nanoparticles with conjugated polymers, hybrid organic–inorganic photodetectors were demonstrated by Yang and Huang, showing EQE from 10^3% to over 10^5% in the UV and visible spectra.[31,94] The gain mechanism was explained as trap-assisted

charge injection. Following this concept, PM OPDs were realized using disproportionate donor–acceptor (D–A) ratios,[95–98] dopant dyes,[99] or by confinement of carriers with extraction barriers.[100] These efforts have led to PM OPDs that compete favorably with avalanche gain inorganic detectors. However, PM OPDs still face several major challenges. First, their spectral response is limited by poor photon harvesting, and there is insignificant spectral response beyond visible spectra. Efforts have been made to extend the spectral response by incorporating near infrared (NIR) absorbing dyes,[99] conjugated polymers with a narrower bandgap,[95] inorganic quantum dots,[101] or an additional layer with broader spectral absorbance.[102] However, these strategies compromise the photoresponse, leading to lower EQE values achievable without the later introduced spectrum-widening components. Another obstacle is the slow response times from tens of milliseconds to over a second,[93,103] unfavorable for operations involving real-time interactions such as health monitoring. Finally, the voltage required to achieve high photoresponse is still large. The threshold voltage required to achieve over 100% of EQE varies from a few volts to over 10 V, and that for achieving EQE of 10^4% can be as large as 20 V,[96,98,104,105] which are energy-inefficient and undesirable for the use of OPDs in wearable/portable electronics.

While previous efforts usually show improvement on one of the issues, efforts are scarcely demonstrated to address the composite set of challenges toward comprehensively well performing candidates. Herein, we demonstrate a step toward such all-rounder gain OPDs, that simultaneously achieve EQE over 10^4%, wide spectral response cutting off around 1200 nm, real-time monitoring applicable response speed, low gain-threshold voltage of several millivolts, and low operating voltages no larger than that of an AA battery (1.5 V). A systematic study reveals a trap-enhanced photoconductive gain mechanism.[106] The strategy in

this work is also applicable to different organic bulk heterojunction (BHJ) systems, making it a promising approach for further exploration with the large diversity of available organic photoactive materials.

4.2 Photoresponse Performance

To gain a wide spectral response from UV to NIR, a bulk heterojunction blend of poly[(4,8-bis(5-(2-ethylhexyl)thiophen-2-yl)benzo[1,2-b;4,5-b0]dithiophene-2,6-diyl-alt-(4-(2-ethylhexyl)-3-fluorothieno[3,4-b]thiophene-)-2-carboxylate-2-6-diyl)] (PTB7-Th) and COTIC-4F were chosen as the active layer for its broadband absorption.[9,10] Different amount of tetracyanoquinodimethane (TCNQ) was added to this donor-acceptor blend. The chemical structures and the energy levels of these materials are shown in Figure 4.1. The photodetector devices use a vertical structure (Figure 4.1c), where the active layer is sandwiched between a layer of poly(3,4-ethylenedioxythiophene) polystyrene sulfonate (PEDOT:PSS) deposited on the indium-doped tin oxide substrate and a thermally evaporated Al film on the top.

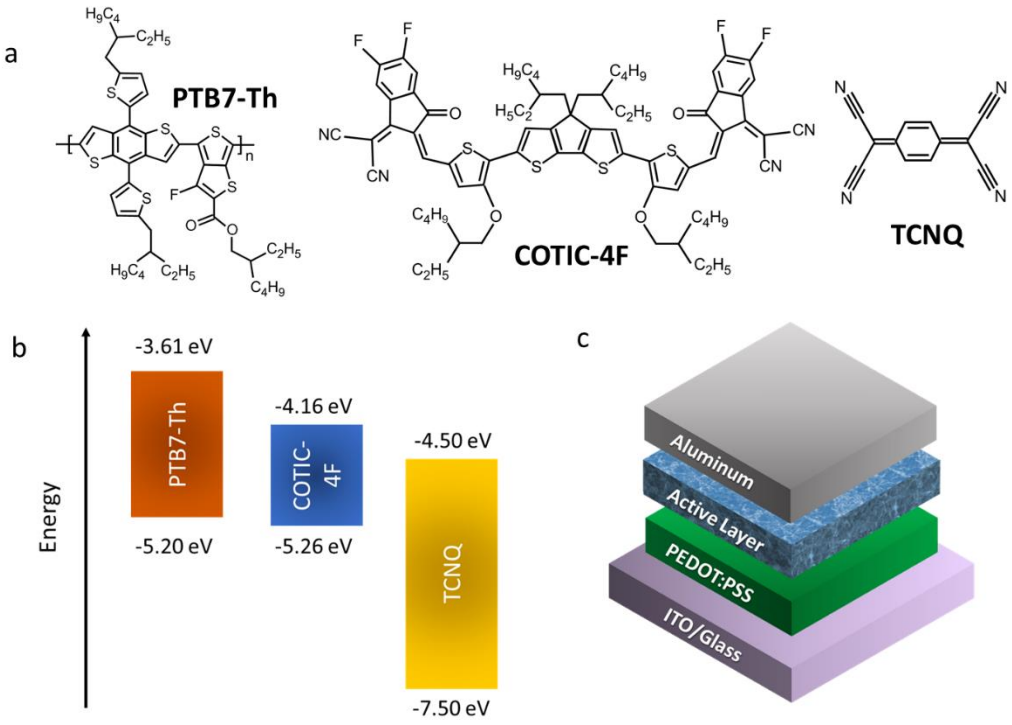

Figure 4.1. (a) Chemical structures and (b) energy levels of PTB7-Th, COTIC-4F and TCNQ. (c) Device structure of the photodetectors.

For simplicity, we refer to the devices with the active layer of PTB7-Th:COTIC-4F:TCNQ as PC-Tx, where "x" represents the weight percentage (wt%) of the TCNQ relative to the total weight of PTB7-Th and COTIC-4F. Due to the solubility limit of TCNQ in the processing solvent chlorobenzene, the largest x value in this work is 1.55. We can find that for the PC-T0 device (Figure 4.2a), the EQE increases with the bias, showcasing a typical electric field-enhanced extraction of the photogenerated carriers. However, due to the inevitable loss in photon capturing, carrier recombination, and the absence of multi-carrier generation processes observable in crystalline inorganic semiconductors,[107,108] the EQE is lower than 100% regardless of the bias applied to improve the carrier collection. When TCNQ is introduced for the PC-T0.1, PC-T0.3, PC-T1, and PC-T1.55 devices (Figure 4.2b to 4.2e), while a similar span of spectral response is observed, the EQE is considerably enhanced. The effect of the

quantity of the TCNQ on the EQE is summarized in Figure 4.2f for all the devices, where an optimized quantity is determined to be 1% TCNQ. The PC-T1 device can reach over 20000% EQE at a small bias of -1.5 V (Figure 4.2d). Additionally, a small gain-threshold voltage of only -5 mV is required for the EQE to surpass 100%. In terms of the relation between the quantity of TCNQ and EQE, one interesting observation is that the devices with larger EQE under bias will show lower EQE under short-circuit condition (0 V). From low values to high for EQE, the order is PC-T0, PC-T0.1, PC-T0.3, PC-T1.55 and PC-T1 under the biased condition, while the trend for the short-circuit condition is the opposite. The undermined EQE under short-circuit condition can be well rationalized by the trap states induced by the TCNQ molecules for the photogenerated electrons with its deep lying lowest unoccupied molecular orbital (LUMO) level below those of the BHJ components. These trap states can act as carrier recombination centers, decreasing the number of extractable photogenerated carriers.[109] For the case of saturated TCNQ (PC-T1.55), the EQE is slightly higher than PC-T1, possibly due to the higher tendency to aggregation of TCNQ and therefore some degree of alleviation of its charge trapping. On the other hand, when a bias is applied, the opposite trend of EQE observed for these PC-Tx devices heavily implies that the PM gain effect in the devices with TCNQ does not stem from the typical field-enhanced charge collection as in PC-T0. Additionally, while the EQE obtained from the PC-T0.1 device is overall below 100%, the close-to-unity EQE of 98.1% compared to 55.8% of the PC-T0 device under the same bias (-10 V) still implies the presence of the PM gain effect in the PC-T0.1 device considering the losses from the photon absorption and charge recombination.

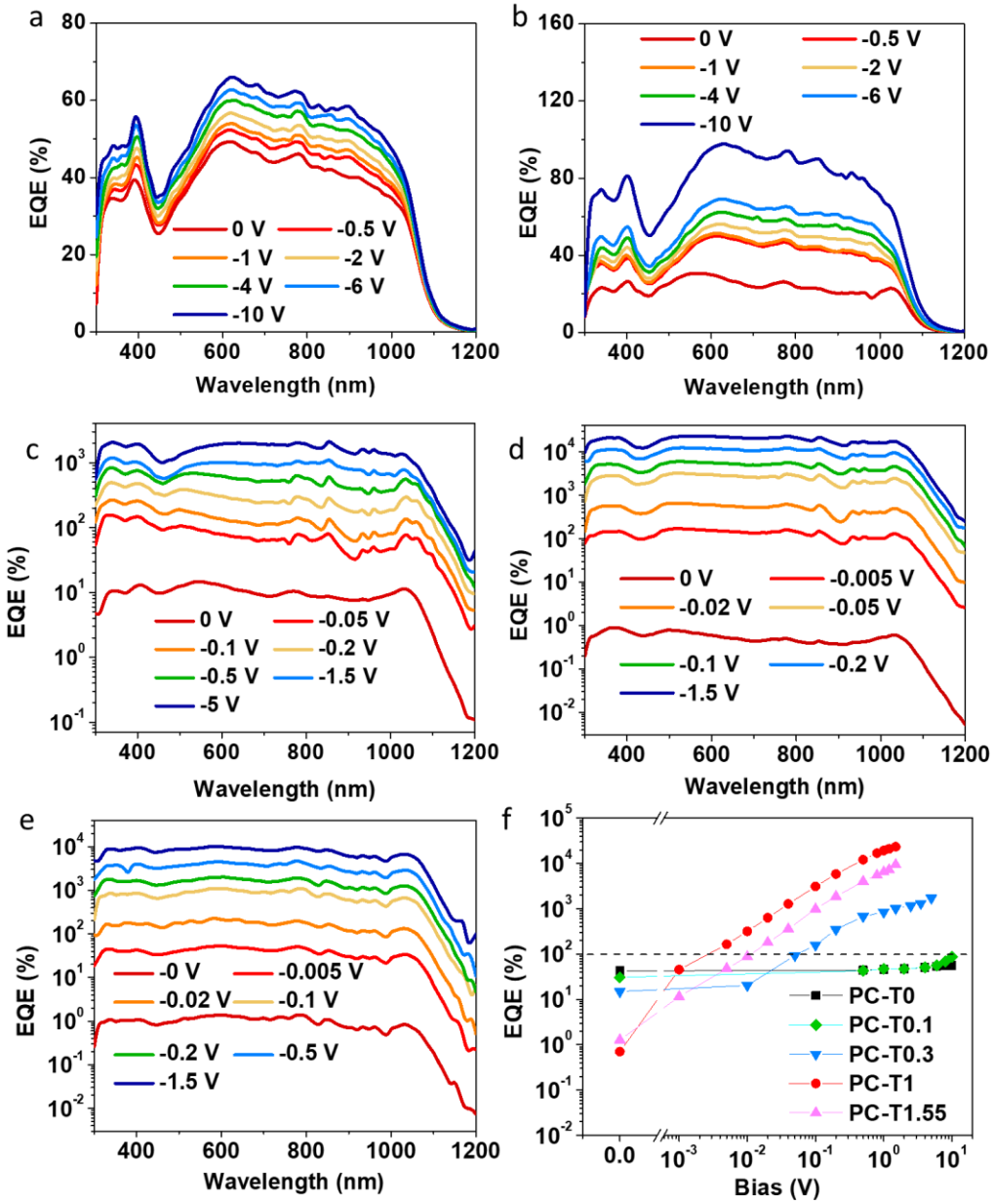

Figure 4.2. EQE spectral profiles of (a) PC-T0, (b) PC-T0.1, (c) PC-T0.3, (d) PC-T1 and (e) PC-T1.55. (f) EQE at 550 nm as a function of the applied bias for these devices.

4.3 Origin of the PM Effect

Apparently, the PM effect is related to the added TCNQ in the D-A blend. When compared to previously reported PM OPDs based on trap-assisted band bending mechanism, there exists such similarity where disproportionate ratios of the components in the active layer can be

found.[31,98] However, the much smaller gain-threshold voltage and the opposite trend of EQE as a function of the quantity of the trap-inducing materials suggest a different origin of the gian effect. To obtain more insights into the underlying dynamics, we sought to understand the effect of incorporating TCNQ on the charge transport properties of the devices. The focus is placed on the gain-absent PC-T0 and the highest gain PC-T1 devices.

4.3.1 Effect of TCNQ on the Interfacial Conditions

First, we assumed if the TCNQ-involved effect responsible for the observed gain occurs only in the bulk of the active layer, then changing the conditions at the interface between the active layer and electrode should not significantly alter the photoresponse behavior of the devices. Hence, modified PC-T1 devices were prepared, which feature a layer of Al-doped ZnO between the active layer and the Al top electrode (Figure 4.3a). Surprisingly, the 100%-EQE-breaking gain behavior is not seen within a reasonable range of bias (Figure 4.3b), and the achieved EQE at -10 V is very close to that of the PC-T0 devices. This indicates that the assumption is not true, and a direct contact between the Al electrode and the TCNQ added to the active layer (called as interfacial TCNQ in this work) is prerequisite for the gain effect to occur. During the device fabrication, the Al was evaporated onto the active layer to form a capping electrode. It is believed that some portion of the TCNQ at and/or close to the surface of the active layer will interact with the incoming Al vapor, which is being deposited on the surface of the active layer and may diffuse into the active layer to a degree.

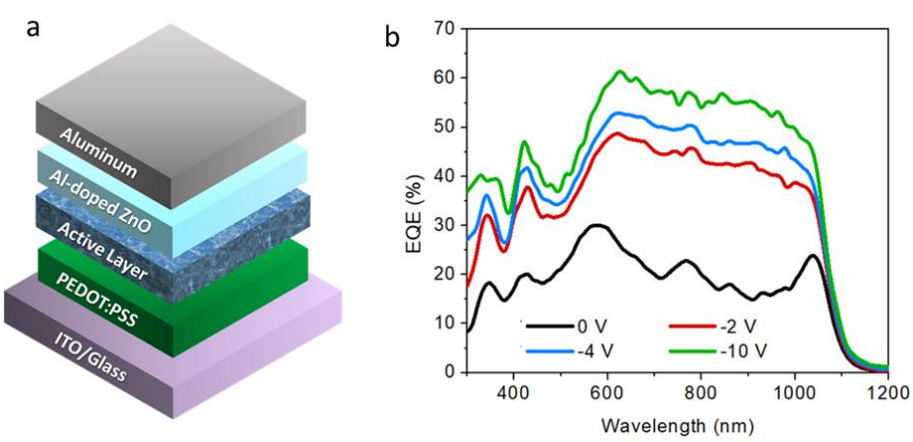

Figure 4.3. (a) Device structure and (b) typical EQE spectrum of modified PC-T1 device where a solution-processed aluminum-doped zinc oxide nanoparticle layer is between the active layer and the top electrode.

To understand the potential interaction between the evaporated Al and the interfacial TCNQ, spectroscopic study on an simplified scenario is conducted, where the Al is evaporated with TCNQ powder near the evaporation source (Figure 4.4a). The Fourier-transform infrared (FT-IR) spectrum (Figure 4.4b) of the Al vapor-treated TCNQ sample is plotted against the spectrum from the pristine TCNQ powder. The C≡N and C=C peaks typical of the reduced form of TCNQ species are identified for the Al vapor-treated TCNQ sample at 2177 cm^{-1} and 1505 cm^{-1}, respectively. For the pristine TCNQ sample, the corresponding characteristic signals are found at 2222 cm^{-1} (C≡N) and 1542 cm^{-1} (C=C) for neutral $TCNQ^0$. Such shifts suggest electron transfer from Al to TCNQ and formation of Al-TCNQ complexes during evaporation of the Al electrode atop the TCNQ-containing active layer.[110] Such metal-TCNQ complex have been found to increase the work function of the metal electrode and lower the contact resistance for hole injection.[111,112] Therefore, we subsequently explored the change in the charge injection at the organic/metal interface by extracting the contact resistance (R_{ct}) using the transmission line method (TLM). The relevant data are shown in the Appendices (Figure A4.1). The calculated width-normalized contact resistanct ($R_{ct} \cdot W$) is 3.63×10^8 and

1.12×10^7 Ω·mm for the p-type operation (corresponding to the hole transport) of the field-effect transistors based on PC-T0 and PC-T1 active layers, respectively. This dramatic decrease of the $R_{ct}\cdot W$ by more than one order of magnitude has confirmed the facilitated hole injection at the Al metal-organic interface when TCNQ is present.

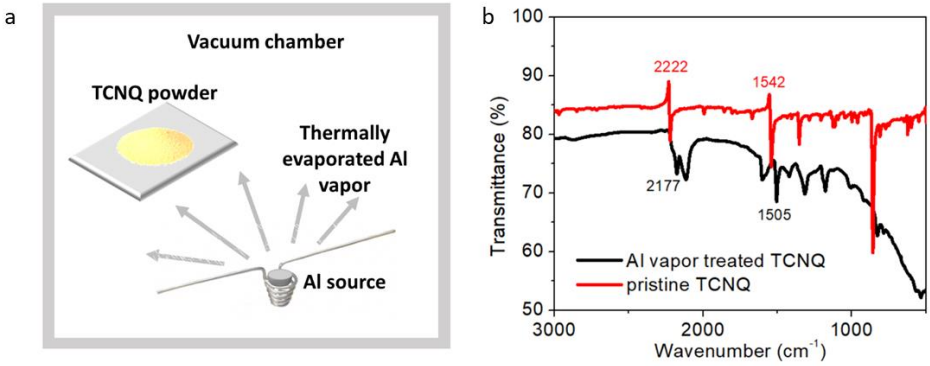

Figure 4.4. (a) Schematic of preparation of Al vapor treated TCNQ sample. (b) FTIR spectra of pristine TCNQ and Al vapor treated TCNQ samples.

To confirm that the change of the contact property is owing to the work function, the difference of the work function of the pristine and TCNQ-treated Al films was obtained by scanning Kelvin probe microscopy (SKPM). The contact potential difference (CPD) is defined as:

$$e \cdot CPD = \Phi_{tip} - \Phi_{sample} \tag{23}$$

where e is the elementary charge, Φ_{tip} and Φ_{sample} are the work function of the measuring tip and the sample, respectively.

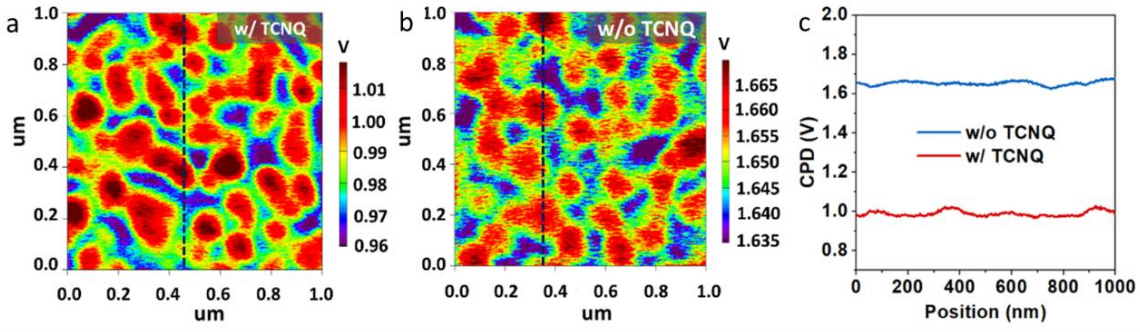

Figure 4.5. CPD images of the Al film (a) with and (b) without modification of TCNQ. (c) Line profiles of CPD for the samples in (a) at and (b).

The CPD profiles for the two types of Al films are shown in Figure 4.5a and 4.5b. Line-scan profiles of the two samples (Figure 4.5c) reveal that the CPD of the pristine Al film (CPD_{Al}) is 1.652±0.014 V, and that of the TCNQ-modified Al film ($CPD_{Al\text{-}TCNQ}$) is 0.988±0.010 V. Therefore, the change in work function upon modification of Al with TCNQ is about +0.664 eV according to the equation:

$$\Delta\Phi = \Phi_{Al-TCNQ} - \Phi_{Al} = e \cdot \left(CPD_{Al} - CPD_{Al-TCNQ}\right) \quad (24)$$

where $\Phi_{Al\text{-}TCNQ}$ and Φ_{Al} are the work function of the TCNQ-modified and pristine Al films, respectively. Thus, the increase in work function upon modification of TCNQ is expected to lead to improved hole transport at the organic/metal interfaces. This agrees well with the trend of the *J*-*V* characteristics (Figure 4.6) in the dark for all the PC-T*x* devices.

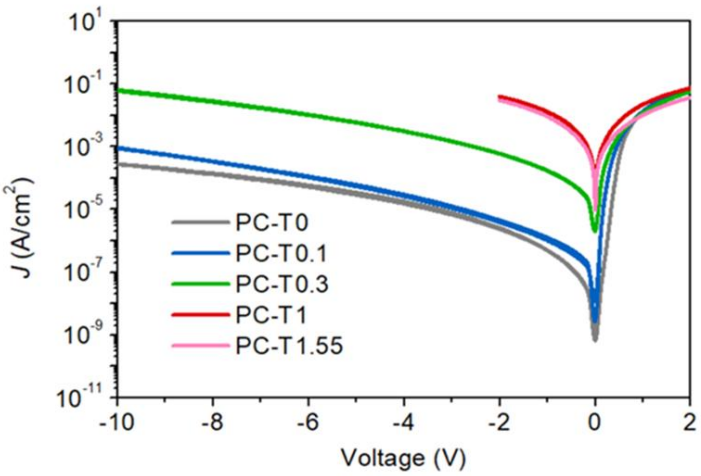

Figure 4.6. (a) *J-V* characteristics in the dark of the PC-T*x* devices.

As a result of increase in work function of the Al top electrode and improved hole injection, the dark current increases with the amount of the TCNQ. In addition, a gradual loss of typical diode rectification behavior is observed with more TCNQ in presence, indicating a Schottky-to-ohmic conversion of the metal/organic interface.

4.3.2 Effect of TCNQ on Charge Transport of the Active Layer

After revealing the effect of the interfacial TCNQ, we further sought to understand the impact of the TCNQ in the bulk of the active layer (called bulk TCNQ in this work). Modified PC-T0 devices were prepared, with the top Al electrode replaced with large work function MoO_x/Ag electrode (Figure 4.7a). The large work function of the MoO_x/Ag will enable efficient hole injection similar to the case of PC-T1 device. This type of devices are abbreviated as H-PC-T0 to present their dominant hole transport due to the charge selective electrodes, yet without TCNQ added to the active layer. Figure 4.7b shows that H-PC-T0 device exhbiting EQE larger than 100%, which is, however, lower than that of the PC-T1 counterpart under the same voltages. This contrast implies that although the bulk TCNQ is not a precondition which determines whether the 100%-EQE-breaking PM effect will be

present, its existence undoubtedly contributes to a stronger larger photocurrent gain and higher EQE.

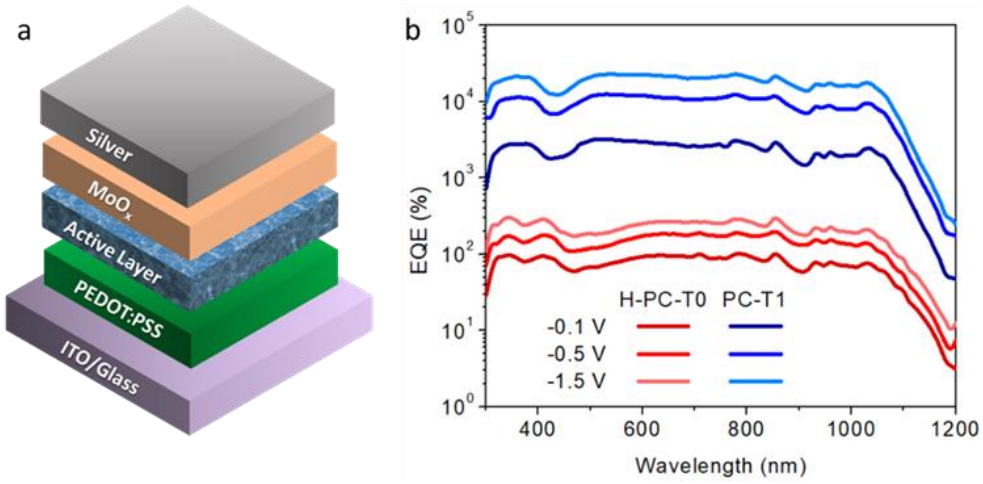

Figure 4.7. (a) Device structure and (b) spectral EQE of H-PC-T0 device with MoO_x/Ag as the top electrode compared with PC-T1 device.

To find the effect of the bulk TCNQ on the charge transport of the active layer, single-carrier diodes with the active layers of PC-T0 and PC-T1 were made to extract the electron and hole mobilities (Figure 4.8). The hole and electron mobilities of PC-T0 devices were found to be $(2.12\pm0.32)\times10^{-4}$ and $(1.27\pm0.23)\times10^{-4}$ cm^2 $V^{-1}s^{-1}$. For PC-T1, the values were $(2.86\pm0.73)\times10^{-4}$ and $(1.93\pm1.61)\times10^{-6}$ cm^2 $V^{-1}s^{-1}$ for hole and electron, respectively.

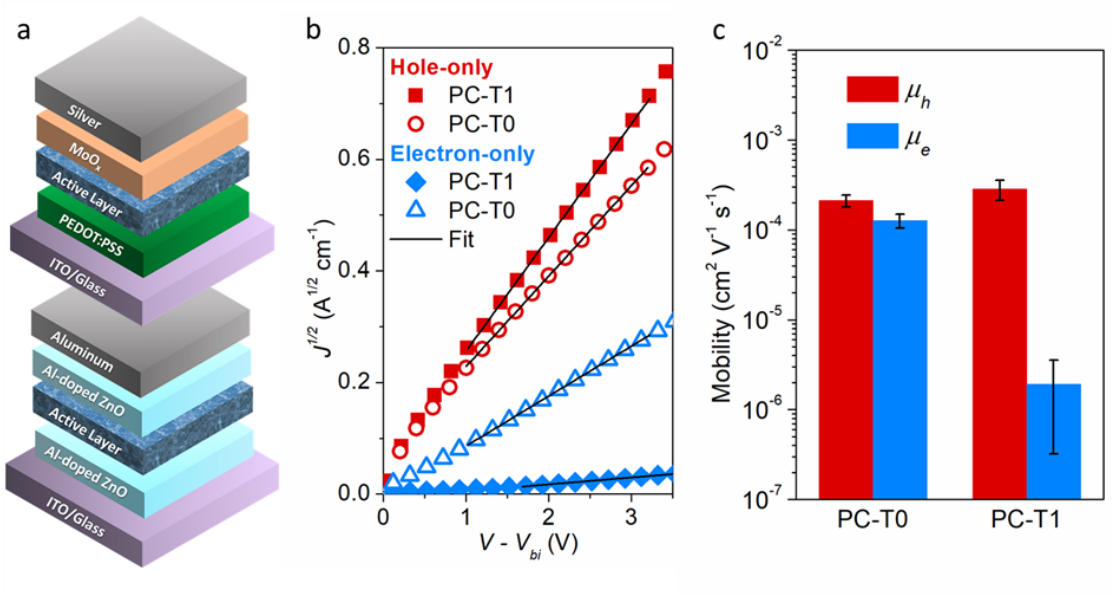

Figure 4.8. (a) Device structure of the hole-only (upper) and electron-only (lower) diodes. Specifically, for electron-only diode, the active layer is sandwiched between Al-doped ZnO layers to prevent the interaction between the interfacial TCNQ and Al electrode. (b) Plot of $J^{1/2}$ vs (V-V_{bi}) of the single-carrier diodes. (c) Hole mobility (μ_h) and electron mobility (μ_e) for the PC-T0 and PC-T1 devices.

Considerable decrease of electron mobility is observed with PC-T1 devices. To examine whether such decrease is due to changes in film morphologies caused by TCNQ, we analyzed grazing-incidence wide-angle X-ray scattering (GIWAXS) data for both PC-T0 and PC-T1 films.[10] The overall GIWAXS features of PC-T1 film are very similar to those of the PC-T0 film (Figure 4.9). Notably, no distinct new features arise in either lamellar or π-π stacking directions for PC-T1 when compared to PC-T0. This implies the small quantity of TCNQ does not form a separate crystalline phase large enough to be distinguishable by GIWAXS, which is consistent with the similar morphologies of the two films as characterized by AFM (Figure A4.2). It is noted that both films show a preferential face-on orientation. Since the main charge transport is normal to the substrate for vertical devices, we mainly consider high q_z features, which are essentially close for PC-T0 and PC-T1 around 1.79 $Å^{-1}$. More importantly, for PC-T1, the stacking distance corresponding to the low-LUMO electron-transporting COTIC-4F

is almost the same as in pristine COTIC-4F film (d = 0.34 nm). These similar out-of-plane π-π stacking distances further confirms their similar molecular packing behavior for the vertical charge transport (Table 4.1). Thus, the minor morphology variation brought by addition of TCNQ does not seem to pose a major impact on drastically decreased electron mobility. The decrease of electron mobility can be well rationalized by the energy landscape of the PC-T1, where electrons are energetically preferable to transfer from the LUMO levels of the D-A blend to that of TCNQ. The small amount of TCNQ also makes it relatively morphologically isolated and difficult for uninterrupted electron transport, effectively lowering the electron mobilities.

Table 4.1. Summary of the GIWAXS scattering patterns

q_{xy} (Å^{-1})	d (nm)	L_c (nm)	q_z (Å^{-1})	d (nm)	L_c (nm)
PC-T1					
0.31	2.02	2.49	0.34	1.83	2.42
0.36	1.76	5.26	1.79	0.35	2.29
			1.85	0.34	4.20
PC-T0					
0.28	2.26	7.18	0.314	2.00	-
0.34	1.84	6.22	1.794	0.35	2.92
PTB7-Th					
0.27	2.37	5.42	1.63	0.39	1.63
COTIC-4F					
0.35	1.8	29.3	0.42	1.51	5.15
1.83	0.34	6.23	1.85	0.34	5.35

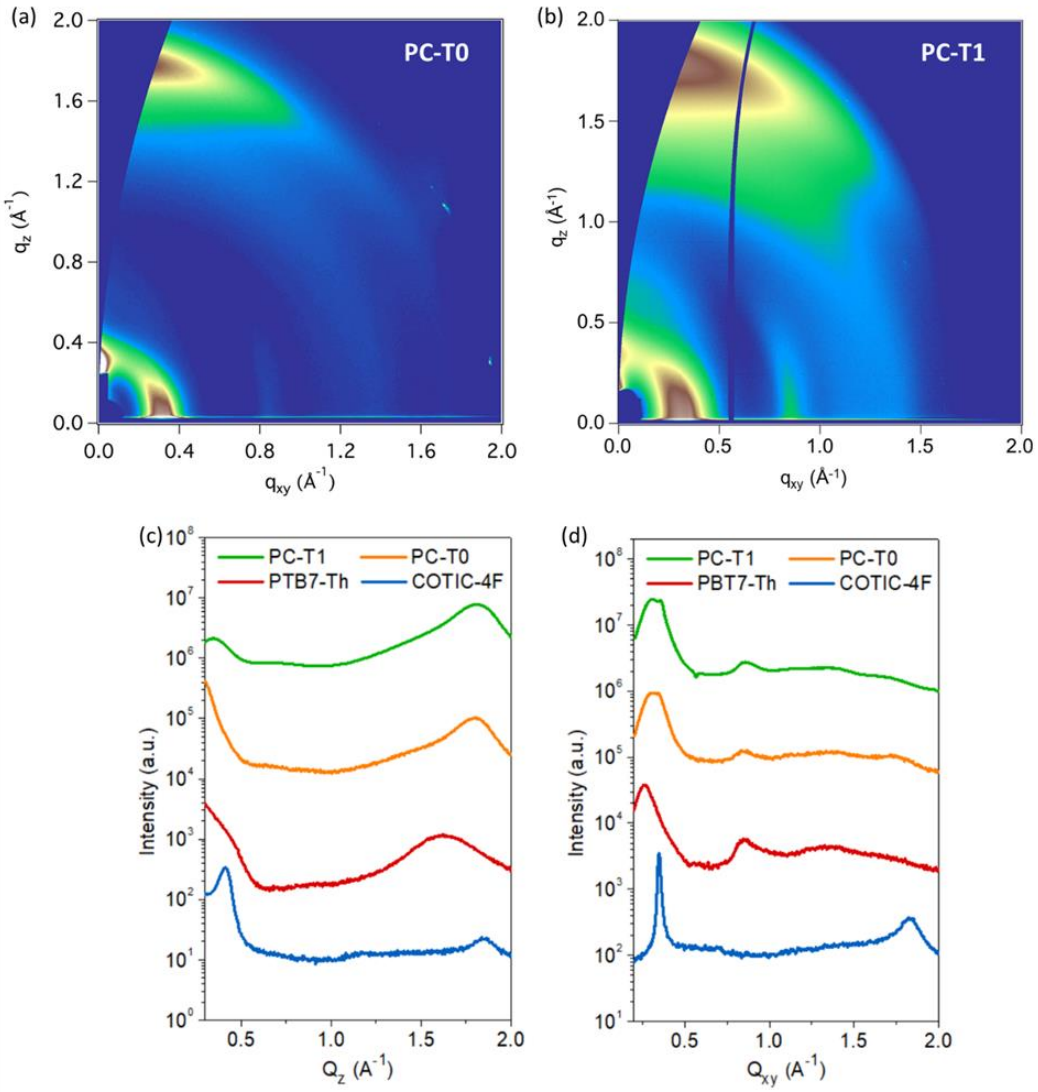

Figure 4.9. 2D GIWAXS images of (a) PC-T0 and (b) PC-T1 films. (c) Out-of-plane and (d) in-plane line-cut features of PC-T0 (orange), PC-T1 (green), PTB7-Th (red) and COTIC-4F (blue) films. Data of PC-T0 and the neat films are extracted from our previous work.[10]

4.3.3 PM Gain Mechanism

With the experimental results shown above, it is proposed that the photocurrent gain originates from the imbalance between hole and electron transport due to the addition of TCNQ. The different schematics of photocurrent generation are shown for the devices with and without TCNQ, respectively. For the devices without TCNQ (Figure 4.10a), the operation

is that of a junction photodiode working in the reverse bias region, where the photogenerated holes and electrons are swept by the externally applied bias and the built-in potential, and collected at the respective electrodes. The carriers contributing to the photocurrent are all from the photogeneration, and thus the EQE cannot surpass 100% due to the inevitable loss in light absorption and charge recombination. For the devices with TCNQ (Figure 4.10b), the bulk TCNQ causes trapping of photogenerated electrons, which will induce extra holes to be injected due to charge neutrality. At the same time, the interfacial TCNQ enhances hole injection by increasing the work function of the Al electrode. Ultimately, the electron trapping and facile hole injection together lead to the net transfer of a large amount of charges from external circuit and manifests it as a strong photocurrent gain.

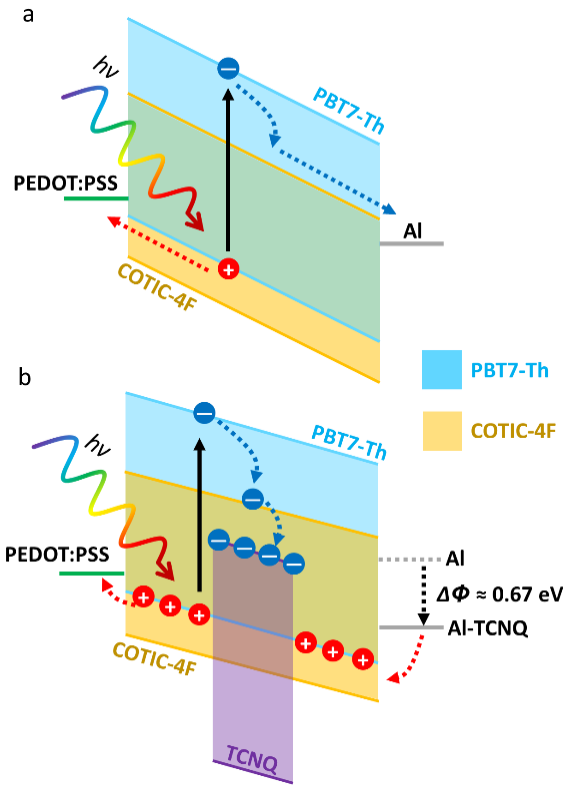

Figure 4.10. A schematic of the photoresponse in the devices (a) without and (b) with TCNQ in the active layer under bias.

4.4 Light Intensity Dependence

The dependence of the photoresponse on the light intensity is probsed for the PC-T1 device. The photocurrent density (J_{ph}) as a function of light intensity (E) is plotted in Figure 4.11a. The slopes of the linear fits in the logarithmic plot are close to unity. Hence, an approximate linear scaling of J_{ph} with light intensity is observed for all biases at lower light intensity. The linear region is followed by a sub-linear region typically observed in the photoconductors at higher light intensity, which is related to the photo-induced saturation of the traps states.[113] The EQE – light intensity relation is shown in Figure 4.11b. Under weak light intensity, the photogeneration rate is low, giving also a low extent of trap filling. There are enough traps available for efficient trapping of photogenerated electrons and for the occurrence of the gain effect. As the photogeneration rate increases with more incident photons, more and more traps are filled by the photogenerated carriers. Ultimately, it leads to less prominent gain effect at higher light intensity.

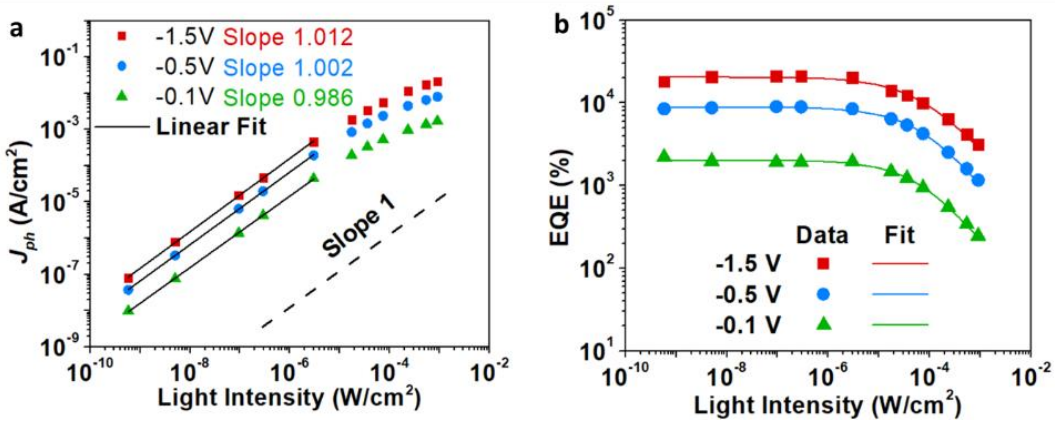

Figure 4.11. (a) Photocurrent density - light intensity and (b) EQE (@940 nm) characteristics under different biases.

The EQE – light intensity characteristics can be well fitted with a photoconductive model:

$$EQE = \eta \left[\frac{1}{1 + (E/E_0)^n} \right] \tag{25}$$

where η is a prefactor, representing the EQE at low light intensity, E_0 is the onset light intensity of trap saturation, and n is a fitting parameter.[63] The similar light intensity threshold where the J_{ph} – light intensity curves turn sub-linear and the weak dependence of both n (0.71-0.77) and E_0 (63.6-70.5 uW/cm^2) on bias suggest that the trap filling is mainly dominated by photogeneration rather than the electric field strength. This also marks the difference from a PM OPD based on trap-enahcned photoconductive gain and a regular rectification photodiode , the latter of which tends to have a higher light intensity threshold when a higher bias is applied due to improved charge collection and alleviated carrier recombination.[57]

4.5 Phototransient Behavior

The transient behavior to incident light is evaluated by the rise time (t_r) and fall time (t_f), defined as the time needed for the photoresponse to rise/fall between 10% and 90% of its steady- state photocurrent change. Figure 4.12a and 4.12b show the normalized transient response of a PC-T1 device upon the introduction/removal of a 940 nm optical signal. The t_r and t_f are estimated to be 0.59 ms and 9.04 ms, respectively, which are much shorter than the typical human response time (250-950 ms to visual stimuli[114]).

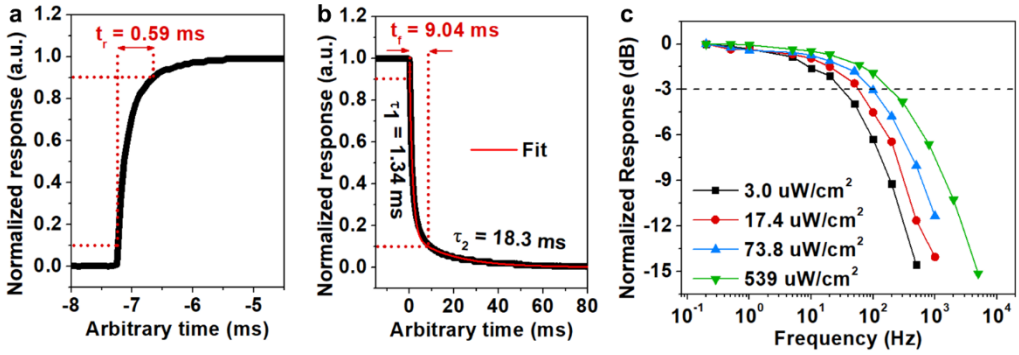

Figure 4.12. Transient (a) rise and (b) decay curves upon application/removal of 940 nm light (~539 uW/cm^2). (c) Normalized response versus frequency under different light intensities.

Exponential fitting of the decay curve in Figure 4.12b finds a faster component of time constant τ_1 = 1.34 ms and a slower component of τ_2 = 18.3 ms, implying multiple pathways for recombination. Deep electron traps induced by LUMO level of TCNQ may have longer trapping release time that cause the slower component in the decay characteristics.[31] The cutoff frequency (f_{3dB}) was evaluated by measuring phototransient response at different modulation frequencies. The f_{3dB} ranges from 30 to 180 Hz at the light intensities from 3 to 539 uW/cm^2 (Figure 4.12c). The slower response speed at low light intensities can be understood as a result from the gain mechanism. At lower light intensities, the degree of trap-filling is lower, and thus rendering the transient behavior is more dominated by the slower process related to the deep traps. Regardless, the speed is still fast enough for the usually involved weak light intensity (<10^{-1} mW/cm^2) in photoplethysmography (PPG) applications.[2]

4.6 Applicability for Other Active Layer Materials

Additionally, devices with and without 1 wt% TCNQ in other two exrta D-A blends as the active layer were prepared to preliminarily probe the applicability of this approach to gain OPDs for other photoactive materials (Figure 4.13a). A small-molecule acceptor, CO1-4Cl from Chapter 1,[58] was coupled with PTB7-Th, and polymer donor poly(3-hexylthiophene), P3HT, was coupled with COTIC-4F. Similarly, the devices without TCNQ do not show EQE above 100% while those with TCNQ can. The PTB7-Th:CO1-4Cl:TCNQ system shows EQE up to about 3500% (Figure 4.13b), while the P3HT:COTIC-4F:TCNQ device delivers EQE between 100% and 200% (Figure 4.13c). We noticed that the PTB7-Th:CO1-4Cl system without TCNQ can achive EQE values close to that of PC-T0 device of the PTB7-Th:COTIC-4F system. Since under large bias, the non-geminate recombination of the free carriers is minimized, such close EQE insinuates their similarly favorable photon capture and

photogeneration. Hence, the performance difference in the TCNQ-present counterparts may be more related to the difference in the electron trapping. Differently for the P3HT:COTIC-4F blend, the much lower EQE (<10%) compared to the other two systems in the case without TCNQ suggests intrinsically inferior photogeneration from this particular D-A combination in the first place, unfavorable for achieving appealing photocurrent gain since the ultimate gain is positively related to the step of photogeneration in the D-A blend. Understandably, the performance for these two blends was obtained without extensive processing optimizations for the specific blends, and the differences in blend crystallinity, phase separation, and energy levels may lead to considerable variations in photogeneration rate, charge mobility, trap density, etc., ultimately manifesting a large difference in photoresponse. Regardless, this initial result suggests the universality of the approach to introduce photocurrent gain to organic BHJ systems.

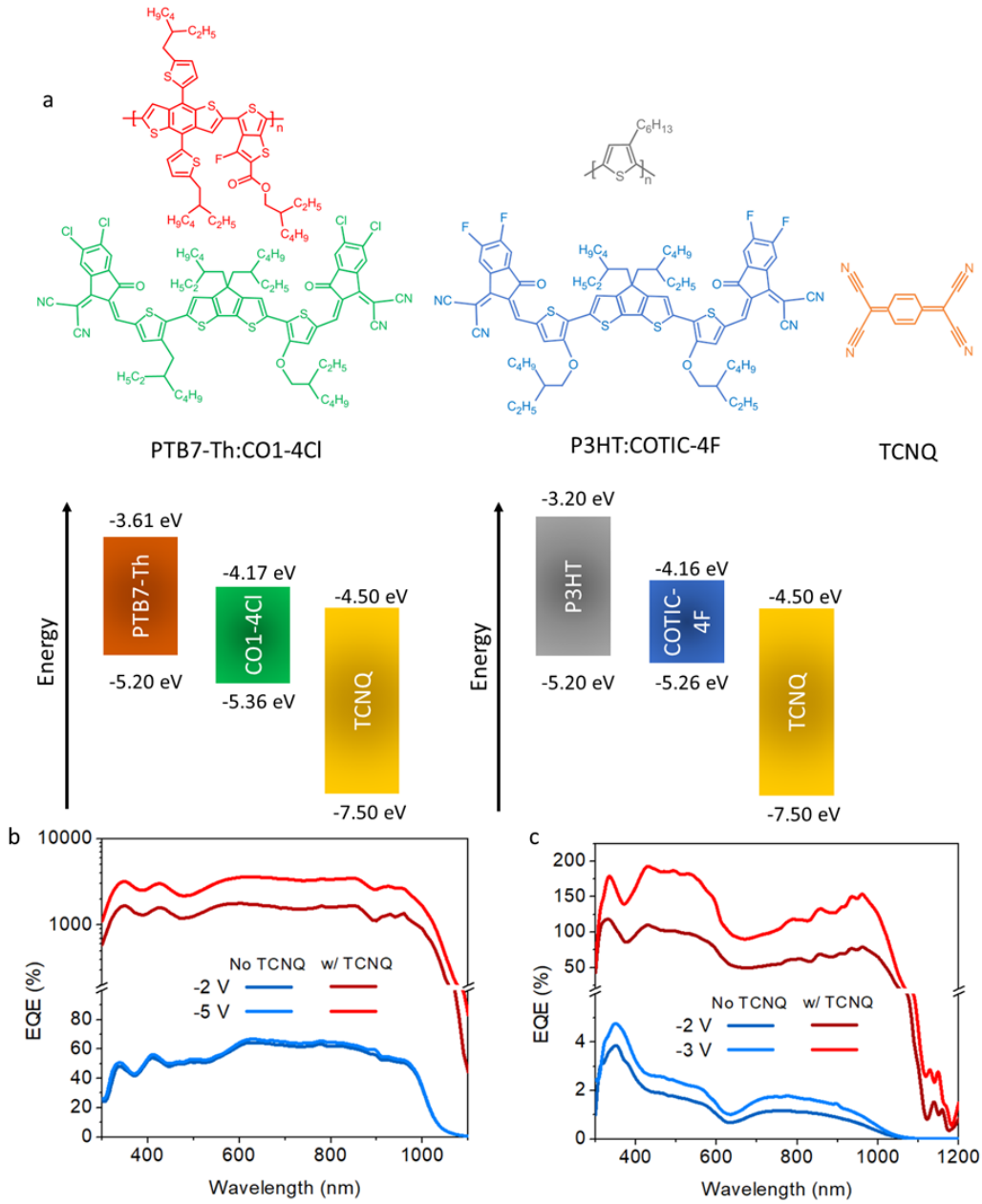

Figure 4.13. (a) Chemical structures and energy diagrams of the materials in the other two blends. EQE profiles of devices with active layers of (b) PTB7-Th:CO1-4Cl:TCNQ (1:1.5:0.025 and 1:1.5:0 weight ratio) and (c) P3HT:COTIC-4F:TCNQ (1:1:0.02 and 1:1:0 weight ratio). The device preparation is similar to that of PC-T*x* devices except that the corresponding the donor or acceptor was varied.

4.7 Experimental

4.7.1 Device fabrication

The ITO substrates were cleaned with deionized water, acetone and isopropanol, respectively. Solutions of PTB7-Th:COTIC-4F:TCNQ (PC-T*x*) with the weight ratio of 1:1.5:*x* (*x* varies to be achieve 0.1 to 1.55 wt% of the PTB7-Th:COTIC-4F total weight) were prepared in chlorobenzene. The fresh solution was kept under stirring at 60 °C for overnight and used the next day to minimize solute aggregation. The cleaned ITO substrates were subject to UV-ozone treatment for 15 min and PEDOT:PSS solution was spun onto the ITO substrates at 2500 rpm for 1 min, followed by thermal annealing at 120 °C for 30 min. Subsequently, the PC-T*x* solution with a concentration of 25 mg/mL was deposited onto the PEDOT:PSS-covered ITO substrates in a nitrogen glovebox by spin coating. The aluminum top electrode was then thermally evaporated onto the active layer under a vacuum level of ~10^{-6} torr. The device area was defined by the overlapping area of the top electrode and pre-patterned ITO bottom electrode, giving a device area of 4.51 mm^2. The devices for TLM tests were made with active layers of PC-T0 and PC-T1 under the same processing condition for the photodetectors. The active layers were deposited on benzocyclobutene-covered SiO_2/Si^{++} substrates, followed by vacuum deposition of 100 nm Al top contacts through shadow masks.

4.7.2 Spectroscopic Analysis

Fourier-transform infrared (FT-IR) spectroscopy of pristine TCNQ and Al vapor treated TCNQ powders were performed using a Perkin Elmer Spectrum Two spectrometer with a universal attenuated total reflectance (UATR) attachment.

4.7.3 Thin-film Characterizations

Contact potential and thin film morphologies were obtained from an Asylum MFP-3D atomic force microscope with amplitude modulation SKPM (AM-SKPM) under an inert atmosphere. A single Au-coated Si tip with a resonant frequency of 300 kHz and a force constant of 40 N m^{-1} was used in a two-pass scanning method. The images were processed using first order image flattening and all images were analyzed on Asylum Research AFM software version 14, programmed using IGOR Pro.

The GIWAXS data was collected at the Advanced Light Source at Lawrence Berkeley National Lab on the 7.3.3 beamline. The samples prepared on silicon substrates were scanned with an incidence angle of 0.12° and a photon energy of 10 keV (λ = 1.24 Å), while under a helium environment to minimize beam damage and reduce air scattering. The width of the incident X-ray beam is about 1 mm, and silver behenate was used to calibrate the lengths in the reciprocal space. A 2D detector (PILATUS 2 M from Dectris) with a sample-to-detector distance of 276.9 mm was used to collect the images. The Nika software package for Igor (by Wavemetrics) and the Igor script WAXStools were used to process the image.

4.7.4 Device Characterizations

The current-voltage data were collected with a Keithley 4200 semiconductor characterization system. The EQE was measured with a monochromatic light source with a modulation frequency of 35 Hz. The current signal was amplified with a low-noise pre-amplifier (SRS 570) and recorded with an SR810 DSP lock-in amplifier (Stanford Research System). Calibration was done with reference silicon and germanium photodiodes. For the light intensity-photocurrent measurement, calibrated 940 nm light-emitting diodes (LEDs) were used as the light source, and the signals from the devices under test were fed to the pre-

amplifier and collected with a lock-in amplifier (AMETEK SI 5210). The light intensity was varied by a set of neutral filters. To measure the phototransient behavior of the devices, a function generator (SRS DS345) was employed to supply square-wave AC voltage to the 940 nm LEDs to generate pulsed optical signal. The response from the photodetector was obtained with an oscilloscope (Keysight DSOX3022T).

Chapter 5

Conclusions and Outlooks

5.1 Summary of the PhD Work

This PhD work mainly involves studying organic photodetectors (OPDs) based on highly efficient BHJ systems. The work largely focuses on device engineering and device physics aiming to provide routes toward better broadband sensing performance, as well as understanding of the device behaviors.

First of all, in order to achieve high sensitivity in the NIR region, a novel ultranarrow bandgap non-fullerene acceptor, CO1-4Cl, has been used to construct high-performance solution-processed BHJ OPDs. In terms of photoresponse performance, the optimized OPDs can achieve a high maximum responsivity > 0.5 A W^{-1} in the NIR region beyond 900 nm, surpassing existing organic photodiodes in a broad NIR spectrum, to the best of our knowledge. In addition to shunt leakage, we have also determined that the injection current also has significant contribution to the dark current. The onset of charge injection can be effectively postponed with the thick junction strategy, without significantly compromising the photoresponse thanks to the efficient charge collection. Consequently, we are able to obtain a D^* as high as 10^{12} *Jones* based on experimentally measured noise level by fast Fourier transform of the dark current. We then studied the operating bandwidth (f_{-3dB}) of the OPDs and found a f_{-3dB} of 240 kHz, which is determined to be limited by the carrier transit time. The high responsivity, low noise, and fast detector speed make the OPDs applicable for practical applications such as real-time heart rate monitoring by photoplethysmography.

Subsequently, the focus shifts from getting the excellent figures-of-merit of the OPDs to stability and consistency of the figures-of-merit. Specifically, we analyzed a detrimental behavior where the magnitude of the dark current depends on the illumination history of the device, a universal problem found for OPDs based on inverted structure. We identified that the issue originated from the loss of selectivity and enhanced hole transport of the ZnO interlayer following its exposure to high energy photons ($h\nu > E_{g,opt}$, primarily UV) by various control experiments. To proactively counter it, we screened a series of materials as potential alternative to the ZnO interlayer, which need to meet four requirements: 1) illumination history insensitivity, 2) well suppressed low dark current, 3) uncompromised photoresponse and 4) uncompromised detector speed. We noticed that while certain options meet one or two of the requirements, finding one to suffice all of them is challenging. Through extensive examination, "multilayer" SnO_2 layer was finally identified as an adequate solution to the problem, which rendered the dark current characteristics minimally sensitive to illumination processes, low magnitude of the dark current below 10 nA/cm^2, close to the initial dark current exhibited by the ZnO-based devices without UV exposure history, and well retained outstanding photoresponse and phototransient response. Our findings here emphasize a must where the stability of the dark current should also be concerned for photodetection application, and the long-overdue necessity of examining the complications of illumination on the dark current characteristics of OPDs.

Lastly, an attempt was made to introduce a certain photomultiplication gain effect to a broadband active BHJ system. To do so, a small quantity of deep-LUMO TCNQ as electron trap agents were added into the BHJ blend. This results in strong PM effect with not only favorable EQE > 10^4 %, but also small operation voltages (0.5-1.5 V), a wide span of spectral

response (300 – 1200 nm), as well as decent detector speed faster than humans. By examining the effect of TCNQ on both the organic/metal interface and the bulk of the BHJ layer, the origin of the observed large photocurrent gain was determined to be from the metal-TCNQ interaction and electron trapping by bulk TCNQ. The inerfacial TCNQ interacts with the Al contact and deepens its work function to facilitate hole transport, whereas the bulk TCNQ trapped the photogenerated electrons. These effects essentially convert the device behavior from that of a regular junction photodiode to a photoconductor with excessive trapping sites for electrons. Due to charge neutrality, the trapped electrons induced extra hole injection, made possible by the deepened work function due to the TCNQ-Al interaction at the contact. We also found that the strategy is readily applicable to other BHJ systems, although optmization would be needed for better performance for each case.

5.2 Outlooks for Organic Photodetectors Development

OPDs hold great promise in the development of next-generation optoelectronics. Some of their unique features may be used to realize interesting advantages and novel applications usually not accessible by crystalline inorganic semiconductors. For example, the full stack of OPDs can be tailored into ultrathin (semi)transparent sheet, applicable for IR sensing while allowing partial transmittance of visible light, which is useful for an application where simultaneous receipt of visible light by human eye and detection of IR light by machines are desired. In addition, the characteristic Frenkel excitation of organic semiconductors can be exploited to tune the spectral response profile of the OPDs when the dissociation of excitons generated by the photons of targeted wavelength can be hindered by rational design the active thickness and/or vertical component distribution. This can lead to narrowband response which would otherwise require additional filters for conventionally used inorganic photodetectors.

Regardless of these advantages tied to the organic semiconductors, for the OPDs to compete more favorably with the currently commercial photodetectors based on crystalline/amorphous inorganic semiconductors, there are still some challenges in several key aspects that need to be better addressed.

First, the success of OPDs in sensing long wavelength light is still limited. On this matter, the inorganic counterparts still outperform most OPDs. For example, even under non-cryogenic temperatures, Ge, InGaAs and InAs can achieve spectral cutoff over 1500 nm, 1700 nm and 3000 nm, respectively. While the material development of narrow bandgap organic semiconductors has demonstrated possibility of extending the spectral sensitivity to the near infrared region up to 1400 nm, ambitions further pushing spectral activity into short-wave near infrared (SWIR, 1400 nm to 3000 nm) is no trivial. This challenge partially stems from the difficulties in synthesis to simultaneously secure small bond length alternation and decent solubility by attaching aliphatic side chains.[115] In addition, molecular designs that solely target narrowing bandgap does not necessarily lead to favorable photogeneration in BHJ since the charge transfer and morphology may also be negatively affected by structures that favor bandgap narrowing.

Second, the stability of the OPDs should also be concerned. Arguably, the stability issue is not as critical as their photovoltaic counterparts, i.e., the organic solar cells, owing to both its usually milder (weaker light intensity and less heat induced by intense irradiation) operation condition and less economic demand of the energy payback time. However, as a potential platform for photosensing and optical communication applications, the devices must demonstrate stable and consistent figures-of-merit under their designated working conditions. Due to the sensitivity of the organic semiconductors and their organic/metal (oxide) interfaces

toward the environment (moisture, oxygen, heat, UV light, etc.), the OPDs require good encapsulation to ward off these usually detrimental factors. Apart from external factors, the intrinsic thermodynamics of the morphology/phase of the BHJ also plays a role. The optimized film morphology itself may not be in a thermodynamically favorable state, making possible gradual changes of the active layer film to move away from the optimized condition over time.[116] Another relevant matter is the stability of OPDs in the currently established semiconductor manufacturing and packaging processes, where harsh temperature for interconnects welding and/or annealing of other adjacent structures are unavoidable, even with inert protective atmosphere. This puts extra importance on curbing undesirable morphological changes of the BHJ layer and the interfaces in the device.

Third, the OPD response speed is also relatively slow, with very few exceptions reaching into the megahertz region for the -3dB cutoff frequency. Typically, for rectifying photodiode devices operated under reverse bias, the speed is limited either by the RC time constant, or the carrier transit time, or their combinatory effect if they happen to have similar influence. Since organic semiconductors usually have low dielectric constants, the junction capacitance of OPDs is usually not very large. The series resistance of the devices are not particularly large, either. These typically render a small RC time constant and a RC time constant-limited cutoff frequency in the megahertz region, as shown in Section 2.8. For OPDs, the limiting factor is usually found to be the carrier transit time, ultimately originating from the relative low carrier mobility on the order of 10^{-6} cm^2 V^{-1} s^{-1} to 10^{-1} cm^2 V^{-1} s^{-1} of organic semiconductors, significantly outperformed by those of over 10 cm^2 V^{-1} s^{-1} and 1000 cm^2 V^{-1} s^{-1} of poly- and single-crystalline Si, respectively. Strategies such as increasing the applied electric field or reducing the thickness of organic layer can help to improve the response speed, yet may

concurrently lead to undermined performance of dark/noise current. The ultimate solution toward a faster phototransient behavior of OPDs is to design high mobility organic semiconductors and better controlled thin-film molecular packing to allow intrinsically improved vertical carrier mobility to reduce the transit time.

In spite of these challenges, the field is fast growing, and has witnessed extensive progress in various aspects in the past couple of decades. With many of the mentioned issues being tackled by synthetic chemists, device physicists and process engineers, it is believed that the OPDs will see more opportunity of commercialization and weigh more heavily in the field of photodetectors in the future.

Appendices

Appendix to Chapter 2

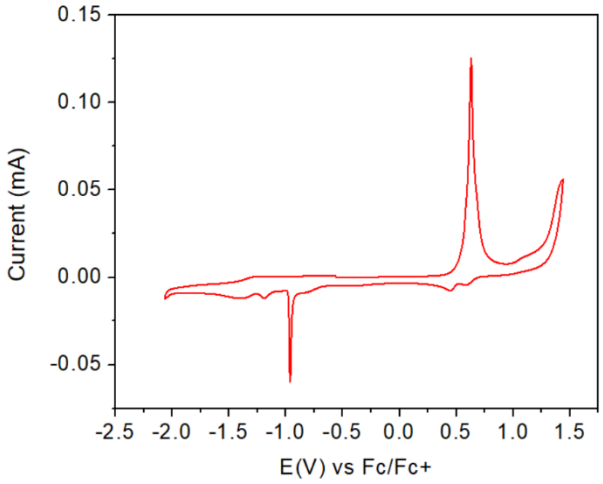

Figure A2.1. Cyclic voltammogram of CO1-4Cl. The levels of highest occupied molecular orbital ($HOMO_{(CV)}$) and the lowest unoccupied molecular orbital ($LUMO_{(CV)}$) derived from the electrochemical cyclic voltammogram data are -5.36 eV and -3.87 eV, respectively.

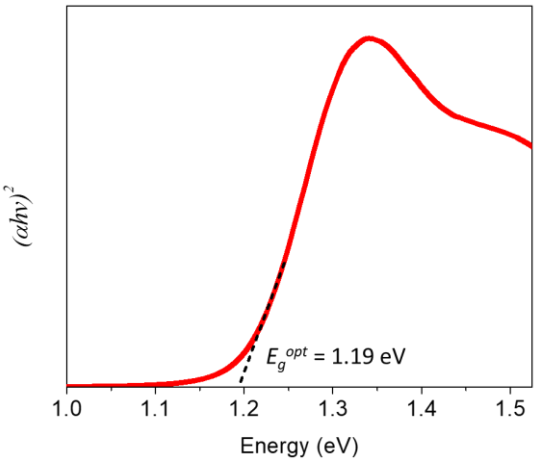

Figure A2.2. Tauc plot of CO1-4Cl.

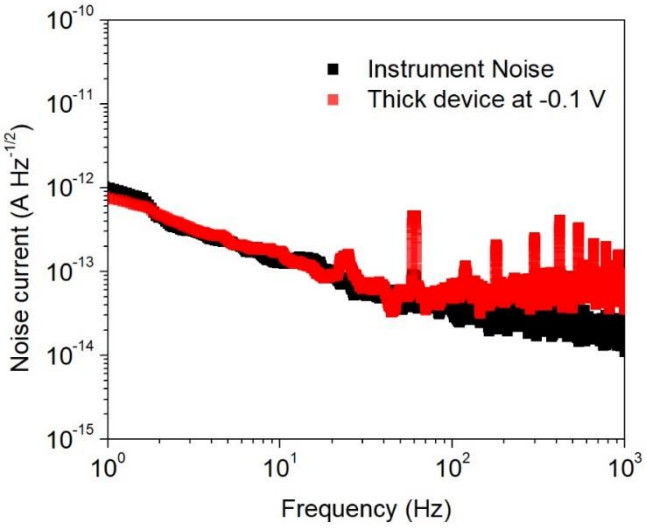

Figure A2.3. Comparison of the background instrument noise and the noise from the thick device at -0.1 V. The background instrument noise was measured in the same condition as when the OPDs were measured except that the OPD devices were removed from the sample holder.

The noise signals from the instrument beyond ~70 Hz is smaller than the noise level measured with the device in presence, but is still on the magnitude of 10^{-14} A $Hz^{-1/2}$, much larger than the calculated shot noise limit. This observation explains the discrepancy between the theoretical shot noise (dashed lines in Figure 2.8) and the actually measured noise level in the frequency-independent region, and indicates the background noise from the measurement setups as the limiting factor for detecting ultra-small signal when the dark current is small.

Table A2.1. Summary of GIWAXS scattering patterns of the donor, acceptor and their blend films.

PTB7-Th:CO1-4Cl					
In-Plane			Out-of-Plane		
q_{xy} (Å^{-1})	d (nm)	L_c (nm)	q_z (Å^{-1})	d (nm)	L_c (nm)
0.3	2.11	5.48	1.79	0.35	2.25
0.36	1.74	5.53	1.85	0.34	3.75
0.85	0.74	5.09			
0.91	0.69	2.8			
PTB7-Th					
In-Plane			Out-of-Plane		
q_{xy} (Å^{-1})	d (nm)	L_c (nm)	q_z (Å^{-1})	d (nm)	L_c (nm)
0.27	2.33	5.1	1.63	0.39	1.11
0.87	0.72	1.8			
CO1-4Cl					
In-Plane			Out-of-Plane		
q_{xy} (Å^{-1})	d (nm)	L_c (nm)	q_z (Å^{-1})	d (nm)	L_c (nm)
0.35	1.8	17.4	0.42	1.48	5.65
0.37	1.69	15.14	1.65	0.38	1.22
			1.85	0.34	2.61

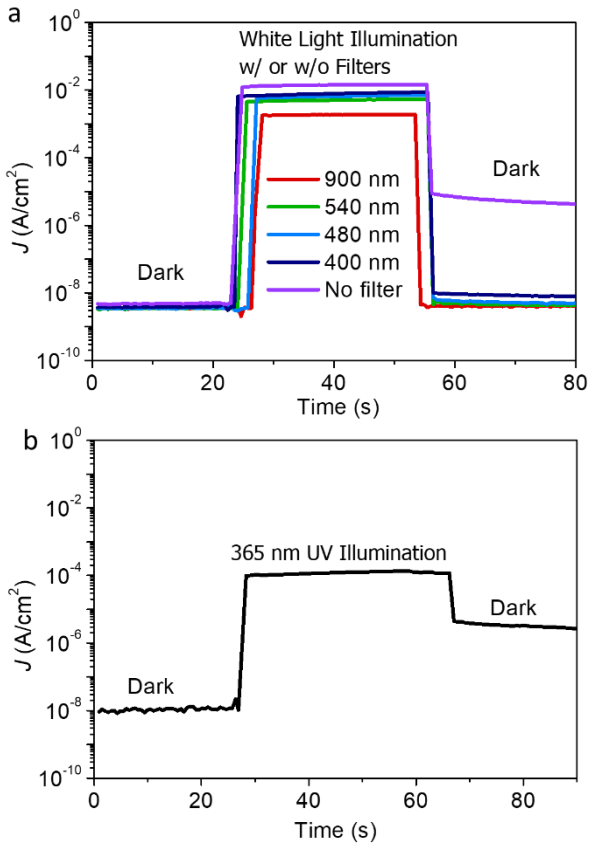

Figure A3.1. (a) Current density *versus* time of a freshly made OPD device measured at -1 V. The illumination processes have long-pass filtering that blocks the light with wavelength below the indicated numbers. The tests were done in the same order as shown in Figure 3.4a. (b) Current density *versus* time of a freshly made OPD device measured at -1 V under the dark, UV illumination (~7 mW/cm^2) and dark conditions.

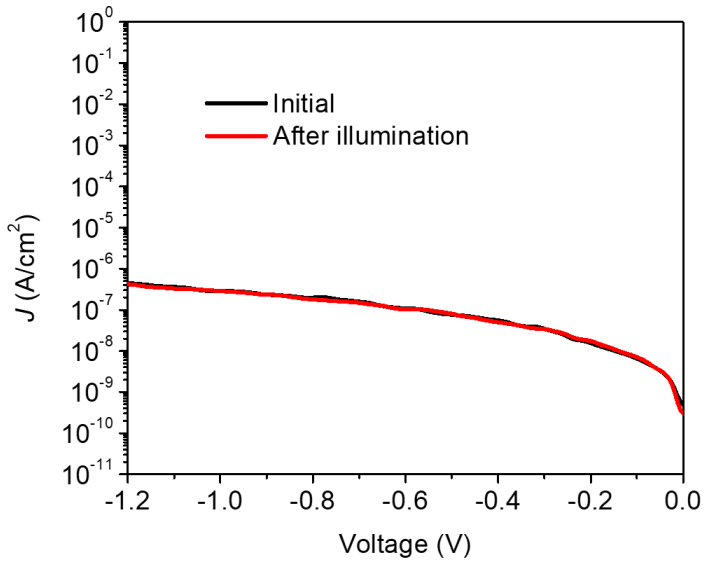

Figure A3.2. Dark *J-V* curves of conventional structure device with ZnO ETL (TIO/PEDOT:PSS/Active Layer/ZnO/Al). Interestingly even with ZnO in presence, the conventional structure device does not show the illumination-history sensitivity of the dark current, which may imply the behavior is also uniquely associated with the inverted device structure.

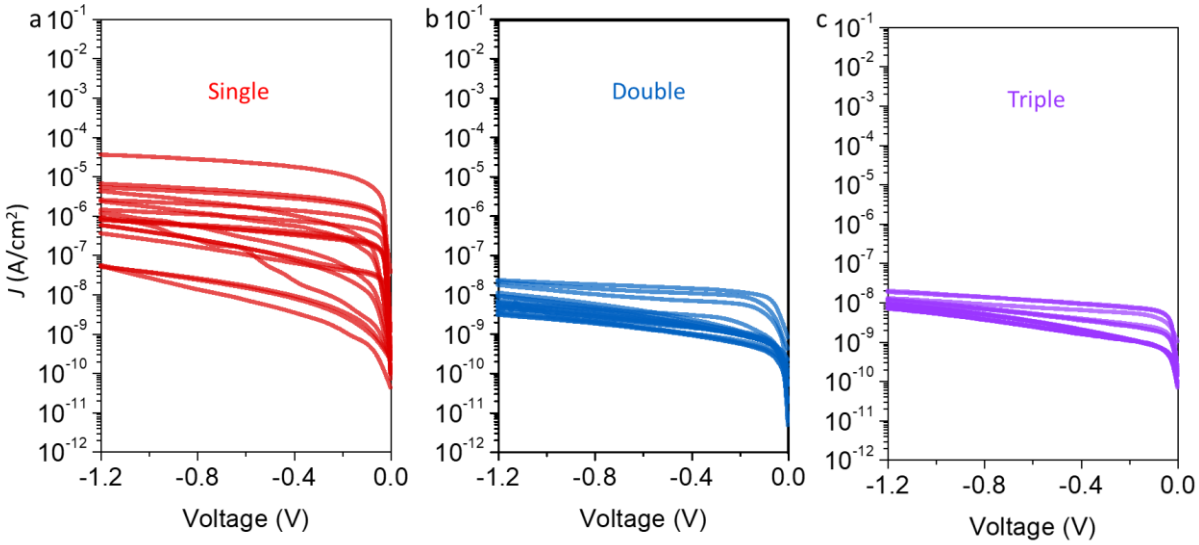

Figure A3.3. Reverse bias dark *J-V* curves of the devices based on (a) "single" layer, (b) "double" layer and "triple" layer SnO_2 ETLs. Each group has 18 devices.

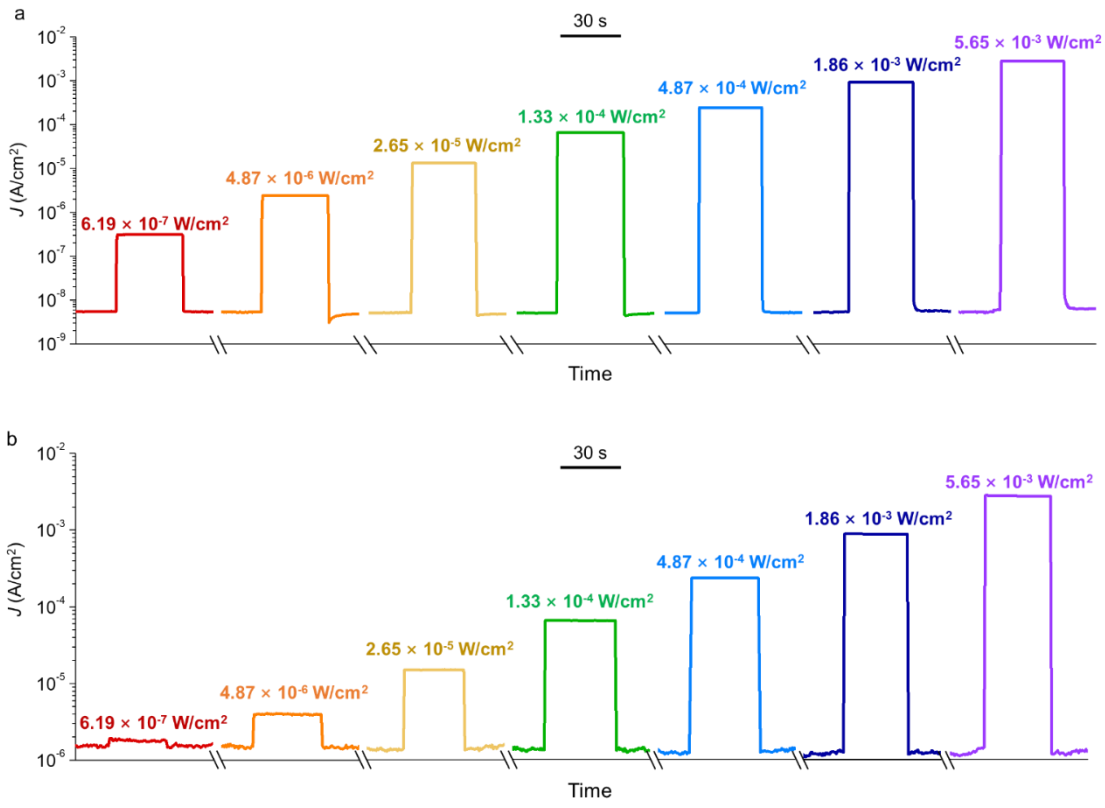

Figure A3.4. Current response at -1 V to different intensities of 940 nm light for the OPDs based on (a) SnO_2 and (b) ZnO ETLs.

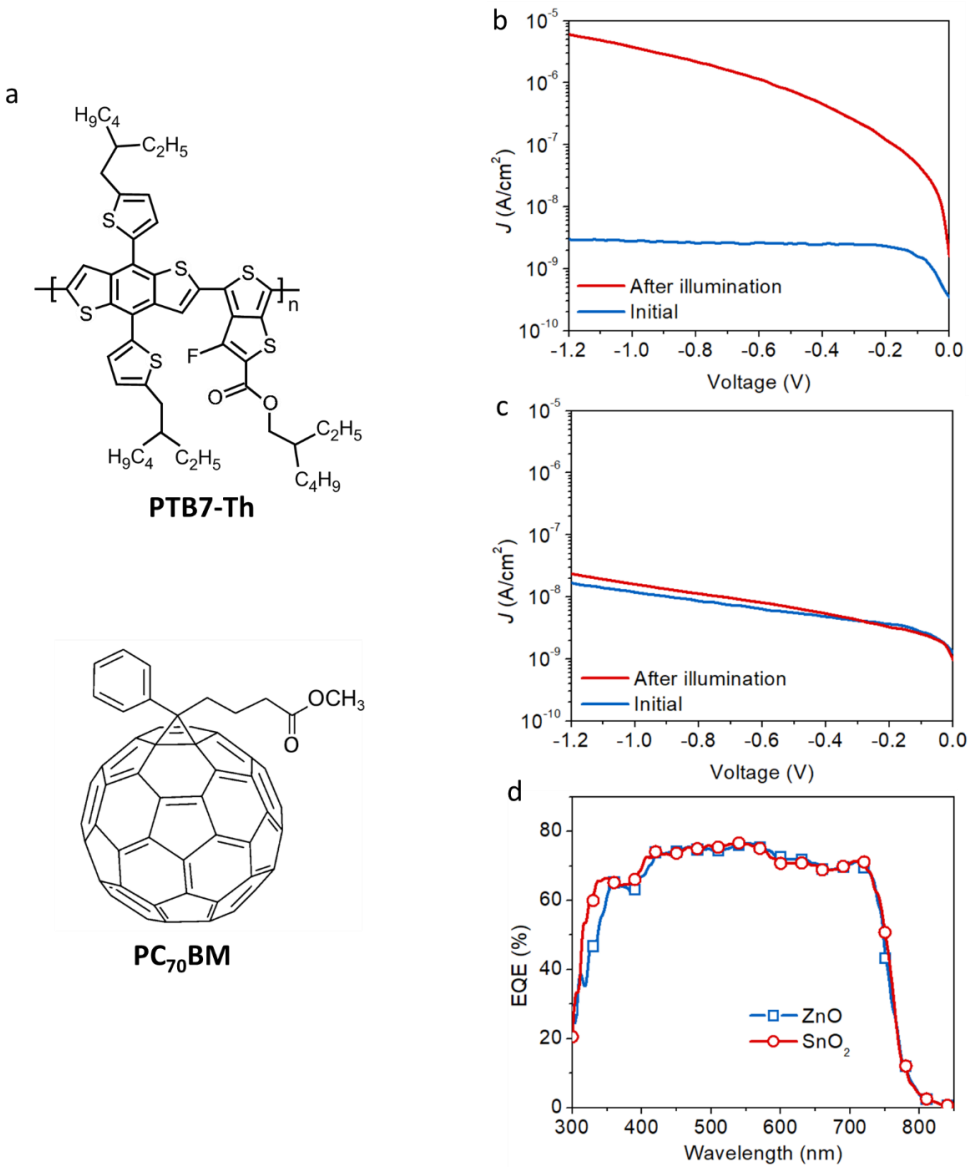

Figure A3.5. (a) Chemical structures of PTB7-Th and $PC_{70}BM$. Initial and after-illumination dark *J-V* characteristics of the devices with (b) ZnO and (c) SnO_2 as the ETL. (d) EQE profiles of PTB7-Th:$PC_{70}BM$ OPDs with ZnO or SnO_2 as the ELT at -1 V.

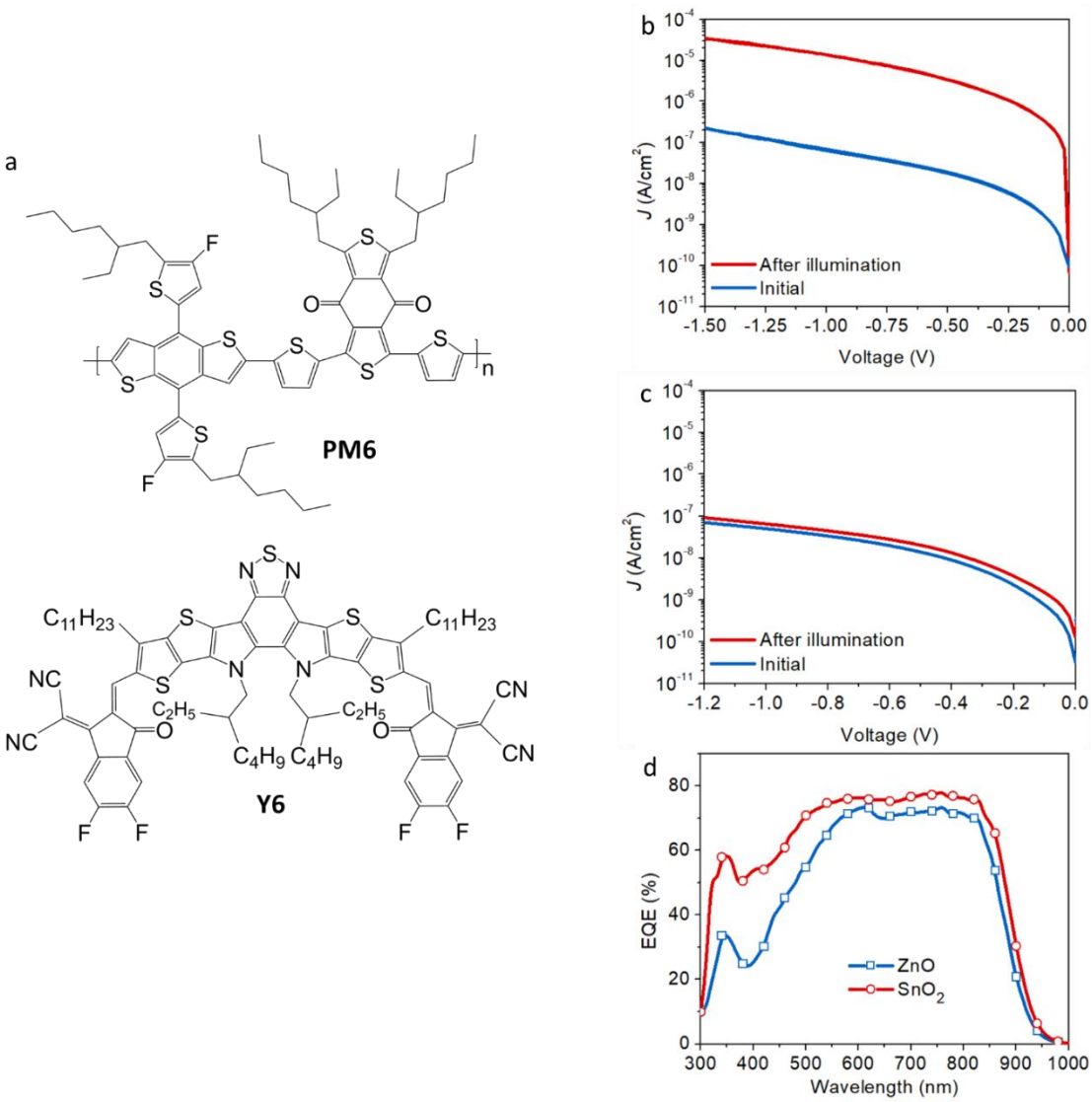

Figure A3.6. (a) Chemical structures of PM6 and Y6. Initial and after-illumination dark *J-V* characteristics of the devices with (b) ZnO and (c) SnO_2 as the ETLs. (d) EQE profiles of PM6:Y6 OPDs with ZnO or SnO_2 as the ETL at -1 V.

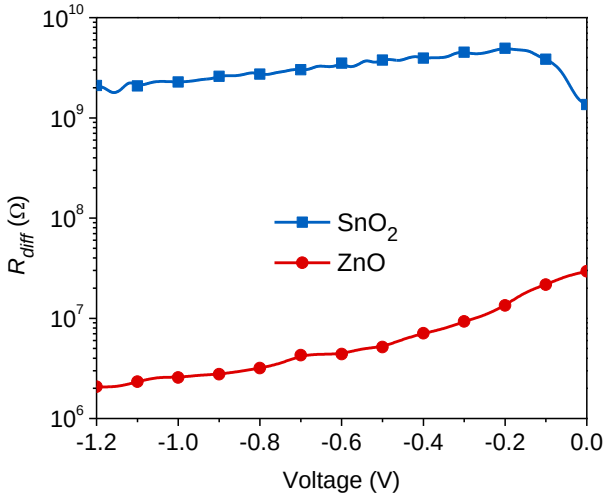

Figure A3.7. Differential resistance derived from the after-illumination dark current-voltage characteristics of the OPD devices based on ZnO and SnO_2 ETLs.

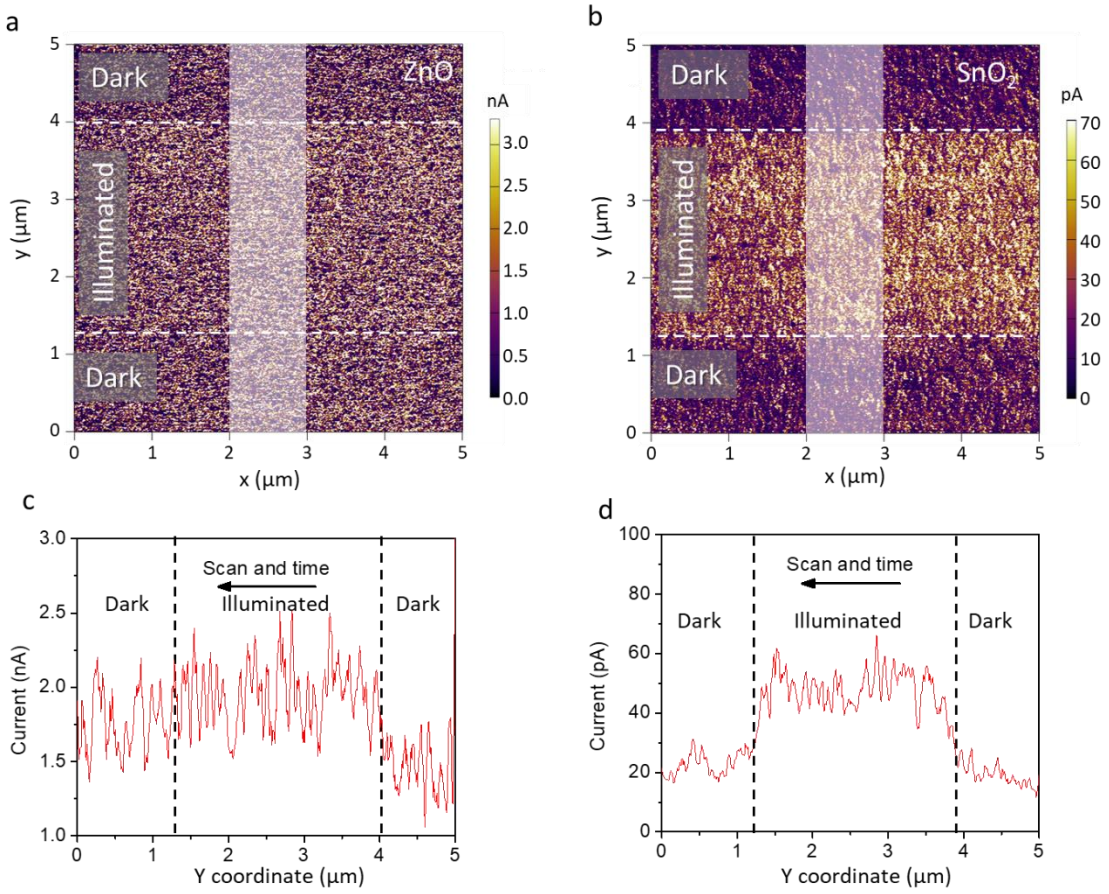

Figure 3.8. Conductive atomic force microscopy (c-AFM) images collected at 1 V for (a) ZnO and (b) SnO_2 films. The scan was taken from top (vertical position 5 μm) to bottom (vertical position 0 μm) under first dark, then illuminated, and finally dark conditions. (c-d) Current-vertical coordination characteristics extracted from (a) and (b). The data in (c) and (d) is averaged from current values in the 1 μm lateral width indicated by the white area. The black dashed lines in (c) and (d) indicate the illumination conditions during the scan. Please note that ***the dashed lines indicate only the position of the probe at which illumination was applied or removed. When illumination was applied, the whole areas in Figure A3.8a and A3.8b were illuminated.***

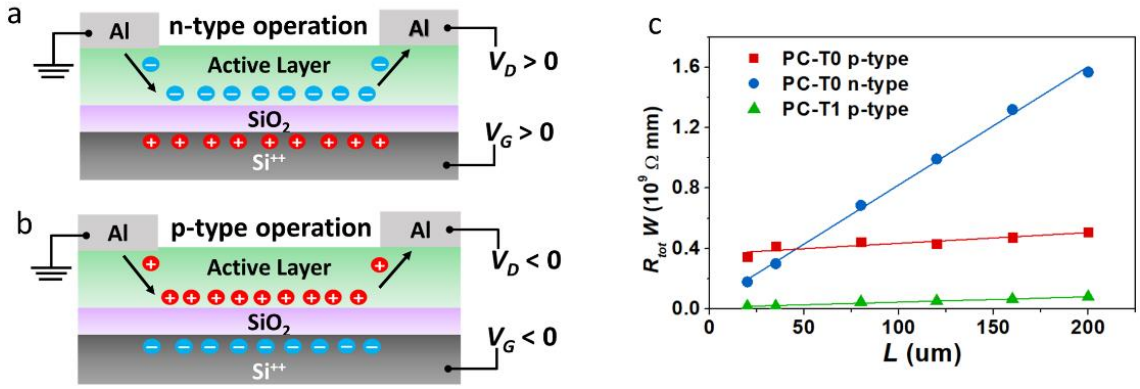

Figure A4.1. Schematic of gate field-effect controlled charge transport allowing selectively probing the R_{ct} when the majority carriers are (a) electrons and (b) holes. (c) Plot of width-normalized total resistance (R_{tot} W) vs channel length (L) for the FETs with 1% and without TCNQ operated under n-type transport and p-type transport.

The major contributing type of carriers toward the charge transport and the measured current can be modulated by the gate potential, allowing us to obtain R_{ct} values that reflect the interfacial charge transport for holes and electrons separately. To make the condition more relevant to the vertical photodetectors, top-contact device architecture was adopted, and Al was used as the electrode. By extrapolating the width-normalized total resistance ($R_{tot} \cdot W$) to the zero-channel length (L = 0), one can obtain the width-normalized contact resistance ($R_{ct} \cdot W$) according to the following equation:

$$R_{tot}W = \frac{V_D}{I_D}W = R_{ct}W + \frac{L}{\mu_{FET}C_i(V_G - V_T)} \qquad (A1)$$

where R_{tot} is the total resistance, V_D is the drain voltage, I_D is the drain current, R_{ct} is the contact resistance, μ_{FET} is the field-effect carrier mobility, C_i is the areal capacitance of the dielectric layer, V_G is the gate voltage and V_T is the threshold voltage. It is noted that the devices based on PC-T1 are unable to be operated as n-type OFETs due to intensified electron trapping caused by TCNQ, and therefore, it is not possible to extract the $R_{ct} \cdot W$ under n-type

transport for the PC-T1 to compare with the $R_{ct} \cdot W$ (3.90×10^7 Ω·mm) of the TCNQ-absent PC-T0.

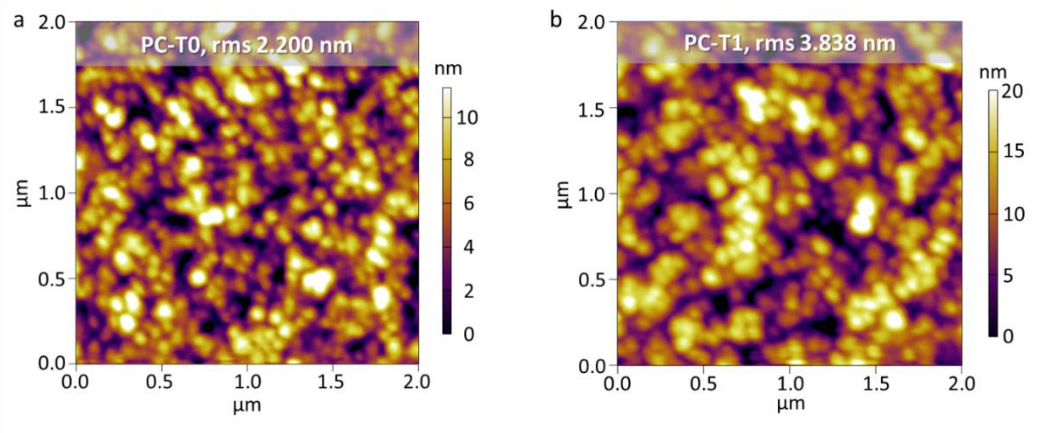

Figure A4.2. AFM height images of the active layers of (a) PC-T0 and (b) PC-T1.

References

1. Li, Q., Guo, Y. & Liu, Y. Exploration of Near-Infrared Organic Photodetectors. *Chem. Mater.* **31**, 6359–6379 (2019).
2. Liu, X., Lin, Y., Liao, Y., Wu, J. & Zheng, Y. Recent advances in organic near-infrared photodiodes. *Journal of Materials Chemistry C* **6**, 3499–3513 (2018).
3. Wang, H. & Ha Kim, D. Perovskite-based photodetectors: materials and devices. *Chemical Society Reviews* **46**, 5204–5236 (2017).
4. Yokota, T. *et al.* Ultraflexible organic photonic skin. *Science Advances* **2**, e1501856 (2016).
5. Yokota, T. *et al.* A conformable imager for biometric authentication and vital sign measurement. *Nature Electronics* **3**, 113–121 (2020).
6. Isorg obtains FBI certification for security market's first organic photodiode-based module for fingerprint scanners. https://www.isorg.fr/news/.
7. Simone, G., Dyson, M. J., Meskers, S. C. J., Janssen, R. A. J. & Gelinck, G. H. Organic Photodetectors and their Application in Large Area and Flexible Image Sensors: The Role of Dark Current. *Advanced Functional Materials* **30**, 1904205 (2020).
8. García de Arquer, F. P., Armin, A., Meredith, P. & Sargent, E. H. Solution-processed semiconductors for next-generation photodetectors. *Nature Reviews Materials* **2**, 16100 (2017).
9. Lee, J. *et al.* Side Chain Engineering of Non-Fullerene Acceptors for Near-Infrared Organic Photodetectors and Photovoltaics. *ACS Energy Lett.* **4**, 1401 (2019).
10. Lee, J. *et al.* Bandgap Narrowing in Non-Fullerene Acceptors: Single Atom Substitution Leads to High Optoelectronic Response Beyond 1000 nm. *Advanced Energy Materials* **8**, 1801212 (2018).
11. Armin, A., Jansen-van Vuuren, R. D., Kopidakis, N., Burn, P. L. & Meredith, P. Narrowband light detection via internal quantum efficiency manipulation of organic photodiodes. *Nat Commun* **6**, 6343 (2015).
12. https://www.isorg.fr/.
13. https://www.nikkoia.com/en/press-reviews/699/.
14. Brütting, W. Physics of Organic Semiconductors. *physica status solidi (a)* **201**, 1031–1031 (2004).
15. Bässler, H. & Köhler, A. Charge Transport in Organic Semiconductors. in *Unimolecular and Supramolecular Electronics I* (ed. Metzger, R. M.) vol. 312 1–65 (Springer Berlin Heidelberg, 2011).
16. Pope, M. & Swenberg, C. E. *Electronic Processes in Organic Crystals and Polymers*. (Oxford University Press, 1999).
17. Ran, N. A. *et al.* Understanding the Charge-Transfer State and Singlet Exciton Emission from Solution-Processed Small-Molecule Organic Solar Cells. *Advanced Materials* **26**, 7405–7412 (2014).
18. Wadsworth, A., Hamid, Z., Kosco, J., Gasparini, N. & McCulloch, I. The Bulk Heterojunction in Organic Photovoltaic, Photodetector, and Photocatalytic Applications. *Adv. Mater.* **32**, 2001763 (2020).
19. Tang, C. W. Two-layer organic photovoltaic cell. *Appl. Phys. Lett.* **48**, 183–185 (1986).
20. Yu, G., Gao, J., Hummelen, J. C., Wudl, F. & Heeger, A. J. Polymer Photovoltaic Cells: Enhanced Efficiencies via a Network of Internal Donor-Acceptor Heterojunctions. *Science* **270**, 1789–1791 (1995).

21. Hiramoto, M., Fujiwara, H. & Yokoyama, M. p-i-n like behavior in three-layered organic solar cells having a co-deposited interlayer of pigments. *Journal of Applied Physics* **72**, 3781–3787 (1992).
22. Liu, F. *et al.* Organic Solar Cells with 18% Efficiency Enabled by an Alloy Acceptor: A Two-in-One Strategy. *Advanced Materials* **33**, 2100830 (2021).
23. Strobel, N., Seiberlich, M., Rödlmeier, T., Lemmer, U. & Hernandez-Sosa, G. Non-Fullerene-Based Printed Organic Photodiodes with High Responsivity and Megahertz Detection Speed. *ACS Appl. Mater. Interfaces* **10**, 42733–42739 (2018).
24. Simone, G. *et al.* On the Origin of Dark Current in Organic Photodiodes. *Adv. Optical Mater.* 1901568 (2019).
25. Gielen, S. *et al.* Intrinsic Detectivity Limits of Organic Near-Infrared Photodetectors. *Advanced Materials* **32**, 2003818 (2020).
26. Fang, Y. & Huang, J. Resolving Weak Light of Sub-picowatt per Square Centimeter by Hybrid Perovskite Photodetectors Enabled by Noise Reduction. *Advanced Materials* **27**, 2804–2810 (2015).
27. Xiong, S. *et al.* Universal Strategy To Reduce Noise Current for Sensitive Organic Photodetectors. *ACS Appl. Mater. Interfaces* **9**, 9176–9183 (2017).
28. Jones, R. C. Quantum efficiency of photoconductors. in *Proc. IRIS* vol. 2, 9 (1957).
29. Gong, X. *et al.* High-Detectivity Polymer Photodetectors with Spectral Response from 300 nm to 1450 nm. *Science* **325**, 1665–1667 (2009).
30. Fang, Y., Armin, A., Meredith, P. & Huang, J. Accurate characterization of next-generation thin-film photodetectors. *Nature Photonics* **13**, 1 (2019).
31. Guo, F. *et al.* A nanocomposite ultraviolet photodetector based on interfacial trap-controlled charge injection. *Nature Nanotechnology* **7**, 798–802 (2012).
32. Konstantatos, G., Clifford, J., Levina, L. & Sargent, E. H. Sensitive solution-processed visible-wavelength photodetectors. *Nature Photon* **1**, 531–534 (2007).
33. Kielar, M., Dhez, O., Pecastaings, G., Curutchet, A. & Hirsch, L. Long-Term Stable Organic Photodetectors with Ultra Low Dark Currents for High Detectivity Applications. *Scientific Reports* **6**, (2016).
34. Collins, S. D. *et al.* Observing Ion Motion in Conjugated Polyelectrolytes with Kelvin Probe Force Microscopy. *Advanced Electronic Materials* **3**, 1700005 (2017).
35. Melitz, W., Shen, J., Kummel, A. C. & Lee, S. Kelvin probe force microscopy and its application. *Surface Science Reports* **66**, 1–27 (2011).
36. Xu, H. *et al.* Flexible Organic/Inorganic Hybrid Near-Infrared Photoplethysmogram Sensor for Cardiovascular Monitoring. *Advanced Materials* **29**, 1700975 (2017).
37. Millán, M. S. & Escofet, J. Fabric inspection by near-infrared machine vision. *Opt. Lett.* **29**, 1440 (2004).
38. Jonsson, P., Casselgren, J. & Thörnberg, B. Road Surface Status Classification Using Spectral Analysis of NIR Camera Images. *IEEE Sensors Journal* **15**, 1641–1656 (2015).
39. Weissleder, R. A clearer vision for in vivo imaging. *Nature Biotechnology* **19**, 316 (2001).
40. Wu, Z., Yao, W., London, A. E., Azoulay, J. D. & Ng, T. N. Elucidating the Detectivity Limits in Shortwave Infrared Organic Photodiodes. *Advanced Functional Materials* **28**, 1800391 (2018).
41. Yao, Y. *et al.* Plastic Near-Infrared Photodetectors Utilizing Low Band Gap Polymer. *Advanced Materials* **19**, 3979–3983 (2007).

42. Zhang, H. *et al.* Transparent Organic Photodetector using a Near-Infrared Absorbing Cyanine Dye. *Scientific Reports* **5**, 9439 (2015).
43. Young, M. *et al.* Organic Heptamethine Salts for Photovoltaics and Detectors with Near-Infrared Photoresponse up to 1600 nm. *Advanced Optical Materials* **4**, 1028–1033 (2016).
44. Choi, M.-S., Chae, S., Kim, H. J. & Kim, J.-J. Control of Crystallinity in PbPc:C60 Blend Film and Application for Inverted Near-Infrared Organic Photodetector. *ACS Appl. Mater. Interfaces* **10**, 25614–25620 (2018).
45. Wu, G. *et al.* Perovskite/Organic Bulk-Heterojunction Integrated Ultrasensitive Broadband Photodetectors with High Near-Infrared External Quantum Efficiency over 70%. *Small* **14**, 1802349 (2018).
46. Wang, H. *et al.* Three-Phase Morphology Evolution in Sequentially Solution-Processed Polymer Photodetector: Toward Low Dark Current and High Photodetectivity. *ACS Appl. Mater. Interfaces* **10**, 3856–3864 (2018).
47. Armin, A. *et al.* Thick junction broadband organic photodiodes. *Laser & Photonics Reviews* **8**, 924–932 (2014).
48. Proctor, C. M. & Nguyen, T.-Q. Effect of leakage current and shunt resistance on the light intensity dependence of organic solar cells. *Appl. Phys. Lett.* **106**, 083301 (2015).
49. Sze, S. M. & Ng, K. K. *Physics of Semiconductor Devices*. (John Wiley & Sons, 2006).
50. Brus, V. V. *et al.* Graphene/semi-insulating single crystal CdTe Schottky-type heterojunction X- and γ-Ray Radiation Detectors. *Scientific Reports* **9**, 1065 (2019).
51. Wu, Z., Zhai, Y., Kim, H., Azoulay, J. D. & Ng, T. N. Emerging Design and Characterization Guidelines for Polymer-Based Infrared Photodetectors. *Acc. Chem. Res.* **51**, 3144–3153 (2018).
52. Vollbrecht, J. *et al.* Quantifying the Nongeminate Recombination Dynamics in Nonfullerene Bulk Heterojunction Organic Solar Cells. *Advanced Energy Materials* **9**, 1901438 (2019).
53. Biele, M. *et al.* Spray-Coated Organic Photodetectors and Image Sensors with Silicon-Like Performance. *Advanced Materials Technologies* **4**, 1800158 (2019).
54. Karki, A. *et al.* Unifying Energetic Disorder from Charge Transport and Band Bending in Organic Semiconductors. *Advanced Functional Materials* **29**, 1901109 (2019).
55. Albrecht, S. *et al.* Quantifying Charge Extraction in Organic Solar Cells: The Case of Fluorinated PCPDTBT. *J. Phys. Chem. Lett.* **5**, 1131–1138 (2014).
56. Lochner, C. M., Khan, Y., Pierre, A. & Arias, A. C. All-organic optoelectronic sensor for pulse oximetry. *Nature Communications* **5**, 1–7 (2014).
57. Zhou, X., Yang, D. & Ma, D. Extremely Low Dark Current, High Responsivity, All-Polymer Photodetectors with Spectral Response from 300 nm to 1000 nm. *Advanced Optical Materials* **3**, 1570–1576 (2015).
58. Huang, J. *et al.* A High-Performance Solution-Processed Organic Photodetector for Near-Infrared Sensing. *Advanced Materials* **32**, 1906027 (2020).
59. Jang, W. *et al.* Superior Noise Suppression, Response Time, and Device Stability of Non-Fullerene System over Fullerene Counterpart in Organic Photodiode. *Advanced Functional Materials* **30**, 2001402 (2020).
60. Vuuren, R. D. J., Armin, A., Pandey, A. K., Burn, P. L. & Meredith, P. Organic Photodiodes: The Future of Full Color Detection and Image Sensing. *Advanced Materials* **28**, 4766–4802 (2016).

61. Qi, Z., Cao, J., Li, H., Ding, L. & Wang, J. High-Performance Thermally Stable Organic Phototransistors Based on PSeTPTI/PC61BM for Visible and Ultraviolet Photodetection. *Advanced Functional Materials* **25**, 3138–3146 (2015).
62. Pierre, A., Deckman, I., Lechêne, P. B. & Arias, A. C. High Detectivity All-Printed Organic Photodiodes. *Advanced Materials* **27**, 6411–6417 (2015).
63. Zhou, X. *et al.* Ultrahigh Gain Polymer Photodetectors with Spectral Response from UV to Near-Infrared Using ZnO Nanoparticles as Anode Interfacial Layer. *Advanced Functional Materials* **26**, 6619–6626 (2016).
64. Liao, Z.-M., Liu, K.-J., Zhang, J.-M., Xu, J. & Yu, D.-P. Effect of surface states on electron transport in individual ZnO nanowires. *Physics Letters A* **367**, 207–210 (2007).
65. Pachoumi, O., Li, C., Vaynzof, Y., Banger, K. K. & Sirringhaus, H. Improved Performance and Stability of Inverted Organic Solar Cells with Sol–Gel Processed, Amorphous Mixed Metal Oxide Electron Extraction Layers Comprising Alkaline Earth Metals. *Advanced Energy Materials* **3**, 1428–1436 (2013).
66. Verbakel, F., Meskers, S. C. J. & Janssen, R. A. J. Electronic memory effects in diodes from a zinc oxide nanoparticle-polystyrene hybrid material. *Appl. Phys. Lett.* **89**, 102103 (2006).
67. Wang, K., Liu, C., Meng, T., Yi, C. & Gong, X. Inverted organic photovoltaic cells. *Chem. Soc. Rev.* **45**, 2937–2975 (2016).
68. Brus, V. V. *et al.* Balance Between Light Absorption and Recombination Losses in Solution-Processed Small Molecule Solar Cells with Normal or Inverted Structures. *Advanced Energy Materials* **8**, 1801807 (2018).
69. Liu, G., Li, T., Zhan, X., Wu, H. & Cao, Y. High-Sensitivity Visible–Near Infrared Organic Photodetectors Based on Non-Fullerene Acceptors. *ACS Appl. Mater. Interfaces* **12**, 17769–17775 (2020).
70. Trost, S. *et al.* Overcoming the "Light-Soaking" Issue in Inverted Organic Solar Cells by the Use of Al:ZnO Electron Extraction Layers. *Advanced Energy Materials* **3**, 1437–1444 (2013).
71. Wang, Y. *et al.* High sensitivity and fast response solution processed polymer photodetectors with polyethylenimine ethoxylated (PEIE) modified ITO electrode. *Opt. Express, OE* **25**, 7719–7729 (2017).
72. Trost, S. *et al.* Avoiding Photoinduced Shunts in Organic Solar Cells by the Use of Tin Oxide (SnOx) as Electron Extraction Material Instead of ZnO. *Advanced Energy Materials* **6**, 1600347 (2016).
73. Huang, S. *et al.* Solution-processed SnO2 nanoparticle interfacial layers for efficient electron transport in ZnO-based polymer solar cells. *Organic Electronics* **62**, 373–381 (2018).
74. Huang, S. *et al.* Low-Temperature Solution-Processed Mg:SnO2 Nanoparticles as an Effective Cathode Interfacial Layer for Inverted Polymer Solar Cell. *ACS Sustainable Chem. Eng.* **6**, 6702–6710 (2018).
75. Xiong, L. *et al.* Performance enhancement of high temperature SnO 2 -based planar perovskite solar cells: electrical characterization and understanding of the mechanism. *Journal of Materials Chemistry A* **4**, 8374–8383 (2016).
76. Akgul, F. A. *et al.* Structural and electronic properties of SnO2. *Journal of Alloys and Compounds* **579**, 50–56 (2013).

77. Tran, V.-H., Khan, R., Lee, I.-H. & Lee, S.-H. Low-temperature solution-processed ionic liquid modified SnO2 as an excellent electron transport layer for inverted organic solar cells. *Solar Energy Materials and Solar Cells* **179**, 260–269 (2018).
78. Grätzel, M. Photoelectrochemical cells. *Nature* **414**, 338–344 (2001).
79. Xiong, L. *et al.* Review on the Application of SnO2 in Perovskite Solar Cells. *Advanced Functional Materials* **28**, 1802757 (2018).
80. Tran, V.-H., Ambade, R. B., Ambade, S. B., Lee, S.-H. & Lee, I.-H. Low-Temperature Solution-Processed SnO2 Nanoparticles as a Cathode Buffer Layer for Inverted Organic Solar Cells. *ACS Appl. Mater. Interfaces* **9**, 1645–1653 (2017).
81. Jiang, Q., Zhang, X. & You, J. SnO2: A Wonderful Electron Transport Layer for Perovskite Solar Cells. *Small* **14**, 1801154 (2018).
82. Jiang, Y. *et al.* Photocatalytic effect of ZnO on the stability of nonfullerene acceptors and its mitigation by SnO_2 for nonfullerene organic solar cells. *Mater. Horiz.* **6**, 1438–1443 (2019).
83. Li, W. *et al.* Visible to Near-Infrared Photodetection Based on Ternary Organic Heterojunctions. *Advanced Functional Materials* **29**, 1808948 (2019).
84. Wang, J. *et al.* Organic Cavity Photodetectors Based on Nanometer-Thick Active Layers for Tunable Monochromatic Spectral Response. *ACS Photonics* acsphotonics.9b00471 (2019) doi:10.1021/acsphotonics.9b00471.
85. Yuan, J. *et al.* Single-Junction Organic Solar Cell with over 15% Efficiency Using Fused-Ring Acceptor with Electron-Deficient Core. *Joule* **3**, 1140–1151 (2019).
86. Reemts, J. & Kittel, A. Persistent photoconductivity in highly porous ZnO films. *Journal of Applied Physics* **101**, 013709 (2007).
87. Kröger, M. *et al.* Role of the deep-lying electronic states of MoO3 in the enhancement of hole-injection in organic thin films. *Appl. Phys. Lett.* **95**, 123301 (2009).
88. Manor, A., Katz, E. A., Tromholt, T. & Krebs, F. C. Electrical and Photo-Induced Degradation of ZnO Layers in Organic Photovoltaics. *Advanced Energy Materials* **1**, 836–843 (2011).
89. Prosa, M. *et al.* Enhanced Ultraviolet Stability of Air-Processed Polymer Solar Cells by Al Doping of the ZnO Interlayer. *ACS Appl. Mater. Interfaces* **8**, 1635–1643 (2016).
90. Clark, J. & Lanzani, G. Organic photonics for communications. *Nature Photonics* **4**, 438–446 (2010).
91. Chow, P. C. Y. & Someya, T. Organic Photodetectors for Next-Generation Wearable Electronics. *Advanced Materials* **32**, 1902045 (2020).
92. Dou, L., Liu, Y., Hong, Z., Li, G. & Yang, Y. Low-Bandgap Near-IR Conjugated Polymers/Molecules for Organic Electronics. *Chem. Rev.* **115**, 12633–12665 (2015).
93. Wu, Y.-L., Fukuda, K., Yokota, T. & Someya, T. A Highly Responsive Organic Image Sensor Based on a Two-Terminal Organic Photodetector with Photomultiplication. *Advanced Materials* **31**, 1903687 (2019).
94. Chen, H.-Y., Lo, M. K. F., Yang, G., Monbouquette, H. G. & Yang, Y. Nanoparticle-assisted high photoconductive gain in composites of polymer and fullerene. *Nature Nanotechnology* **3**, 543–547 (2008).
95. Miao, J., Zhang, F., Du, M., Wang, W. & Fang, Y. Photomultiplication Type Organic Photodetectors with Broadband and Narrowband Response Ability. *Advanced Optical Materials* **6**, 1800001 (2018).

96. Tang, F. *et al.* Improved photomultiplication in inverted-structure organic photodetectors via interfacial engineering. *Appl. Phys. Lett.* **113**, 043303 (2018).
97. Neethipathi, D. K. *et al.* High-Performance Photomultiplication Photodiode with a 70 nm-Thick Active Layer Assisted by IDIC as an Efficient Molecular Sensitizer. *ACS Appl. Mater. Interfaces* **11**, 21211–21217 (2019).
98. Li, L. *et al.* Achieving EQE of 16,700% in P3HT:$PC_{71}BM$ based photodetectors by trap-assisted photomultiplication. *Scientific Reports* **5**, 9181 (2015).
99. Chuang, S.-T., Chien, S.-C. & Chen, F.-C. Extended spectral response in organic photomultiple photodetectors using multiple near-infrared dopants. *Applied Physics Letters* **100**, 013309 (2012).
100. Hammond, W. T. & Xue, J. Organic heterojunction photodiodes exhibiting low voltage, imaging-speed photocurrent gain. *Appl. Phys. Lett.* **97**, 073302 (2010).
101. Dong, R. *et al.* An Ultraviolet-to-NIR Broad Spectral Nanocomposite Photodetector with Gain. *Advanced Optical Materials* **2**, 549–554 (2014).
102. Zhao, Z. *et al.* Photomultiplication Type Broad Response Organic Photodetectors with One Absorber Layer and One Multiplication Layer. *J. Phys. Chem. Lett.* **11**, 366–373 (2020).
103. Li, L., Zhang, F., Wang, W., Fang, Y. & Huang, J. Revealing the working mechanism of polymer photodetectors with ultra-high external quantum efficiency. *Physical Chemistry Chemical Physics* **17**, 30712–30720 (2015).
104. Wang, W. *et al.* Highly Narrowband Photomultiplication Type Organic Photodetectors. *Nano Letters* **17**, 1995–2002 (2017).
105. Li, L. *et al.* Trap-Assisted Photomultiplication Polymer Photodetectors Obtaining an External Quantum Efficiency of 37 500%. *ACS Appl. Mater. Interfaces* **7**, 5890–5897 (2015).
106. Baeg, K.-J., Binda, M., Natali, D., Caironi, M. & Noh, Y.-Y. Organic Light Detectors: Photodiodes and Phototransistors. *Advanced Materials* **25**, 4267–4295 (2013).
107. Miao, J. & Zhang, F. Recent Progress on Photomultiplication Type Organic Photodetectors. *Laser & Photonics Reviews* **13**, 1800204 (2019).
108. Nie, R. *et al.* Highly Sensitive and Broadband Organic Photodetectors with Fast Speed Gain and Large Linear Dynamic Range at Low Forward Bias. *Small* **13**, 1603260 (2017).
109. Kaake, L. *et al.* Effects of Impurities on Operational Mechanism of Organic Bulk Heterojunction Solar Cells. *Advanced Materials* **25**, 1706–1712 (2013).
110. Pearson, A., O'Mullane, A. P., Bhargava, S. K. & Bansal, V. Synthesis of CuTCNQ/Au Microrods by Galvanic Replacement of Semiconducting Phase I CuTCNQ with KAuBr4 in Aqueous Medium. *Inorg. Chem.* **51**, 8791–8801 (2012).
111. Koch, N., Duhm, S., Rabe, J. P., Vollmer, A. & Johnson, R. L. Optimized Hole Injection with Strong Electron Acceptors at Organic-Metal Interfaces. *Phys. Rev. Lett.* **95**, 237601 (2005).
112. Di, C. *et al.* High-Performance Low-Cost Organic Field-Effect Transistors with Chemically Modified Bottom Electrodes. *J. Am. Chem. Soc.* **128**, 16418–16419 (2006).
113. Soci, C. *et al.* ZnO Nanowire UV Photodetectors with High Internal Gain. *Nano Lett.* **7**, 1003–1009 (2007).
114. Thorpe, S., Fize, D. & Marlot, C. Speed of processing in the human visual system. *Nature* **381**, 3 (1996).
115. Scharber, M. C. & Sariciftci, N. S. Low Band Gap Conjugated Semiconducting Polymers. *Advanced Materials Technologies* **6**, 2000857 (2021).

116. Ghasemi, M. *et al.* A molecular interaction–diffusion framework for predicting organic solar cell stability. *Nat. Mater.* **20**, 525–532 (2021).